School of Civil and Mechanical Engineering
Department of Mechanical Engineering

Analysis and Optimization of High Temperature Thermochemical Energy Storage Systems for Concentrated Solar Power

Arun Mathew

0000-0001-9307-3740

This thesis is presented for the Degree of
Doctor of Philosophy
of
Curtin University

November 2021

Declaration

To the best of my knowledge and belief this thesis contains no material previously published by any other person except where due acknowledgment has been made. This thesis contains no material which has been accepted for the award of any other degree or diploma in any university.

Signature: ……

Date: 03/11/2021

Abstract

Owing to the growing concerns on global warming coupled with increased energy demand in the past few decades, worldwide research has clearly intensified in advancing the renewable energy technology in reducing the dependency on traditional fossil fuels. In particular, the use of solar energy is regarded to be a viable option for the thermal power generation industry, where high levels of greenhouse gas emissions are evident and challenge regulatory targets. However, wider application of solar energy is largely limited by its day-time intermittent characteristics and being not available as a continuous energy resource throughout the day. Thermal energy storage technology added to solar collector systems would improve the reliability, uninterrupted supply and the practical viability of solar energy, in particular for high-temperature thermal power generation with concentrated solar power (CSP) facilities. In this respect, the development of energy-efficient and cost-effective thermal storage solutions is pivotal for the advancement and wider appeal for CSP plant technology.

Among the thermal energy storage systems available, thermochemical reactors are considered the most efficient, for they absorb or release stored energy through reversible chemical processes without residual effects that lead to decline in performance. The current status of this technology is primitive and remains underdeveloped owing to the complicated processes within these reactors and the lack of scientific investigation thereof. Vital to the advancement of thermochemical energy storage methodology is the analysis, characterisation and optimisation of suitable thermochemical reactors for enhancing performance and thermal storage efficiency. Additionally, a clear understanding of heat transfer mechanisms and the enhancement potency within a thermochemical reactor are critical for optimising reactor design and performance improvements in such thermal storage system. This thesis presents a research investigation on high-temperature thermochemical energy storage reactors using magnesium hydride and calcium carbonate as packed beds, which represent the status-quo of the reactor media technology.

In the first stage of this investigation, numerical modelling is carried out on a reactor having a packed bed of ball-milled magnesium hydride (MgH_2) with an embedded helical coil carrying cooling water for heat exchange. MgH_2 is doped with additives of titanium

boride (TiB_2) and expanded natural graphite (ENG) for enhancing the thermal conductivity of the medium. The hydrogen absorption by the packed bed is determined using Sievert's apparatus. Following the established and reported research practice, the reaction kinetics of hydrogen absorption is formulated using the kinetics fitting method and incorporated into the three-dimensional numerical model. The simulation is used for examining the effect of reactor bed thermal conductivity, heat transfer fluid flow velocity and the hydrogen supply pressure on the reactor performance. These outcomes and trends are validated by experimental data that show excellent compatibility and prediction accuracy.

The results indicate that the reactor performance declines when the heat transfer fluid temperature elevates during heat collection from the reactor bed. For appraising this, a case of flow boiling is considered in the helical tubes, which would maintain constant (saturation) temperature in the heat transfer fluid. The numerical model developed is modified accordingly with a boiling heat transfer mechanism, and using the Eulerian two-fluid framework, this multi-phase flow is simulated. Flow turbulence is modelled using the *SST-k-*ω Reynolds-Averaged Navier-Stokes equations. This study allows the comparison of MgH_2 reactor performance with multi-phase flow to that having single-phase flow, thus establishing the impact from heat transfer fluid temperature variations on the reactor performance. The results indicate the MgH_2 reactor with boiling flow absorbs much higher degree of heat and accelerates the hydrogenation reaction, hence improving thermal performance.

In the second stage of this reactor investigation, a packed bed having limestone-based calcium carbonate doped with aluminium oxide (Al_2O_3) is used, for examining the suitability of such a medium with carbon dioxide absorption. The carbonation kinetics is measured using a thermogravimetric analyser (TGA) and the reaction rate expression is formulated for the simulation as in the case with magnesium hydride. The influence of applied carbon dioxide pressure, reactor bed thermal conductivity, and the boundary temperature on carbonation are investigated. These indicate that calcium carbonate reactor delivers much faster reaction kinetics and enhanced thermal storage performance. Additionally, expanded graphite fins are added to the bed geometry to examine the effects of varying thermal conductivity on the reactor performance. This modification beneficially increased the carbonation process, hence thermal performance.

Acknowledgements

It gives me great pleasure to share my research journey with everyone and convey my gratitude to those who helped me get here without their assistance.

To begin, I would like to convey my gratitude to my supervisor, Prof. Tilak T Chandratilleke, for his constant encouragement, support, and guidance through his breadth of expertise throughout my Ph.D. studies. I will always be indebted to him for the opportunity he has given me to work under his supervision.

I would like to express my sincere thanks to my co-supervisor, Dr. Nima Nadim, for his guidance and assistance throughout my research. He was a constant source of encouragement, and his advice, intellect and persona, was vital in negotiating difficult situations.

I would also like to convey my appreciation to Dr. Terry Humphries for his unique and critical advice throughout my research. He was constantly eager to assist me and point me in the right direction. Additionally, I thank Assoc Prof. Mark Paskevicius, whose ideas, knowledge, and support were crucial in completing this project. I would like to express my acknowledgement to Prof. Craig E. Buckley for guiding me and providing an opportunity to collaborate with the Hydrogen Storage Research Group at Curtin University.

The research funding for the current project was provided by The Australian Research Council (ARC) Linkage Projects (Grant ID: LP150100730) and the Curtin International Postgraduate Research Scholarship (CIPRS), which we are extremely helpful in carrying out my research work successfully.

Statement of attribution

The following publications have arisen from this work, representing Chapters 3, 4 and 5, respectively.

1. Mathew A, Nadim N, Chandratilleke TT, Humphries TD, Paskevicius M, Buckley CE. Performance analysis of a high-temperature magnesium hydride reactor tank with a helical coil heat exchanger for thermal storage. International Journal of Hydrogen Energy. 2021;46:1038-55 (Published).
2. Mathew A, Nadim N, Chandratilleke TT, Humphries TD, Buckley CE. Investigation of boiling heat transfer for improved performance of metal hydride thermal energy storage. International Journal of Hydrogen Energy. 2021;46:28200-13 (Published).
3. Mathew A, Nadim N, Chandratilleke TT, Paskevicius M, Humphries TD, Buckley CE. Kinetic investigation and numerical modelling of $CaCO_3/Al_2O_3$ reactor for high-temperature thermal energy storage application. Journal of Energy Storage (Submitted).

Due to the generally consistent authorship and contributions, individual inputs have been summarized in a single table, below.

	Concept/ Design	Reaction Modelling	Simulation/ Analysis	Interpretation/ Discussion	Final Approval
Arun Mathew (Publication 1,2,3)	✓	✓	✓	✓	✓
I acknowledge that these represented my contribution to the above research output. Signature:					
Nima Nadim (Publication 1,2,3)	✓		✓	✓	✓
I acknowledge that these represented my contribution to the above research output. Signature:					

Tilak T Chandratilleke (Publication 1,2,3)	✓	✓	✓	✓	✓
I acknowledge that these represented my contribution to the above research output. Signature:					
Terry D Humphries (Publication 1,2,3)	✓			✓	✓
I acknowledge that these represented my contribution to the above research output. Signature:					
Mark Paskevicius (Publication 1,3)	✓			✓	✓
I acknowledge that these represented my contribution to the above research output. Signature:					
Craig E Buckley (Publication 1,2,3)	✓			✓	✓
I acknowledge that these represented my contribution to the above research output. Signature:					

Table of Contents

List of Figures

List of Tables

CHAPTER 1: INTRODUCTION AND OVERVIEW

This chapter provides an overview of the major themes in this thesis. The chapter includes the background of thermal energy storage, motivations, and the objectives of the current work. Further, a brief discussion of numerical modelling, boiling heat transfer, turbulence and multiphase modelling techniques used in the study is included.

1.1 Background

Climate change is now considered as one of the most critical concerns the planet is facing. Expanding carbon footprint associated with the use of fossil fuels is considered to be the main reason for this phenomenon. As a result, transition to more environmentally friendly energy sources is essential. To address climate change concerns, governing bodies across the globe have considered enacting a reduction in carbon dioxide emission regulations. In this scenario, there will be serious incentives for utilising the potential of solar energy as a sustainable and abundant resource, capable of serving as a substitute for fossil fuels. However, while considerable work has been done on developing solar-based energy solutions, the widespread deployment has been hampered by the intermittent nature of this source. The intermittency issue can be overcome by developing an effective energy storage system that enables solar energy to be distributed when it comes to this potential solution.

Among the available energy storage technologies, thermochemical energy storage technology has demonstrated superior traits, such as higher energy density, energy storage for a more extended period, and lower cost. Additionally, the higher operating temperature associated with this technology improves the efficiency of the accompanying energy conversion devices. In this method, heat energy is stored by utilising a chemical compound that undergoes reversible endothermic reactions. Consequently, the heat energy is stored in the chemical bond of the operating material.

While considering the suitable energy storage material for the thermochemical energy storage method, magnesium hydride (MgH_2) and calcium carbonate ($CaCO_3$) are attractive options due to their high energy storage capacity, suitable thermophysical properties, abundancy, low cost, and lack of toxicity. Apart from that, both materials have been investigated previously: MgH_2 as a viable hydrogen storage material for mobile applications and $CaCO_3$ as a carbon dioxide capture material in fossil-fuel power

plants. However, due to material synthesis and complexity in reactor development, thermochemical energy storage technology is currently available only on laboratory scale. Additionally, because thermochemical energy storage technology involves a great deal of heat exchange, optimising the system's thermal performance has been crucial to the overall development of thermochemical energy storage technology.

1.2 Objective

The broad objective of this study is to optimise the performance of high-temperature thermochemical energy storage reactors based on magnesium hydride and calcium carbonate. This is performed through the simulation and analysis of various reactor designs using a computational fluid dynamics (CFD) approach.

The below-mentioned procedures were adopted to meet the study objectives:

- Estimate the hydrogenation kinetics of magnesium hydride and carbonation kinetics of calcium carbonate reactions.
- Using ANSYS Fluent to develop a numerical solver for thermo-fluid analysis.
- Generation and meshing of various reactor geometries based on the analysis constraints.
- Develop user-defined functions to incorporate the reaction energy source terms into the model.
- Conduct various parametric investigations of the magnesium hydride and calcium carbonate reactors.
- Model multiphase flow in a magnesium hydride reactor.

1.3 Motivation

This thesis is funded by the Australian Research Council (ARC) for the research towards improving the use of thermochemical energy storage in concentrating solar power plants (CSP). According to the literature review, there is much potential for performance optimisation of thermochemical reactors in the future generation of thermochemical energy storage systems, coupled with CSP. The performance improvement can be achieved mainly by optimising heat extraction from the reactor bed and conducting research on potential novel energy storage materials, both of which are addressed in this work.

1.4 Thesis outline

This thesis is framed as a consolidation of published/submitted articles in a hybrid format. Specifically, Chapters 3, 4, and 5 are from the published/submitted journal articles.

- Chapter 2 of this thesis provides basic information on solar energy, thermal energy storage systems, thermochemical energy storage, and the kinetics of gas-solid processes. Additionally, this section discusses various experimental and numerical research conducted on the magnesium hydride and calcium carbonate materials for thermal energy storage applications.
- Chapter 3 describes the study of the hydrogenation reaction kinetics of magnesium hydride. The reaction rate and energy source terms of the hydrogenation reaction are formulated using the derived kinetics models and parameters. Then, using the synthesised kinetic models, numerical validation and parametric analysis are done on a magnesium hydride reactor equipped with a helical coil heat exchanger.
- In Chapter 4, the effect of heat absorption on the performance of a magnesium hydride reactor in single-to-multiphase phase is investigated. The transient boiling heat transfer is modelled using a Eulerian two-fluid scheme.
- Chapter 5 contains a detailed examination of the carbonation kinetics of the calcium carbonate compound. Then, a numerical investigation of the calcium carbonate reactor's performance was conducted by utilising the acquired kinetics models and parameters. Accordingly, the parametric analysis of key parameters in the reactor was conducted.
- Chapter 6 includes the conclusion of the thesis. It includes the summary of the works carried out, from which inference was made that multiphase heat transfer is an effective method of heat absorption and that calcium carbonate compounds have considerable potential as high-temperature thermal energy storage media.

1.5 Numerical Modelling

Computational Fluid Dynamics (CFD) is a computer-assisted engineering technique for evaluating various processes, such as fluid flow, heat transfer, and related phenomena like a chemical reaction. CFD simulation consists of two stages: firstly, a numerical model is developed using a sequence of mathematical equations representing the flow; secondly, these equations are solved using computer software to acquire the flow

variables inside the domain of interest. Since the introduction and evolution of the digital computer, CFD has garnered great attention and has been widely employed in the engineering sector to investigate many aspects of fluid dynamics.

Partial differential equations (PDEs), such as Navier–Stokes equations, are commonly used to represent the governing equations in a flow field. These equations, however, cannot be solved analytically, hence the numerical solution becomes the preferred option. As a result, PDEs must be converted to discrete set of equations, enabling linearisation. The main discretisation techniques are finite difference, finite element, and finite volume methods.

ANSYS-FLUENT software package, working on the basis of Finite-Volume discretisation scheme, is utilised in this study. The finite volume approach is one of the most widely used numerical discretisation methods in thermo-fluid applications. This method is based on the discretisation of the spatial domain into finite control volumes. Usually, a control volume consists of a large number of mesh components, each of which can be divided into sectors corresponding to a specific mesh element. As a result of this integration, it is possible to ensure the exact conservation of given scalar in discrete finite volumes. Each integral term is discretised, generating a series of linear algebraic equations at the control volume's nodal or centroid locations. Following that, the linear equations are solved using an algebraic multigrid solver. The non-compressible Navier-Stokes equations are solved using a staggered grid.

1.5.1 Flow Modelling

By solving basic conservation equations for the mass and momentum of the fluid, a single-phase fluid flow can be simulated using classical fluid dynamics knowledge. In addition to the basic equations, an energy conservation equation must be solved if the flow involves heat transfer.

To solve problems related to the single-phase fluid flow, the following equations are used. Continuity equation:

$$\frac{\partial \rho}{\partial t} + \nabla . (\rho \vec{v}) = 0 \tag{1.1}$$

where density, velocity and time are denoted by ρ, v and t, respectively.

According to the conservation of mass equation, the mass flux, through the boundary surfaces, equals the rate of mass transfer in a small control volume.

Momentum equation:

$$\frac{\partial(\rho\vec{v})}{\partial t} + \nabla.(\rho\vec{v}\vec{v}) = -\nabla P + \nabla.\tau + \rho\vec{g} \quad (1.2)$$

where P, τ, g represents pressure, stress tensor (potentially embedded with turbulence stresses) and gravitational acceleration, respectively. According to the momentum equation, the rate at which momentum enters or leaves a surface is equal to the sum of the rate of change in momentum in the control volume and the amount of the forces acting on the control volume.

Energy equation is similarly represented by another transport equation which balances transient, diffusion, advection and source terms as:

$$\frac{\partial(\rho C_P T)}{\partial t} + \nabla.(\rho C_P\vec{v}T) = \lambda\nabla^2 T + \dot{Q} \quad (1.3)$$

where T, λ, $\dot{Q}$ are the temperature, thermal conductivity, and energy source term, respectively. The energy equation states that the rate of change in internal energy in the control volume is equal to the amount of the viscous stress and work done on it, as well as the rate at which enthalpy enters.

1.6 Boiling heat transfer

The phase change of fluid from liquid to vapour phase, at its saturation temperature and pressure, by applying the heat energy is defined as boiling. The application of boiling heat transfer can be seen in many applications, from cooking to large scale power generation systems, electronic cooling, heat exchangers, refrigeration systems, nuclear reactors, chemical processes. The advantage in utilising boiling as a multiphase thermal process is because it enhances heat exchange rate within a smaller temperature difference due to the release of latent heat. Compared to single-phase heat transfer, the boiling heat transfer process has two distinct advantages. Firstly, boiling heat transfer requires a smaller temperature gradient than single-phase heat transfer for a given heat flux. Secondly, higher amount of heat transfer was observed in the boiling heat transfer system compared to the single-phase system, for a given temperature gradient. These distinguishing characteristics reduce the operating temperature and size of the heat transfer system that uses boiling heat transfer.

Although boiling is complicated, Nukiyama et al. [1] showed that a single curve could accurately explain the boiling mechanism despite its complicacy. The "boiling curve" depicted in Figure 1.1 depicts the heat flux in relation to the superheat temperature of the heated wall.

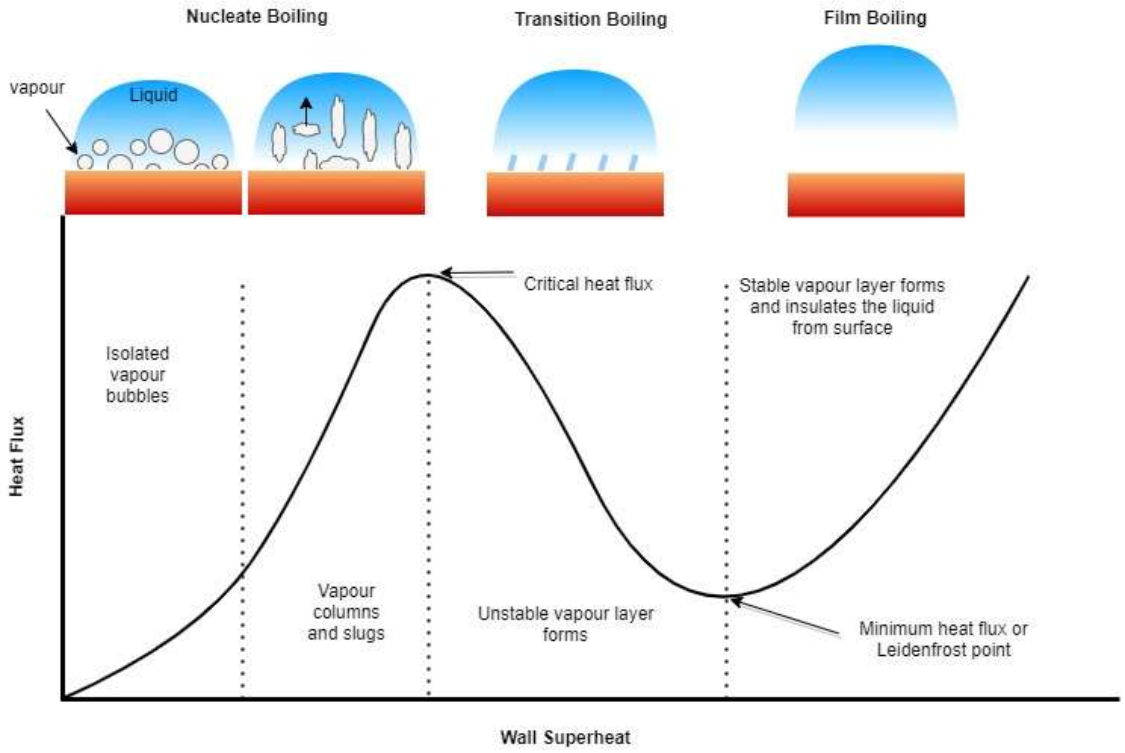

Figure 1.1: Standard boiling curve for a liquid-solid interface [1]

Boiling heat transfer through a liquid-solid interface is highly dependent on the superheat (or sub-cooled) temperature of the wall. The superheat/sub-cooled temperature is the difference between the temperature of the heated wall and the saturation temperature. Once the temperature of the heated wall exceeds the saturation temperature of the liquid, nucleation sites become active, and vapour bubbles start to form. These bubbles initially exist in isolation, but as the surface temperature and heat flux increase, additional nucleation sites form, coalescing the formed vapour into vapour columns and slugs. These vapour columns and slugs facilitate the rigorous mixing of liquid and vapour phases, increasing convection and the heat transfer coefficient. As the surface temperature exceeds the critical heat flux, the vapour pockets coalesce and begin to insulate the surface. Accordingly, maximum heat flux is achieved, referred to as the critical heat flux. At CHF, a thin vapour film forms on the heated wall, rapidly raising

the temperature and damaging the heated surface. This phenomenon is referred to as film dry out or Departure from Nucleate Boiling (DNB).

The process of boiling heat transfer phenomenon typically involves various concurrent physical processes such as bubble formation, bubble departure from the heated wall, bubble coalesce to the bulk fluid. As a result of these physical processes, complex regime of mass, momentum, and energy exchange form in the flow field. The boiling heat transfer process is governed by various parameters such as the velocity of the flow, pressure forces, thermophysical properties of the fluid, surface roughness of the heated wall, liquid-surface contact angle.

Due to the complicated nature of the boiling process and its dependence on several parameters, the estimation of complete boiling phenomena has always been a complex task. However, understanding the heat transfer mechanisms in various two-phase flow regimes is critical for defining safety margins under normal and abnormal operating conditions. Therefore, many experimental investigations have been carried out to study the boiling process, but only recently, more numerical studies were also performed due to the advancement in computational power.

1.7 Multiphase flow modelling methods

The turbulent multiphase flow has significantly complex physics, and hence numerical modelling is more challenging than the single-phase flow. Apart from the typical challenges associated with resolving/modelling a turbulent, single-phase flow field, the interfacial interactions complicate the mathematical formulation of the flow problem in multiphase flow. Currently, there is no fully mechanistic numerical scheme for resolving all types of phase exchange phenomena in engineering applications.

There are several numerical approaches available for the modelling of multiphase flow. The numerical approaches are generally classified into two categories of Euler-Lagrange and the Euler-Euler modelling approaches. A brief discussion of these two multiphase modelling approaches is described in the following section. A more detailed discussion on the various multiphase approaches and formulation of the numerical frames can be found in the literature [2].

1.7.1 Euler-Lagrange Model Approach

In Euler-Lagrange method, the continuous phase present in the multiphase flow regime is modelled by solving time-averaged Navier-Stokes equations, while the dispersed phase is approximated by tracking a large number of bubbles or droplets through the estimated continuous flow field. The critical assumption in this methodology is that the dispersed phase occupies a limited volume percentage, meaning that the dispersed phase elements are not too close together and should be regarded as distinct.

1.7.2 Euler-Euler Approach

In contrast to the Euler-Lagrange model, the Euler-Euler (also known as Eulerian two-fluid) scheme treats the phases present in the flow field as interpenetrating continua. As a result, the phases share the same volume and interact spatially, exchanging mass, momentum, and energy. The continuity, momentum, energy conservation equations for each phase are solved separately. The critical premise of this method is that the phases will mix or separate, with the dispersed phase occupying a significant volume percentage of the total volume. Because of the large volume fraction, the dispersed phase elements are too close together to be considered distinct. As a result, the interaction between the multiphase flow and the secondary phase effect will be large enough to be considered.

The interfacial forces and heat and mass fluxes are estimated by analytical or empirical correlations to formulate a particular two-fluid model. The analytical and empirical models used to estimate the interfacial interactions of each phase in the boiling heat transfer in the present study are discussed in Chapter 4.

1.8 Turbulence model

Flow is defined as laminar when fluid flows in parallel layers without interruption. Conversely, turbulent flow is determined by the chaotic properties or random fluctuations within the flow domain. This is also characterised by instantaneous variations in the pressure and velocity of a fluid (measurable quantities). Turbulent flows, in particular, merit special attention due to their extensive dependency on engineering applications. Understanding the complex phenomena of turbulence flow (physically and mathematically), on the other hand, is extremely difficult due to its highly chaotic and irregular nature.

There are three main types of turbulence models commonly used in CFD modelling: Reynolds Averaged Navier Stokes (RANS), Large Eddy Simulation (LES) and Direct Numerical Simulations (DNS). The RANS models are common and efficient among the three. ANSYS Fluent offers options of RANS family models with several sub-models such as the zero-equation, one-equation, two-equation and Reynolds stress models. Out of these options, the well-established and efficient two-equation models of k-ε and k-ω models are deployed in the CFD simulations of this thesis. These models have been formulated with the assumption of a mean and fluctuating component for flow variables based on a particular time and length scale proportional to the scale of larger eddies. After calculating the length scale, the turbulence model assumes that all fluctuations occur at scales smaller than the numerical grid size and handles them.

Two-equation models use two transport equations for the mean (time-averaged) and fluctuating turbulent component to resolve the flow velocity. The instantaneous velocity component in the x-axis in the two-equation models is written as

$$u(x,t) = U(x) + u'(x,t) \tag{1.4}$$

where u, U and u' are the instantaneous, time average, fluctuating velocity components, respectively. Similarly, the pressure component is also decomposed into two: mean and fluctuating components.

$$p(x,t) = P(x) + p'(x,t) \tag{1.5}$$

This chapter primarily covers the background of thermal energy storage as well as the numerical modelling techniques used in computational fluid dynamics simulations to analyse and assess fluid flow and heat transfer mechanisms. The performance analysis of several high-temperature thermochemical energy storage reactors, under various operating situations is addressed in the following chapters using the CFD modelling approach.

CHAPTER 2: LITERATURE REVIEW

2.1 Introduction

Global energy demand has been increasing steadily over time, most notably since the late 20th century. Current energy production mainly relies on fossil fuels, which are becoming scarce as well as detrimental to the environment. According to the International Energy Agency's (IEA) World Energy Outlook for 2018, fossil fuels such as coal, oil, and natural gas accounted for more than 80% of global energy demand in 2018. The combustion of fossil fuels generates significant amounts of greenhouse gas emissions (GHG), contributing to climate change and rising global temperatures. Carbon dioxide is a key contributor to climate change, accounting for 60% of GHG emitted due to fossil fuel combustion. The rise in carbon dioxide (CO_2) concentrations in the Earth's atmosphere over the years is depicted in Figure 2.1. Since the industrial revolution, the atmospheric CO_2 content has been steadily increasing. The CO_2 levels began to climb rapidly following 1960s, and the rate of growth has accelerated each year thereafter. The IEA estimates that if the current CO_2 growth trend continues, annual atmospheric CO_2 emissions will double by 2050.

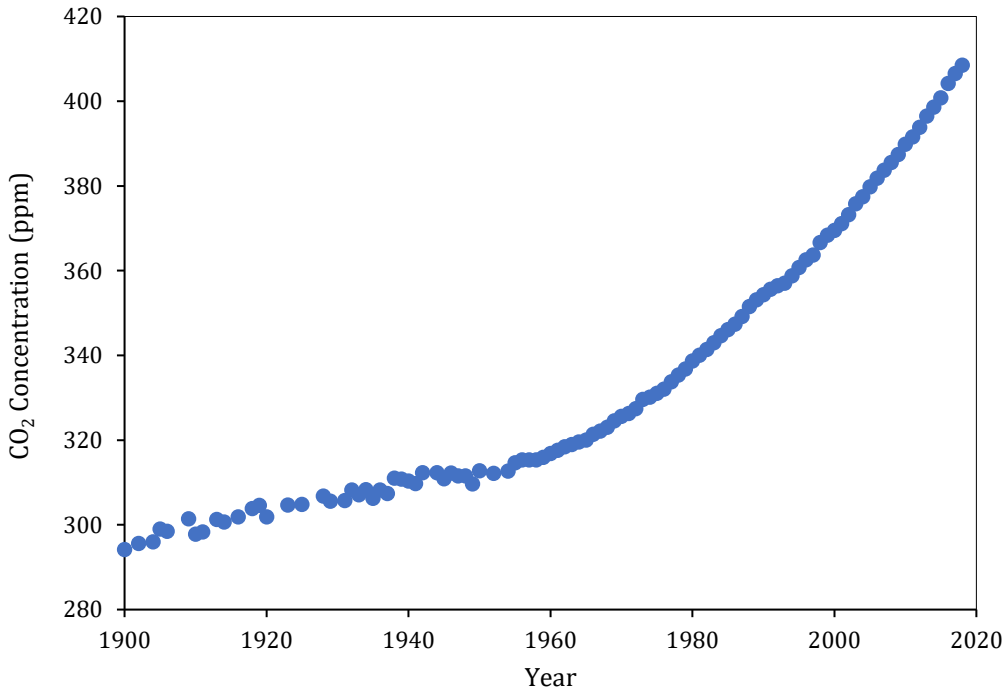

Figure 2.1: Global averaged atmospheric concentration of CO_2 [3]

Additionally, the world's rapidly depleting fossil fuel reserves are being stretched by population expansion and technological advancements. Figure 2.2 shows the global energy consumption pattern over the past few decades. Global energy consumption has risen significantly, with current energy demand being five times that of the 1960s. According to IEA, the global energy demand is estimated to reach over 900 quadrillion BTUs by 2050. As a result, there is a greater demand for abundant and environmentally friendly energy resources. Renewable energy sources such as solar, wind, and geothermal will likely be highlighted in such a situation. In 2019, all available renewable energy sources were able to meet only 11% of total energy demand. A complete transition in global energy supply from fossil fuels to renewable energy sources remains a challenge due to the heavy reliance on fossil fuels. As a result, it is fair to assume that a single renewable energy source will not be sufficient to phase out fossil fuel dependence completely; instead, each renewable energy source will need to contribute.

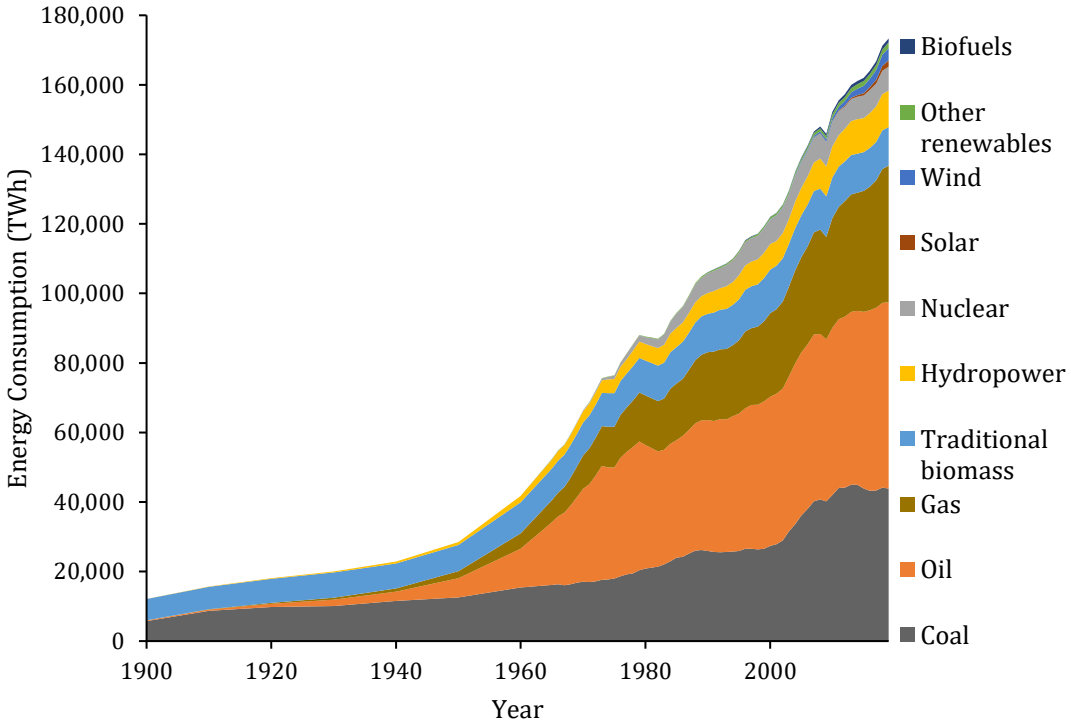

Figure 2.2: Global energy demand since 1800, classified according to energy type [4]

Solar energy is an appealing option when analysing viable green energy sources due to its abundant and pervasive energy supply. Converting around 1% of total solar irradiation on the Earth's surface, at a conversion efficiency of 10%, is estimated to be sufficient to supply the current world energy demand [5]. There are two major technologies for converting solar energy into useable forms currently available: photovoltaic (PV) and concentrated solar power (CSP). According to the IEA's roadmap, renewable energy will account for 27% of global electricity supply by 2050, with PV accounting for 60% and CSP accounting for 40%.

PV technology converts solar energy directly into usable electricity via solar panels. As sunlight strikes the solar panels, the photons in the sunlight excite the electrons in the semiconductors, creating an electron wave that generates electricity. PV technology offers various advantages, including low downtime, ease of installation, a wide range of power generation options, the absence of moving parts, and quiet operation. In addition, the cost of photovoltaic panels has been steadily decreasing, and many more affordable and powerful panels have emerged in recent years. The solar panel conversion efficiency was around 6% in the early phases, but it is now close to 44 %.

CSP technology is based on the principle of using a mirror/reflector to concentrate low-density solar radiation into a small area, resulting in high temperature. The high temperature of the working fluid produces steam or hot air, which is subsequently used to generate electricity using conventional energy conversion devices. The sunlight is concentrated using a large number of precisely controlled mirrors. The direction of the mirror changes over time, depending on the amount of available sunlight. In general, the efficiency of CSP is dictated by the temperature of its operating fluids. As a result, many mirrors are used to concentrate solar radiation into a small area, resulting in an increase in temperature.

The key attribute of an ideal energy storage technology is its ability to operate anytime and anywhere. While solar energy has enormous potential to become a major participant in the global green energy market, its intermittent nature has always prevented it from replacing fossil fuel-based energy resources. The unavailability of solar energy at night and in overcast conditions is one of the drawbacks of this resource. Figure 2.3 shows the average domestic energy usage and solar PV output trend over a day in a typical Melbourne household in 2015. The energy requirement is lowest during the daytime

where energy production is at its peak. But, the energy production from solar energy is unavailable during the high consumption period in households.

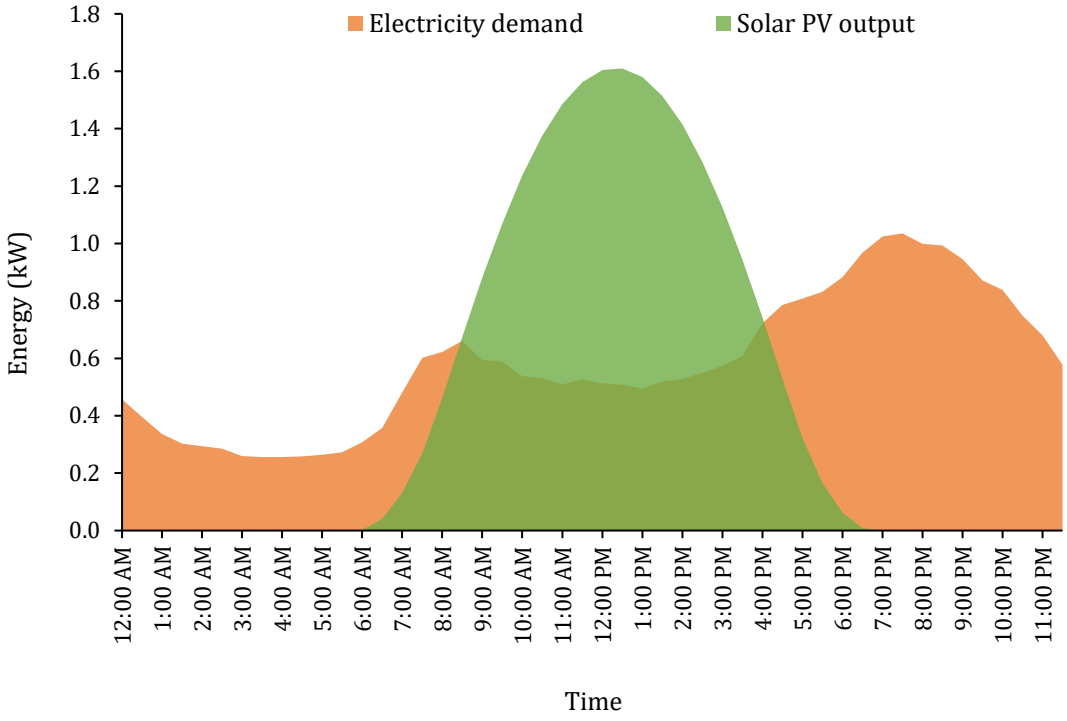

Figure 2.3: The energy consumption and generation patterns of a typical Melbourne household in 2015 [6]

Solar energy's intermittent nature can be mitigated by storing energy during peak hours for usage during off-peak hours. In terms of energy storage, CSP technology is superior to PV technology. One of the key advantages of CSP over PV is its ease of integration with an energy storage facility. Additionally, CSP technology is less expensive than PV technology when it comes to energy storage for off-peak hours. This is due to the fact that energy storage in CSP technology is in the form of heat, but energy storage in PV technology is in the form of electrical energy, which is more expensive than heat storage.

2.2 Thermal energy storage (TES)

The operation of the TES system connected with the CSP plant is depicted in Figure. 2.4. The operation begins with concentrating solar rays into a central receiver system using concentrating mirrors or heliostats. A large number of precisely controlled heliostats are placed on the ground to focus the solar rays. The heliostat's orientation varies according to the angle of solar irradiation. By concentrating a massive number of solar rays into a

small receiver area atop the central tower, the temperature of the central receiver is significantly raised. The receiver's high heat energy is collected and used to generate electricity by utilising the heat transfer fluid. TES system stores a portion of the heat energy gathered from the central receiver during the day, while the remainder is directly transmitted to the boiler. By utilising the heat energy from the HTF, the boiler produces a stream that is then used to power the turbine-generator system. The generated electricity is subsequently distributed via powerlines. The HTF transfers heat to the boiler and continuously circulates it through the central receiver. During the night, the TES system's stored heat energy is used to generate power continually.

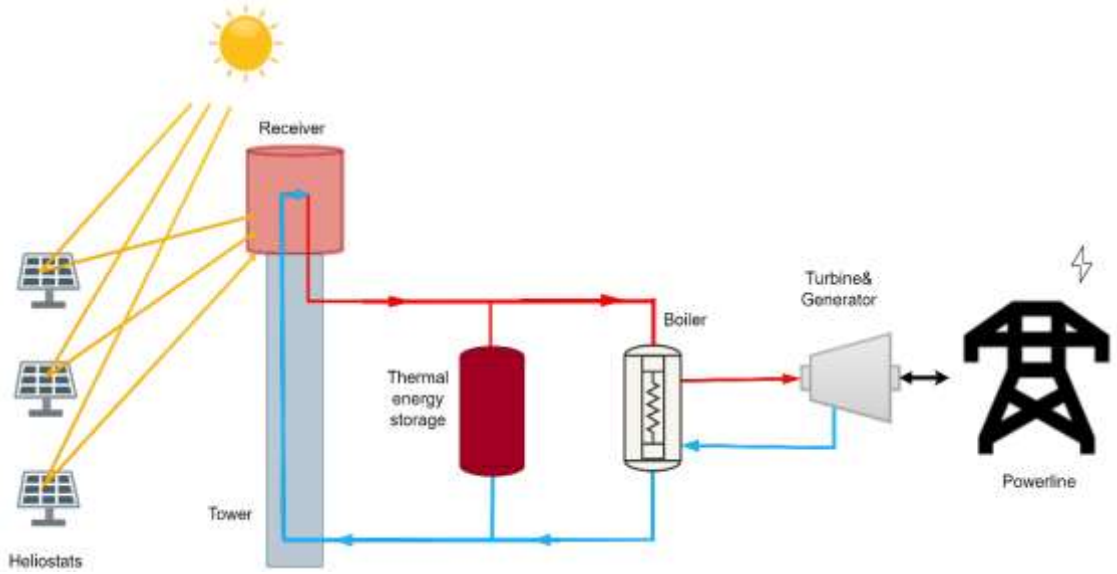

Figure 2.4: Schematic diagram showing the operation of the thermal energy storage system incorporated into the concentrating solar power plant [7]

The TES systems can be classified into three types based on the technique used to store thermal energy: sensible heat storage, latent heat storage, and thermochemical energy storage.

2.2.1 Sensible heat storage

Among the three thermal energy storage methods, sensible heat storage is the simplest and most advanced. The principle energy storage in this system is by raising the temperature of the storage medium without causing phase change. The mass and thermal capacity of the storage medium determines the storage capacity of the method.

$$Q = mc_P dT \tag{2.1}$$

where m is the mass of the material, c_P is the specific heat capacity of the material, and dT is the temperature change.

Sensible heat storage materials include various liquids (water, molten salts, mineral oil, synthetic oil) and solids (rock, high-temperature concrete, stable ceramics). Due to their superior qualities, molten salts are the most suitable material for most CSP facilities.

Compared to other thermal energy storage methods, the sensible heat storage system has the lowest energy density. The drawbacks of the method also include the need for large storage tanks, expensive heat exchangers and insulation, the corrosive nature of molten salts, and the inability to store or produce energy at a constant temperature. Furthermore, in this system, the likelihood of solidification of the energy storage material is high, necessitating constant heat exchange system monitoring.

2.2.2 Latent heat storage

In latent heat storage, the heat energy from the CSP plant is transferred to a storage medium called phase change material (PCM). PCM undergoes a phase transition from solid to liquid or liquid to gas (depending on the scenario). The phase transition involves significant amount of latent heat of fusion or vaporisation. This approach has a higher energy density than sensible heat storage; however, it is still in its early stages of development. Additionally, unlike the sensible heat storage system, the latent heat storage system maintains a constant operating temperature, which increases the system's overall efficiency.

The amount of heat energy stored by the PCM is calculated as

$$Q = mL \tag{2.2}$$

where m is the mass of the PCM, and L is the latent heat of phase change.

Both organic and inorganic materials are examined as appropriate PCM for thermal energy storage applications. Organic PCMs such as paraffin and fatty acids and inorganic PCMs such as salt hydrates and ice are commonly considered for the applications of latent heat storage. The primary PCM selection criteria include high latent heat, high thermal conductivity, non-corrosive, optimal phase change temperature, absence of side reactions, nontoxicity, and cost-effectiveness. While latent heat storage exhibits superior

properties to sensible heat storage, the method's development is hampered by the high-volume change of PCM associated with the phase change, the non-uniform thermophysical properties, and the PCM's low thermal conductivity. Additionally, corrosion of storage tanks and a high investment cost prevent this technique from being widely used.

2.2.3 Thermochemical energy storage

Thermochemical energy storage is the most energy-dense and complex storage technology of the three aforementioned options. In this method, thermal energy is stored in the molecule of the storage material via chemical bonds. A reversible exothermic and endothermic chemical reaction is used to store and release energy. Heat energy from the CSP plant is stored in the chemical compound during the day via an endothermic chemical reaction. The chemical compound undergoes an exothermic reaction during the night/off-peak hours, releasing the previously stored heat energy. The general equation of this process is expressed as

$$A \leftrightarrow B + C \tag{2.3}$$

The reactant A is decomposed into products B and C during the heat absorption cycle. In the reverse cycle, the reactants B and C are recombined, releasing previously-stored heat energy.

The total amount of heat energy stored in a thermochemical reaction is defined as:

$$Q = mc_P\Delta T + mL + m\Delta H \tag{2.4}$$

where m denotes the mass of the material, c_P denotes the specific heat capacity, L denotes latent heat per unit mass, and H denotes the heat of reaction.

While this technique is not fully developed technologically and struggling with many technical obstacles, it is found to have superior characteristics to others. Table 2.1 and 2.2 compares various aspects of the three thermal energy storage methods. When the three TES technologies are compared, the thermochemical energy storage excels them all due to two key advantages: its higher energy density and its ability to store heat energy in chemical bonds indefinitely without losing energy. Thus, it is highly advantageous for the storage and transportation of heat energy to other locations. Additionally, when compared to the other two methods, thermochemical energy storage is more easily

integrated into the CSP. However, owing to the complexities and practical limitations, the thermochemical system has been tested only in prototype scale reactors and limited discharging cycles while the large-scale implementation of other thermal storage systems is already in place.

Table 2.1: Physical parameters of various thermal energy storage materials [8]

Heat Storage Method	Materials	Specific Heat (kJ/kg/K)	Energy Density (GJ/m^3)	Working Temperature (K)
Sensible heat storage	Rock	1.30	n.a.	473−573
	Concrete	0.85	n.a.	473−673
	Mineral oil	2.60	n.a.	473−573
	Carbonate salts	1.80	n.a	723−1123
Latent heat storage	E117	2.61	0.25	390
	A164	n.a.	0.46	437
	KNO_3/KCl	1.21	n.a.	593
	$AlSi_{12}$	1.04	1.51	849
	Na_2CO_3	n.a.	0.70	1127
Thermo-chemical energy storage	Iron carbonate	n.a.	2.60	453
	Magnesium oxide	n.a.	3.30	523−673
	Hydroxides	n.a.	3.00	773
	Metal hydrides	n.a.	4.00	473−773
	Calcium carbonate	n.a	4.40	1073−1173

n.a: Not available

It is critical for the development of thermochemical energy storage to determine the suitable operating material and chemical reaction. In general, an ideal thermochemical energy storage material should meet the following criteria: high energy density, rapid and reversible reactions within a specified temperature range, mechanical stability,

appropriate heat and mass transfer properties, no degradation in thermal stability, low cost, and nontoxicity. Chemical reactions and materials of various types have been considered for TES purposes. Figure 2.5 summarises the various types of thermochemical energy storage materials and their classifications.

Table 2.2: Technical characteristics of thermal energy storage technologies [9]

Heat Storage Method	Sensible heat storage	Latent heat storage	Thermochemical energy storage
Efficiency (%)	50–90	75–90	75–100
Initial capital cost (kW)	3400–4500	6000–15000	1000–3000
Energy cost (USD/kWh)	0.1–13	10–56	8–100
Energy storage density (kWh/m^3)	25	100	~500
Durability (years)	10–30+	10–30+	10–30+
Storage capacity (MW)	0.1–300	0.1–300	0.1–300

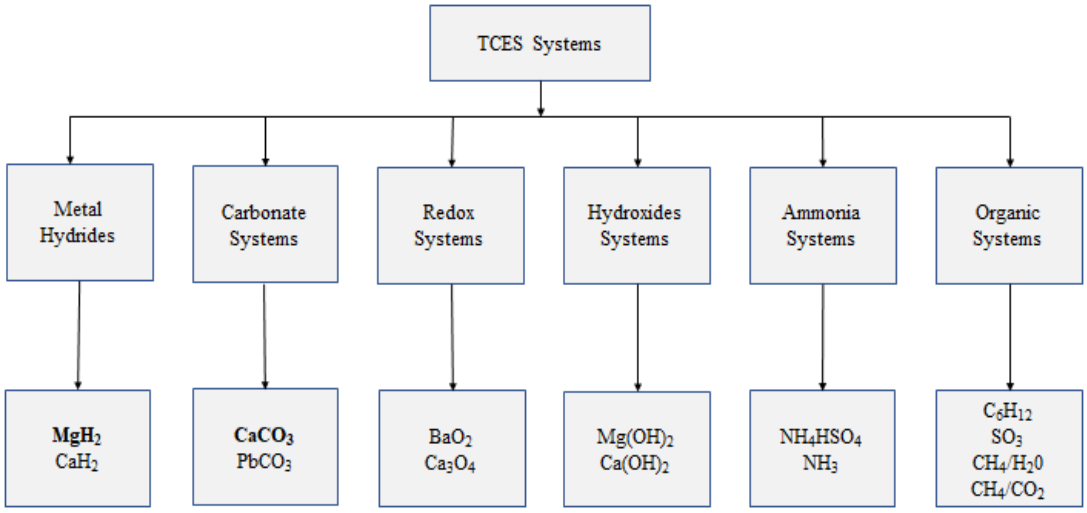

Figure 2.5: Classification of some of the thermochemical energy storage material [10]

The operating temperature of thermochemical energy storage material merits particular consideration among the many critical characteristics since it is so crucial in the overall efficiency of the energy storage system. A higher operating temperature is always

desired in the thermal energy storage application since a higher operating temperature increases the Carnot efficiency of the energy conversion devices used in CSP plants. The operating temperature of different thermochemical energy storage materials, as well as the volumetric energy storage density associated with that temperature, are shown in Figure. 2.6. Among the available thermochemical energy storage materials, metal hydride-based magnesium hydride (MgH_2) and metal carbonate-based calcium carbonate ($CaCO_3$) materials are considered in this thesis. These materials have high volumetric energy density and high operating temperatures.

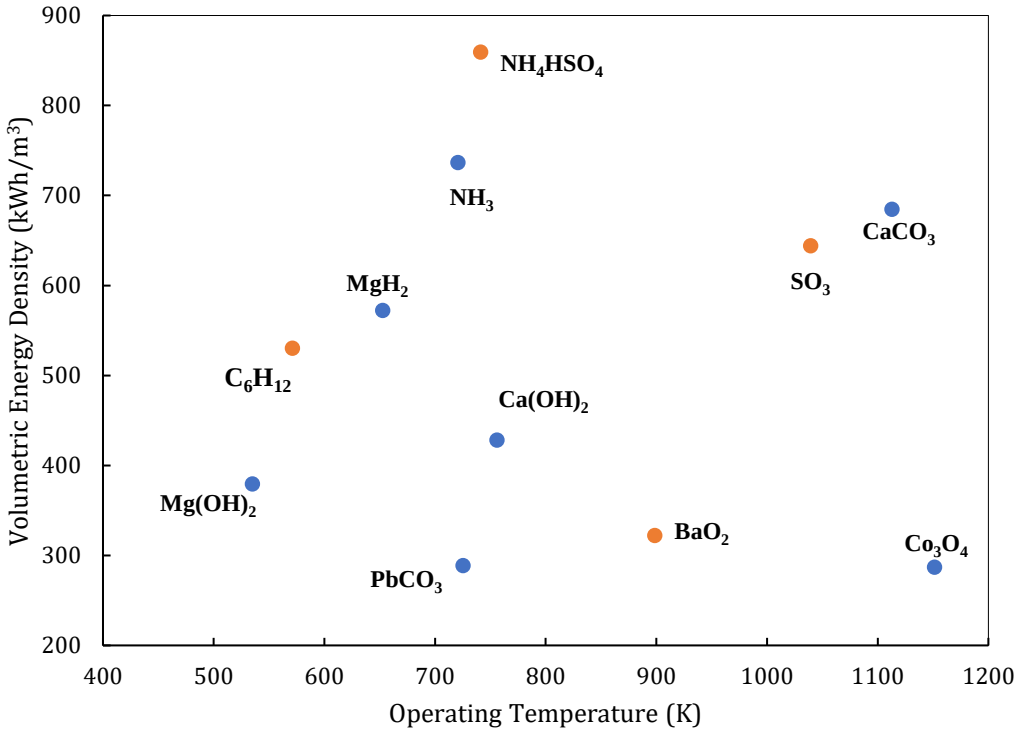

Figure 2.6: Volumetric energy density of some of the thermochemical energy storage material corresponding to its operating temperature [10]

2.3 Metal hydride

Metal hydride (MH) is a compound that contains at least one transition metal and a hydrogen atom or molecule. MHs have demonstrated some distinct advantages over other gas-solid materials, critical for any material used with thermochemical energy storage. MH's, in general, have a high reaction enthalpy and a high volumetric energy density, implying the possibility of cost savings. Additionally, MHs have long been studied as a means of storing hydrogen in mobile applications. As a result, a thorough

understanding of the various MHs materials and reaction kinetics are well developed and known.

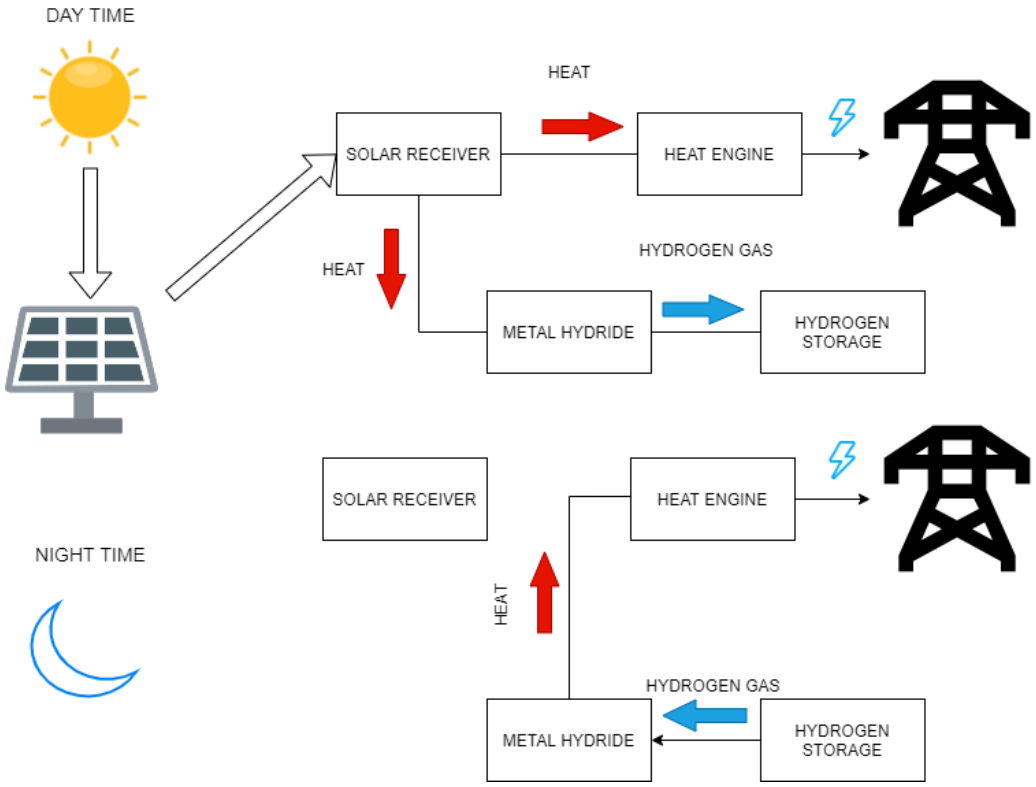

Figure 2.7: Schematic diagram showing the operation of the thermal energy storage system based on metal hydride incorporating the concentrating solar power plant [11]

The energy storage in metal hydride-based thermochemical energy storage is depicted in Figure 2.7. During the daytime, the heat energy is concentrated on the solar receiver using heliostats. A portion of the heat energy produced in the solar receiver is transferred to energy conversion devices to produce electricity. The rest of the heat energy is supplied to the metal hydride reactor for energy storage. By introducing heat energy to the metal hydride reactor, the metal hydride material undergoes a reversible endothermic chemical reaction. As a result of this reaction, metal hydride degenerates into metal and hydrogen gas. The hydrogen gas is then stored separately. Over the night-time period, the stored hydrogen gas is fed back to the reactor which contains the metal porus strudture and undergoes a reversible exothermic reaction. Accordingly, heat energy produced during exothermic reaction from the reactor is used for energy production.

MHs are classified into two categories based on their operating temperatures: low-temperature and high-temperature MHs. MHs materials that work within the room

temperature range (298-373 K) are commonly referred to as low-temperature MHs. Low-temperature MHs are often considered for use as hydrogen storage in mobile application. In general, MHs based on intermetallic alloys such as $LaNi_5$ or Fe-Ti are used in low-temperature applications [12]. By contrast, MHs used in thermal energy storage are usually high-temperature materials. The advantage of using high-temperature MHs for energy storage is that the increased operating temperature of the MHs enhances the efficiency of the heat engine associated with the thermal energy storage system. An increase in efficiency decreases the size of the CSP and reduces the amount of energy storage material used to generate the same amount of electricity.

The investigation of ideal MHs materials for TES has been carried out on a variety of materials with operating temperatures ranging from 533 K (with Mg_2NiH_4) to 1223 K (with LiH). Among the available MHs, magnesium-based MHs have demonstrated potential for thermal energy storage due to their high volumetric and gravimetric capacities, natural abundance of magnesium metal, and ease of processing, all of which contribute to a relatively inexpensive TES. The reversible chemical reaction in the magnesium hydride is expressed as:

$$Mg + H_2 \leftrightarrow MgH_2 + \Delta H \tag{2.5}$$

where ΔH is the reaction enthalpy of hydrogenation.

Since the late 1960s, there has been considerable interest in magnesium-based MH for TES applications, with numerous experimental and numerical studies performed to enhance the thermodynamic, chemical, and heat transfer characteristics. Kawamura et al. [13] carried out an experimental study on a 6.27 kg Mg_2Ni reactor for use in TES with a maximum operating temperature of 623 K. The obtained results suggested that the heat transfer coefficient and the insulation of the rector tank are critical in transferring energy to the HTF. Bogdanović et al. [14] designed and constructed a process steam generator using a MgH_2+ 1–2wt% Ni reactor. The heating output of the heat storage unit was 9.08 kWh at 643 K, and its energy efficiency was 0.796. Later, the energy storage density, thermodynamic properties, operating temperature range, and reversibility of Mg/MgH_2, $Mg\text{-}Ni/Mg_2NiH_4$ for TES were investigated experimentally [15]. Both materials were found to be stable over a temperature range of 523-823 K, with thermal energy densities up to 2.257 MJ/kg. Sekhar et al. [16] examined the effect of hydrogen supply pressure and absorption temperature on the hydrogenation and thermal energy storage coefficients

of a Mg-30% $MmNi_4$ alloy. Under operating conditions of 20 bar of supplied pressure and 423 K absorption temperature, the maximum hydrogen storage capacity of 2.5 wt.% was determined. Thermal energy storage coefficients increased from 0.5 (at 10 bar pressure) to 0.74 at (30 bar pressure) and a 423 K absorption temperature. At a supplied pressure of 20 bar and an absorption temperature of 423 K, the maximum amount of heat stored is approximately 0.714 MJ/kg, with a thermal energy storage coefficient of 0.74.

Paskevicius et al. [6] designed and built a laboratory-scale TES reactor using 20g of magnesium hydride and exfoliated natural graphite (ENG) in a 2250-cm^3 gas tank. Active heat extraction was used to regulate the reactor dynamically. The results indicated that environmental heat loss and powder compaction were the primary determinants of the magnesium hydride reactor's performance. Additionally, Dong et al. [7] constructed another prototype thermochemical reactor using 36 grams of the MgH_2 + TiB_2 + ENG compound. A helical coil heat transfer tube filled with superheated water was used to perform heat exchange during absorption/desorption. The study discovered that by incorporating an internal helical coil heat exchanger, the effective surface area for heat exchange is increased, and the characteristic heat transfer distance is decreased, resulting in an increase in reactor energy efficiency when compared to external heating. Urbanczyk et al. [6] recently demonstrated using a 5 kg Mg_2FeH_6 shell-and-tube reactor for short-term and long-term TES applications at temperatures ~773 K. Molten salt was selected as the heat transfer fluid due to its higher operating temperature. The study discovered that due to heat loss from the system, the reactor only stored 59% of its theoretical heat storage capacity, equating to 1.5 kWh of heat energy.

Due to the complexity of the construction and testing of TES reactors, the numerical investigation has proven to be a valuable method in designing and optimising suitable parameters of the TES. To design MH-based TES accurate in terms of thermodynamics, kinetics, and heat and mass transport, it is essential to use reliable modelling in good agreement with the experimental measurements. Mathematical modelling is an effective method for evaluating and forecasting the state of MH during hydrogenation and dehydrogenation, establishing relationships between various influential factors to optimise the efficiency of the MH storage system. Therefore, experimental studies of MH based reactors suitable for TES applications are supplemented with numerous numerical analyses [17-31].

Generally, the performance of the MH reactor is evaluated based on the de/hydrogenation time and amount of hydrogen to be stored. Multiple parameters affect the performance of the MH reactors, including hydrogen pressure, hydrogen gas inlet temperature, reactor bed initial temperature, flow rate, reactor geometry, and thermal management. The previous studies concluded that the most critical factor affecting the overall performance of the TES is the thermal management system in the MH reactor. As a result, numerous studies have been performed to optimise heat transfer from the MH bed during the hydrogenation and dehydrogenation processes. The majority of thermal management techniques considered are classified into two categories: improving the thermal conductivity of the reactor bed and increasing the effective surface area for heat exchange between the reactor bed and the HTF.

The thermal conductivity enhancement of the reactor bed was achieved through the addition of metal aluminium foam [32], copper wire net structure [33], high conductivity porous matrices [34], expanded natural graphite [35]. Mellouli et al. [34] discovered that adding aluminium foam to a Li-based MH reactor significantly decreases the time required for hydrogenation by 60% as compared to a reactor that does not use aluminium foam. Chaise et al. [35] investigated the impact of incorporating ENG into ball milled magnesium hydride powders. As 20% of ENG is applied, the hydrogenation time is decreased by 25 minutes due to the increased thermal conductivity. The study discovered that using copper finned tubes, a comparable reduction in time can be achieved with 5% of ENG.

The surface area available for heat exchange between the MH bed and the heat collector is improved by using various heat exchanger configurations. Finned heat exchanger tubes [23, 36-38], spiral heat exchangers [39, 40], coiled tubes [41], helical tubes [26, 42], and capillary tubes [43] are all examples of these techniques. Oi et al. [44] used a plate-fin heat exchanger to investigate the heat transfer properties of the MH reactor. Askri et al. [45] developed a model to investigate the dynamic behaviour of various MH reactor designs and discovered that by using a concentric heat exchanger tube fitted with fins and filled with flowing cooling fluid, storage time could be reduced by up to 80%. Dhaou et al. [39] conducted an experimental investigation into embedding a cooling finned spiral tube into MH reactors and discovered that it greatly reduced the time required for the absorption/desorption process. Wu et al. [26] numerically investigated the hydrogen absorption properties of a Mg_2Ni reactor fitted with a helical coil heat

exchanger. The findings indicated that the reactor equipped with a helical coil heat exchanger has significantly superior heat and mass transfer characteristics than the reactor equipped with a straight tube heat exchanger. In effect, integrating a heat exchanger into MH reactors has been shown to significantly improve heat and mass transfer, thereby improving hydrogen storage efficiency.

2.4 Metal Carbonate

Calcium carbonate ($CaCO_3$) is a class of carbonate-based compounds that has attracted considerable attention in recent years as a thermochemical energy storage material for TES application. Due to its high energy density (~3.26 GJ/m^3), widespread availability, nontoxicity, and low cost (~10 $/ton), the $CaCO_3$ compound is an excellent candidate for TES [46]. Additionally, unlike the MH system, which uses flammable hydrogen as the reactant gas, the $CaCO_3$ system uses non-flammable carbon dioxide (CO_2) gas as the reactant gas, enhancing the reactor's safety. The calcium looping process (CaL), based on the carbonation-calcination reaction of $CaO/CaCO_3$, was used to operate the $CaCO_3$ compound for energy storage.

The general equation of the CaL process is expressed as

$$CaO_{(s)} + CO_{2(g)} \leftrightarrow CaCO_{3(s)} \qquad \Delta H_r = -178\ \frac{kJ}{mol} \qquad (2.6)$$

The CaL process is initiated by the decomposition of calcium carbonate ($CaCO_3$) particulate solids in a reactor, which results in the formation of calcium oxide (CaO) and CO_2. This reversible endothermic reaction is called calcination. A significant amount of energy is needed to raise the temperature of the solids stream to the required level for the calcination process, which the CSP plant supplies during the day. As a result, the compound stores the heat energy produced by the CSP plant. The product formed by the calcination process is stored separately. During energy demand hours, previously-stored CaO and CO_2 are circulated into the reactor, where they undergo a reversible exothermic reaction to form $CaCO_3$. This process is known as carbonation. The carbonation reaction generates a considerable amount of heat energy proportional to the reaction's enthalpy, which is later used to produce electricity. [46, 47].

The CaL process has been extensively studied primarily as a method of post-combustion carbon capture in fossil fuel-fired power plants [48-50]. Additionally, it has been

regarded as a technique for enhancing hydrogen production processes by reforming [51, 52]. The CaL process for TES was first proposed by Baker et al. [53] in 1974, and the technique has recently reawakened interest [46, 54, 55]. Edwards et al. [56] proposed a novel CSP plant using CaL and determined the heat and mass balances of the energy storage system. The study found that increasing recyclability (activity levels) of CaO resulted in increased energy efficiency and decreased storage volume. The power efficiencies of the system were estimated to be 40-50%, with recyclability ranging from 15-40%. To continue optimising the energy efficiency of the thermochemical energy storage system, Chacartegui et al. [46, 57] developed a CSP plant using CaL in conjunction with a CO_2 Brayton cycle. The study found that the plant achieved an overall efficiency of 46% at a carbonation pressure of 3 bar. Additionally, four variables were discovered as having a significant effect on the energy storage system's overall efficiency: CaO conversion, turbine pressure ratio, turbine outlet pressure, and carbonator temperature. Alovisio et al. [57] performed a process optimisation analysis on several layout configurations. It was discovered that adding additional gas-solid heat recovery systems increased power production efficiency up to 46% at 50% CaO conversion. Moreover, the previous performance studies of calcium looping technologies in TES applications indicate that the energy density of the system is highly process-and material-dependent [46, 58].

While process engineering studies demonstrate that CaL-based TES is a viable option in plant efficiency and economics, the continuous degradation of multicyclic activity of CaO after each cycle of operation has always hindered it from successful implementation. The recyclability of limestone derived CaO typically reaches 0.07 after 20 cycles of operation [58]. At the TES operating temperature, the recyclability of CaO decreases due to pore plugging phenomena. The ideal TES system integrated into a CSP plant must withstand hundreds of operation cycles without significant loss of CO_2 storage capacity to be economically viable. As a result, various techniques for addressing CaO recyclability have been developed, including hydration, thermal, and mechanical activation [59-64]. These methods, however, were unable to increase recyclability for extended cycles substantially.

On the other hand, our research group has recently found an excellent technique for retaining a high level of multicyclic activity in CaO even after 500 carbonation/calcination cycles [65]. The study examined the influence of various

additives to $CaCO_3$ on the carbonation/calcination reaction's cyclic stability. The results indicated that after 500 cycles of operation, the $CaCO_3$ compound doped with 20% Al_2O_3 or 40% ZrO_2 retained 80% of the multicyclic activity of CaO. This remarkable finding opens up a world of possibilities for CaL-based TES implementation on a large scale. Additionally, due to the superior multicyclic operation of $CaCO_3$ + 20% Al_2O_3 / 40% ZrO_2 compounds, it is vital to explore the effect of various operating parameters on this system.

2.5 Kinetics of gas-solid reaction

The absorption and desorption processes in the thermochemical energy storage system involve an exchange of a significant amount of heat and mass transfer. These processes are coupled with the chemical kinetics of the reaction utilized in the thermochemical material. As a result, efficient reactor modelling and development require a thorough understanding of reaction kinetics and the influence of various operating parameters. The absorption/desorption in both metal hydride and carbon carbonate are gas-solid reactions. The exact reaction kinetics of the materials are essential for the numerical investigation of the thermochemical reactor. As a result, the emphasis of this section is on the kinetics of the gas-solid reaction.

The aim of investigating the reaction kinetics of any gas-solid reaction is to generate an accurate description of the reaction progress under any operating conditions. To determine reaction kinetics, the physical and chemical properties of a sample substance are monitored as a function of time during the absorption and desorption processes. The use of kinetic models to investigate the absorption and desorption behaviour of gas-solid materials is a significant and effective technique for revealing the kinetic mechanism.

2.5.1 Reaction rate equation

Generally, the rate equation of kinetics for a solid–gas reaction is expressed as follows

$$\frac{dx}{dt} = k(T,P)\, f(x) \tag{2.7}$$

where *x* is the reacted fraction at time t, *k* is rate constant, *f(x)* is a function determining the mechanism of the reaction and *g(x)* is the integral form of *f(x)*,

$$g(x) = \int \frac{dx}{f(x)} = kt \tag{2.8}$$

Using the Arrhenius equation, the kinetic coefficient can be expressed as

$$k(T, P) = k_0 f(P) e^{\frac{-E_a}{RT}} \tag{2.9}$$

where k_0 is the pre-exponential factor (also called frequency factor), E_a is the activation energy, and R is the universal gas constant. The pre-exponential factor and activation energy are usually called Arrhenius parameters. The parameters E_a, k_0 and $f(x)$ estimated from the kinetic study has its own theoretical concept. The pre-exponential factor is related to the vibration of the activated complex formed during the reaction. The activation energy is related to the energy barrier that has to be overcome to reactants to form the products, and $f(x)$ is related to the reaction mechanism. Based on the previous studies, a number of kinetics models of the as-solid reaction were proposed [66-68]. Some of the most important kinetics models are listed in Table 2.3. Out of these kinetic models, only some of the classical models are commonly used in reaction modelling.

The absorption/desorption process in a gas-solid material involves a range of concurrent physical and chemical mechanisms and intermediate stages. For example, in a metal hydride system, hydrogen absorption includes physisorption, chemisorption, surface penetration of atomic hydrogen into bulk, hydrogen atom diffusion, and hydride formation at the interface. To interpret these processes during the absorption/desorption process is beyond the scope of this research. Therefore, the current study only intends to formulate the reaction rate equation to incorporate into the numerical modelling of the different types of thermochemical reactors.

Table 2.3: Mechanism function of the kinetics [68]

Model	Differential form, f(x)	Integral form, g(x)
Avrami-nucleation and growth	$(1/r)\,(1-x)\,[-\ln(1-x)]^{1-r}$	$[-\ln(1-x)]^{r}$
	r = 1/4, 1/3, 2/5, 1/2, 2/3, 3/4, 1, 3/2, 2, 3, 4	
Power law	$(1/r)\,x^{1-r}$	x^{r}
	r = 1/4, 1/3, 1/2, 1, 3/2, 2	
Exponential	$(1/r)\,x$	$\ln x^{r}$
	r = 1, 2	
Branching nucleation	$x(1-x)$	$\ln[x/(1-x)]$
Phase boundary reaction	$(1-x)^{r}/(1-r)$	$1-(1-x)^{1-r}$
	r = 1/2, 2/3	
Chemical reaction	$(1/r)\,(1-x)^{r}$	$1-(1-x)^{r}$
	r = 1/2, 2, 3, 4, 1/4, 1/3	
1-D diffusion	$(1/2)\,x^{-1}$	x^{2}
2-D diffusion	$[-\ln(1-x)]^{-1}$	$x+(1-x)\ln(1-x)$
2-D diffusion	$(1-x)^{1/2}[1-(1-x)^{1/2}]^{-1}$	$[1-(1-x)^{1/2}]^{2}$
2-D diffusion	$4(1-x)^{1/2}[1-(1-x)^{1/2}]^{1/2}$	$[1-(1-x)^{1/2}]^{1/2}$
3-D diffusion	$(3/2)(1-x)^{2/3}[1-(1-x)^{1/3}]^{-1}$	$[1-(1-x)^{1/3}]^{2}$
3-D diffusion	$(3/2)[(1-x)^{-1/3}-1]^{-1}$	$1-2x/3-(1-x)^{2/3}$

CHAPTER 3: PERFORMANCE ANALYSIS OF A HIGH-TEMPERATURE MAGNESIUM HYDRIDE REACTOR TANK WITH A HELICAL COIL HEAT EXCHANGER FOR THERMAL STORAGE

3.1 Preface

*This chapter is based on a manuscript published in the International Journal of Hydrogen Energy in 2021 titled "**Performance Analysis of a High-Temperature Magnesium Hydride Reactor Tank with a Helical Coil Heat Exchanger for Thermal Storage**". This chapter contains the same text as the published manuscript, with minor formatting changes to enable thesis referencing.*

Performance Analysis of a High-Temperature Magnesium Hydride Reactor Tank with a Helical Coil Heat Exchanger for Thermal Storage

Arun Mathew [a], Nima Nadim [a], Tilak. T. Chandratilleke [a], Terry D. Humphries [b], Mark Paskevicius [b], Craig E. Buckley [b]

[a] School of Civil and Mechanical Engineering, Curtin University

Curtin University, GPO Box U1987, Perth, WA 6845, Australia

[b] Department of Physics and Astronomy, Fuels and Energy Technology Institute Curtin University, GPO Box U1987, Perth, WA 6845, Australia

3.2 Abstract

Metal hydrides are regarded as one of the most attractive options for thermal energy storage (TES) materials for concentrated solar thermal applications. Improved thermal performance of such systems is vitally determined by the effectiveness of heat exchange between the metal hydride and the heat transfer fluid (HTF). This paper presents a numerical study supported by experimental validation on a magnesium hydride reactor fitted with a helical coil heat exchanger for enhanced thermal performance. The model incorporates hydrogen absorption kinetics of ball-milled magnesium hydride, with titanium boride and expanded natural graphite additives obtained by Sievert's apparatus measurements and considers thermal diffusion within the reactor to the heat transfer fluid for a realistic representation of its operation. A detailed parametric analysis is carried out, and the outcomes are discussed, examining the ramifications of hydrogen supply pressure and its flow rate. The study identifies that the enhancement of thermal conductivity in magnesium hydride has an insignificant impact on current reactor performance.

Nomenclature	
Symbols	
C_P	specific heat capacity, J/kg.K
E_a	activation energy, J/mol
ΔH	molar enthalpy of reaction, J/mol
K	permeability, m^2
wt.	maximum mass content of hydrogen in the metal, %
k	kinetic coefficient, 1/s
k_0	kinetic law coefficient, 1/s
μ	dynamic viscosity of hydrogen, Pa.s
M	molar mass of hydrogen, kg/mol
$\dot{Q}$	heat source, W/m^3
P	hydrogen pressure, Pa
ΔS	reaction entropy, J/ mol. K
R	universal gas constant, J/mol. K
T	temperature, K
t	time, s
$\vec{V}$	velocity vector, m/s
Nu	Nusselt Number
Ra	Rayleigh Number
Pr	Prandtl Number
L_{gas}	typical gas diffusion length, m
λ	thermal conductivity, W/m.K
ρ	density, kg/m^3
ε	porosity
x	relative hydriding fraction: $x = x' / x_{60}$

x_{60}	hydrogenated fraction after 60 min of reaction at a given temperature
x'	hydrogenated fraction
dx/dt	hydriding velocity, 1/s
U	overall heat transfer coefficient, $W/m^2.K$
Subscript	
eq	equilibrium
m	bulk metal
g	gas, hydrogen
e	effective
ref	reference
ini	initial
app	applied
in	inlet
Abbreviation	
HTF	heat transfer fluid
MH	metal hydride

3.3 Introduction

Increasing population growth and rapid technological development are placing excessive strain on current resources of fossil fuels such as coal, oil and gas and hence renewable energy sources are deemed as a sustainable solution to replace them. Among the various types of available renewable energy sources, solar energy is considered to be one of the more feasible options. Nonetheless, the discontinuous nature of this energy form remains a hurdle for its practical transition towards widespread use [69]. In a technological sense, an efficient high-temperature thermal energy storage (TES) system would act to resolve the current mismatching between the solar energy supply and its intended application demand. A TES system could be employed to store the heat produced by a concentrated solar thermal power (CSP) plant, store the excess energy produced by photovoltaic cells, or remove excess energy from the power grid.

TES can be classified into three categories: sensible heat, latent heat and thermochemical energy storage [10]. Among the three, sensible heat is the simplest form of the TES system. Molten salts as TES have been successfully implemented into some commercial CSP plants including the 110 MWe Crescent Dunes CSP plant, Nevada, USA. However, molten salts only offer a low practical thermal storage capacity [12]. This is not an issue for latent heat storage using phase change materials, which have been proven to have a relatively higher energy capacity, but also a high monetary cost and technical challenges due to detrimental corrosion of the plant by the phase change materials [70]. The higher energy density and low cost have made thermochemical energy storage systems more appealing in recent times [10, 12, 71, 72]. The three most common compounds utilised in such a system are metal hydrides (MH), carbonates and hydroxides. Of these, Mg-based hydrides are proven to be an attractive proposition with good energy storage reversibility and cyclic stability at a lower cost [12, 72-76].

A general MH based TES system, to be used in a CSP plant, would absorb heat energy during the daytime and extend the heat storage capacity by employing the reversible chemical reaction where a MH decomposes into metal and hydrogen. During the daytime, an endothermic reaction is employed, and heat is absorbed by the MH and hydrogen is released at a given pressure and temperature determined by the thermodynamic properties of the reaction. Inversely, to recover the stored heat, hydrogen will be fed back to the reactor where it reacts with the metal to form a MH and generates heat energy due to the exothermic nature of the reaction [12, 54].

Magnesium containing MH materials has been under investigation as TES materials since at least 1967 and many systems have been developed [10, 12, 72, 76]. In 1982, Kawamura et al. [13] experimentally tested a reactor containing 3.7 kg of Mg_2Ni alloy and found that heat transfer through the reactor bed is the primary controlling factor in the reaction. Bogdanovic et al. [14] developed a 14.5 kg process steam generator for thermochemical energy storage filled with MgH_2 + 1−2 wt.% Ni, which was cycled 1000 times. Sekhar et al. [16] investigated the effect of both applied hydrogen pressure and absorption temperature on the amount of hydrogen absorbed and the thermal energy efficiency of Mg-30% $MmNi_4$ reactor. Reiser et al. [15] examined the performance of Mg-Fe, Mg-Ni and Mg-Co compounds for energy storage application and concluded that Mg-Fe was a better performing hydride. Sheppard et al. [77] identified that $NaMgH_3$ displays a high enthalpy of reaction (86.6 ± 1.0 kJ/mol H_2) with negligible hysteresis, inferring that it is a promising material for TES applications. Furthermore, a reactor containing 150 g of $NaMgH_3$ was constructed, and more than 40 cyclic de/hydrogenation reactions were performed without major loss in hydrogen storage capacity [78]. A feasibility study was conducted into the performance of $NaMgH_2F$ to provide improved operational conditions over $NaMgH_3$, and its hydrogen desorption properties were measured [79]. Comparison of $NaMgH_2F$ to $NaMgH_3$ revealed the possibility for $NaMgH_2F$ to have an increased operating temperature, stability and exergetic efficiency [80]. Paskevicius et al.[81] designed and constructed a small-scale TES system utilising 19 g of magnesium hydride-based MH inside a tank for CSP application, while Dong et al. [42] designed a 36 g reactor soon after with a helical coil HTF configuration.

Apart from the development of materials and prototype design and manufacture, various numerical investigations on the performance of high-temperature MH reactors for TES have also been carried out [82]. The numerical investigation aids in the understanding of the critical factors influencing the overall performance of the reactors. Muthukumar et al. [83] conducted a numerical study on a $MmNi_{4.6}Al_{0.4}$ based co-axial MH reactor with multiple heat exchanger tubes (12−20) combinations. The overall heat transfer coefficient across each of the cooling tubes was assumed to be 1000 $W/m^2.K$. It was found that the time taken for 90% hydrogenation of the MH bed at 20 bar of hydrogen supply pressure was 296, 222, 195, 184 and 155 s when the number of cooling tubes was 12, 14, 16, 18 and 20, respectively. Mellouli et al. [34] performed a numerical validation of a 2D axisymmetric model of a $LaNi_5$ based MH tank containing metal foam. In this

work, the author performed the sensitivity analysis based on base material, pore size and relative density of metal foam on the hydrogenation process, respectively. The study suggests that the addition of aluminium foam enhances the performance of the reactor by reducing the time required for 90% of hydrogenation of the MH by 60% as compared to a MH tank without the metal foam.

Shen et al. [22] performed 2D axisymmetric mathematical modelling of a high-temperature cylindrical MH tank (L/D = 80/30 mm) with MgH_2 powder and metal foams for heat transfer enhancement, without accounting for the effect of temperature change of the HTF in MH performance. The results showed that the addition of metal foams with a porosity of 0.92 into the reactor resulted in a 40% reduction of reaction time and a 60% improvement in the exothermic power output. Chaise et al. [35] investigated the effect of the addition of expanded natural graphite (ENG) into compacted discs of ball-milled MgH_2. It was found that the introduction of ENG to MgH_2 considerably improves the thermal conductivity of the MgH_2 bed in the normal direction to compression, and the improvement of thermal conductivity is almost linear with ENG content. Moreover, Chaise et al. [19] have conducted an experimental and numerical study on two prototype scale cylindrical reactors (123 g), one filled with Mg-based MH powder and another filled with compacted discs of MgH_2, 4 at.% Ti-V-Cr alloy and 5% ENG. The result showed that due to the addition of the ENG into the second system, faster hydrogenation and dehydrogenation was observed when compared to the first reactor. Bao et al. [84] numerically investigated the influence of some heat transfer enhancement measurements on a high-temperature magnesium hydride-based cylindrical reactor. This included the introduction of circular fins around the heat exchanger tube, the addition of ENG into compacted MgH_2 discs and a combination of circular fins and ENG addition into MgH_2 discs. Overall, the study revealed that the applied heat transfer enhancement techniques reduced the reaction time by 50%. Feng et al. [85] mathematically modelled a high-temperature MgH_2 reactor with proportional-integral (PI) controller to investigate the optimum output temperature setting and the effect of an increase in HTF temperature on the hydrogenation process, based on the gravimetric exergy-output rate (GEOR) [85]. Moreover, the introduction of a tapered hydride bed on the overall performance of the reactor was investigated. Additionally, the introduction of a tapered MH bed structure (L/D_0=600/50) overcomes the adverse effect of non-uniform temperature distribution along the direction of HTF during hydrogenation. It improves the discharging efficiency

of the MH bed from 76 to 90% and GEOR from 35 to 120 W/kg. It identified that the effective heat exchange between the hydride bed and the HTF as one of the key factors affecting the overall performance of the reactor [86]. Therefore, various investigations, both numerical and experimental, have been performed to improve the heat transfer between the MH and HTF. Two methodologies have mainly been adopted for this purpose [87]. Firstly, thermal conductivity augmentation of the MH by incorporating foreign elements with high thermal conductivities such as metal aluminium foam or expanded natural graphite (ENG) [33, 88-91]. Secondly, by improving the effective surface area for a heat exchanger between the MH and heat collector by incorporating extended surfaces like fins and various configurations of cooling tubes [25, 27, 37, 41, 44, 45, 92-99].

Out of these techniques, the helical coil heat exchanger is found to be an attractive option due to its high surface area and the secondary flow associated with it [26, 100-102]. Supporting evidence for this was found in a numerical investigation of the desorption process inside a MgH_2 based reactor equipped with a helical coil heat exchanger, where the performance was shown to be superior compared to other heat exchanger configurations [101]. Wu et al. [26] conducted an optimisation study of a helical heat exchanger used in a Mg-Ni reactor. Their results indicated that a smaller non-dimensional pitch and a smaller helical pitch to helical diameter ratio improves the heat and mass transfer performance. Similarly, a 36 g MgH_2 tank with a helical tube heat exchanger carrying superheated water as the HTF has been constructed and the effects of the internal heat exchanger on the overall performance were studied [42].

However, a mathematical validation of a prototype TES system using a MH reactor with helical coil heat exchanger still remains unexplored. Therefore in this work, 3D modelling of a MH tank containing a magnesium hydride (MgH_2) + titanium boride (TiB_2) + expanded natural graphite (ENG) mixture, equipped with a helical tube heat exchanger, has been developed and utilised to validate a TES prototype reactor constructed by our research group [42]. In estimating the reaction source term, kinetic modelling of the compound is performed. This model is then used for the numerical simulation.

3.4 Numerical modelling

The thermal and fluid dynamic processes in the MH reactor constitute a combined mass and heat diffusion problem with a source term, coupling both equations and accounting for the chemical reaction. The finite volume method is used to solve the equations where material properties of a porous medium, representing the powder, is a key challenge. Additionally, the reaction parameters are required to be quantified and incorporated into a continuum model, conforming to macro-scale assumptions. The model and closures explained below initially require calibration of source terms that account for the chemical reaction. This overcomes the prohibitively complex fully mechanistic approach that would necessitate much extensive knowledge of micro-parameters such as porous structure. Therefore, the kinetic model, which is developed and calibrated in the present study, is based on an empirical examination of a certain reactive material that will be the primary element of simulation and validation.

The calibration process for chemical reaction modelling is performed with the data from a prototype-scale TES reactor, which uses 36 g of ball-milled magnesium-based MH powder containing 0.02 mol.% of TiB_2 and 20 wt.% ENG [42]. The first step towards the modelling of a MH reactor is to identify its kinetics and physical parameters. Thermodynamic properties of magnesium hydride are evaluated in a separate exercise and subsequently used in this study [19].

3.5 Kinetic parameters

Reaction kinetic parameters are sensitive to the particle size of the MH and the synthesis process [68]. This study follows the modelling approach presented by Chaise et al. [19] for magnesium hydride powder. It simply aims to calibrate an empirical closure for a given, but not necessarily for a fully known porous structure. Moreover, the study does not intend to make any interpretation of the fitted models, nor does it investigate the parameters of the MH material used in the experiment. Therefore, magnesium hydride powder with different morphology cannot be used in this problem and the kinetic parameters may not be generalised for certain chemicals.

Approximately 130 mg of MgH_2 ball-milled with 0.02 mol % of TiB_2 and 20 wt. % ENG was used for measuring the isothermal absorption kinetic parameters. Detailed information about the preparation of the material can be found in the literature [42]. A volumetric Sieverts apparatus (High Energy PCTpro E&E) was used with a reservoir

volume of 165 cm^3 and an initial back-pressure of 28, 37, and 45 bar at temperatures of 553, 583, 603, 623 and 653 K. The digital pressure transducer (Rosemount 3051S) deployed had precision and accuracy of 14 mbar.

The measurement revealed that most of the metal had undergone hydrogenation within 60 min of initiating the process. According to the model published by Chaise et al. [19], a variable $x = x'/x_{60}$ was introduced, where 'x" is the hydrogenated fraction and 'x_{60}' is the value at t = 60 min. The data measured at three different pressures and temperatures were fitted to various kinetic models – Avarami type nucleation growth model with multiple exponent values, 3D diffusion and power-law shows that the n = 2 model fits linearly amongst the other models as evident from Figure 3.1.

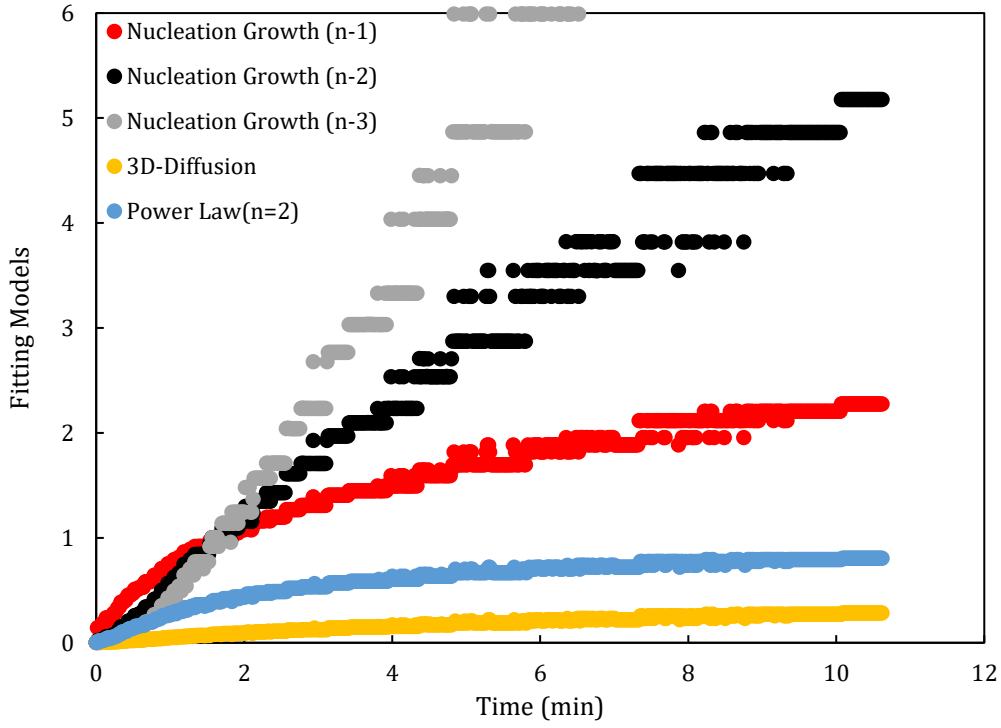

Figure 3.1: Comparison of the degree of fit of different kinetic models

It is found that Avrami-type nucleation and growth model with exponent 2 gave the best linear fit for the most part of the hydrogenation process. The linearised plot based on this model at different temperatures is depicted in Figure 3.2.

$$\left(-ln(1-x)\right)^2 = k(T,P)t \tag{3.1}$$

where k (1/s) is the kinetic coefficient. The pressure-dependent term is also calculated from different pressure absorption test data at 603, 623, and 653 K. Figure 3.3 shows the linear relationship with coefficient k and pressure difference ($P-P_{eq}$).

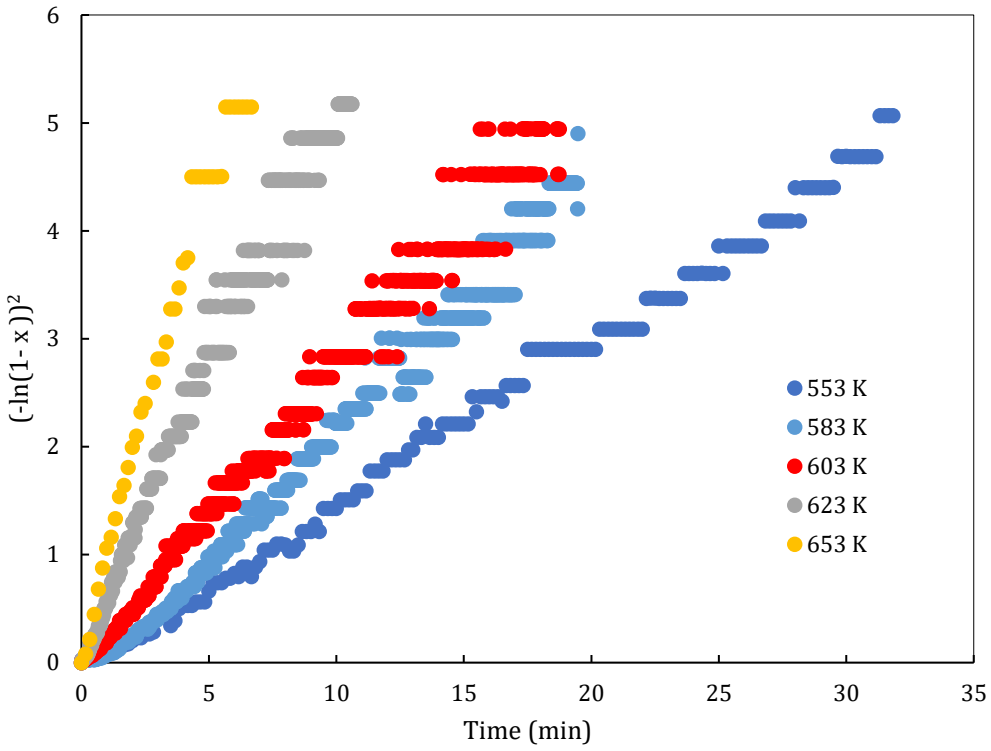

Figure 3.2: Avarami type nucleation growth model (exponent = 2) at different temperatures

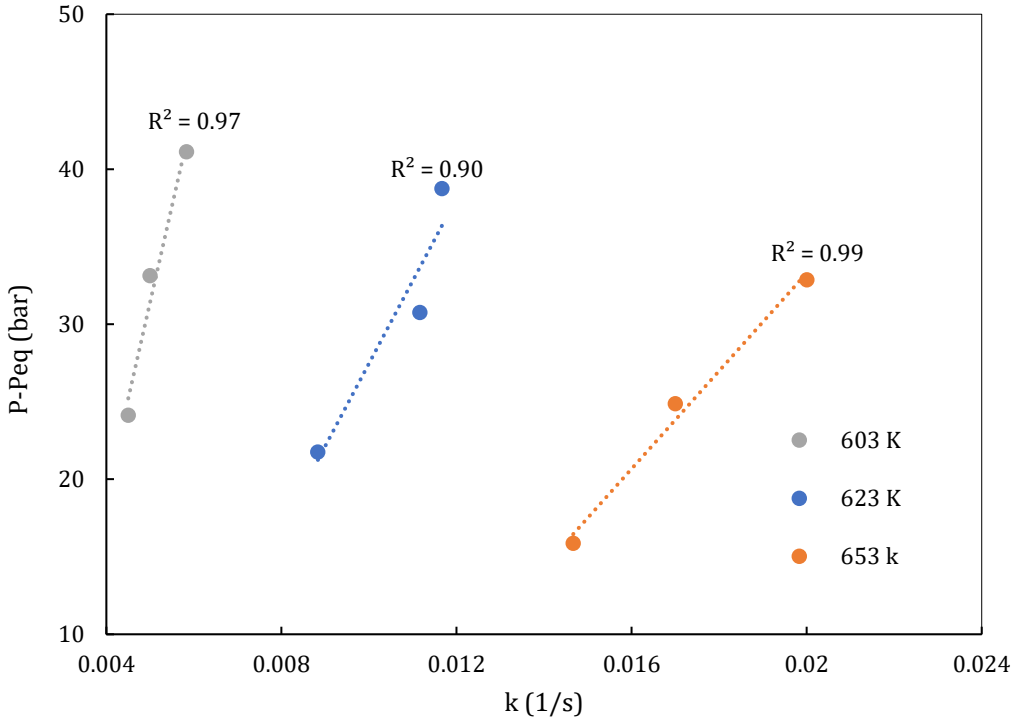

Figure 3.3: Kinetic coefficient vs. pressure depend term at different temperatures

By using the Arrhenius equation

$$k(T,P) = k_0 f(P) e^{\frac{-E_a}{RT}} \tag{3.2}$$

where k_0 (1/s) is the kinetic law coefficient.

where

$$f(P) = \left(\frac{P - P_{eq}}{P_{eq}}\right) \tag{3.3}$$

$$\frac{dx}{dt} = k_0 \frac{(x-1)}{2ln(1-x)} \left(\frac{P - P_{eq}}{P_{eq}}\right) e^{\frac{-E_a}{RT}} \tag{3.4}$$

Plotting (ln (k)−ln (($P-P_{eq}$)/P_{eq})) against (1/T) gives the value of activation energy (E_a) and pre-exponential factor (k_0) at different pressures. The values obtained are listed in Table 3.1. These values vary marginally over the pressure range. The extrapolated values of E_a and k_0 within the experimental pressure range were found to be 141 kJ/mol H_2 and 3×10^9 s^{-1}, respectively.

Table 3.1: Values of activation energy and kinetic law coefficient at different pressures

Pressure (bar)	E_a (kJ/mol H_2)	k_0 (s^{-1})
28	144.37	3.19 x 10^9
37	145.45	3.22 x 10^9
45	146.17	3.29 x 10^9

3.6 Thermal conductivity

The estimation of thermal conductivity in a MH powder is a critical requirement that will influence the numerical modelling outcomes. However, this presents inherent difficulties as the porous structure may not be precisely described or even maintained consistently during the manufacturing process, thus introducing uncertainties. During the manufacture of TES reactors, the MH powder was compacted into the reactor by hand pressing, which makes it practically impossible to maintain uniform compaction of MH powders, especially around the helical heat exchanger tube [42]. Therefore, this study incorporates a sensitivity analysis to ascertain the uncertainty of thermal conductivity.

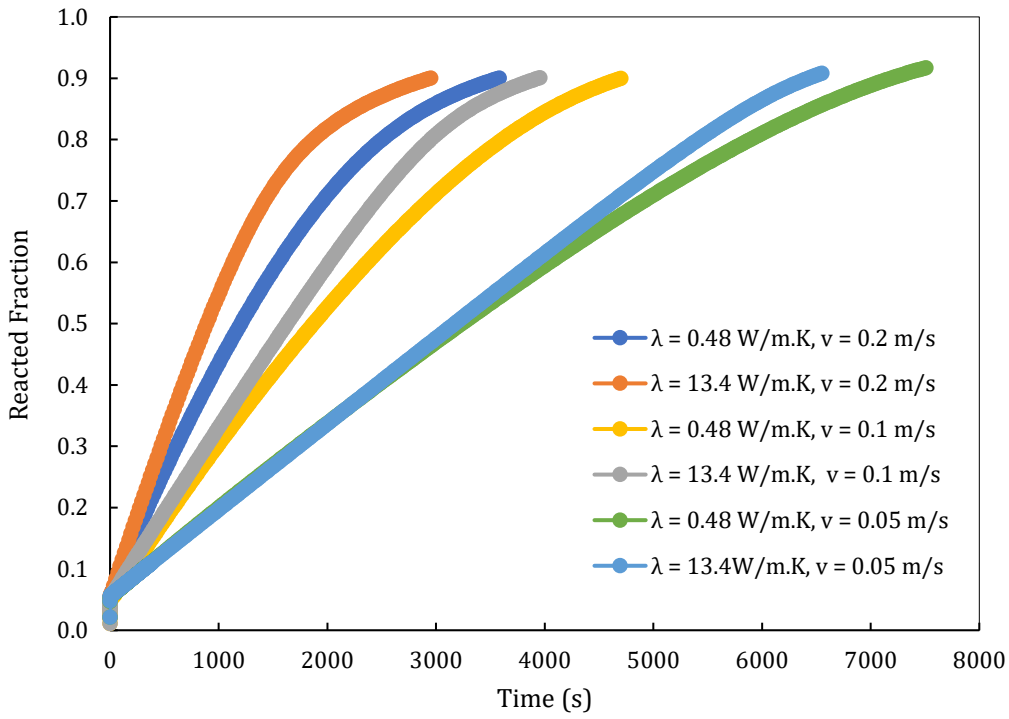

Figure 3.4: Examination of reaction rate versus thermal conductivity in an axisymmetric model

The thermal conductivity of MgH_2 powder without ENG was measured previously by Chaise et al. [19] to be 0.48 W/m.K. This value was adjudged as the lowest possible thermal conductivity of the current mixture. The radial thermal conductivity of the pelletized MH with 20% ENG was measured at 20 bar of hydrogen supply pressure and found to be 13.4 W/m.K [103]. This was the highest possible value used for the thermal conductivity in numerical modelling. It is anticipated that the effective thermal conductivity of the current mixture is in between these two values.

In line with this, an axisymmetric model is utilised to assess the influence of the effective thermal conductivity, in the various operating conditions. The simulated geometry consists of a heat transfer pipe (ID = 0.6 mm, OD = 1.6 mm) centrally embedded in the MH chamber of cylindrical shape (D = 20.6 mm, L = 240 mm). The rates of reacted fractions have been monitored for combinations of heat transfer flow rates and conductivity values. The results could be mandated as a general (i.e. regardless of reactor geometry) observation indicating the effective thermal conductivity to be more crucial when the flow rate of HTF is higher. This sensitivity to thermal conductivity diminishes as the flow rate decreases, and accordingly, heat collection rate reduces.

3.7 Model Description

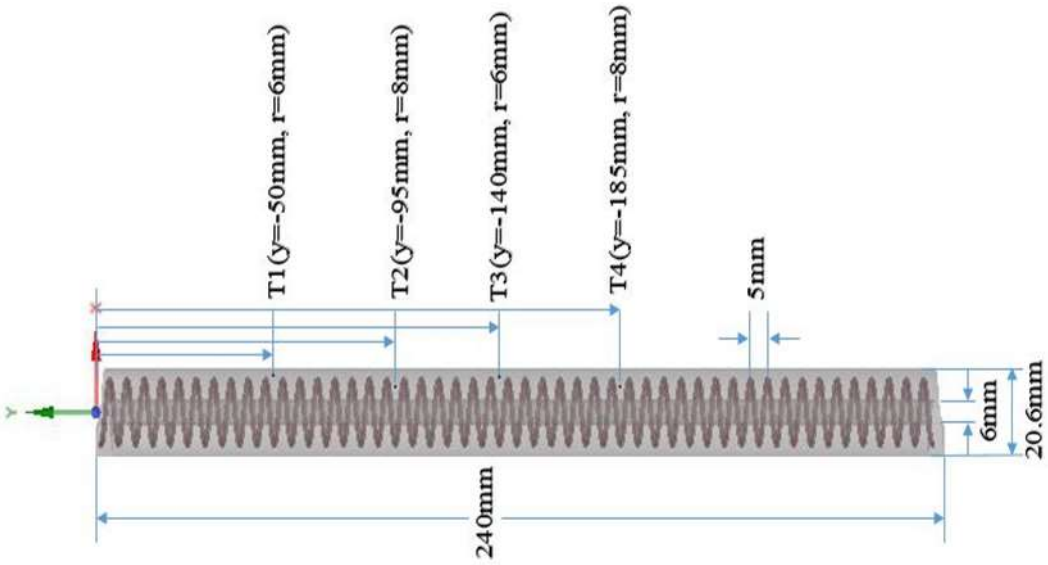

Figure 3.5: Schematic representation of the MH reactor with a helical tube heat exchanger

The schematic diagram of the MH reactor used in this model is shown in Figure 3.5, which is based on the design used by Dong et al. [42]. Overall, the height of the reactor is 240 mm, the outer diameter is 20.6 mm and the inner diameter is 6 mm, respectively. Hydrogen is fed into the reactor through a porous filter from the centre. Superheated water is used as the HTF in the reactor, which flows through a helical tube with a helical diameter and pitch of 15 mm and 5 mm, respectively, the inner diameter of 0.6 mm with a thickness of 0.5 mm. Four thermocouples (T_1, T_2, T_3, and T_4) are placed from top to bottom of the reactor with their positions depicted in Figure 3.5. The reactor is covered with 5 mm thick insulation material (Insulfrax LTX Blanket: grade 128).

3.8 Governing Equations

The heat and mass transfer processes within the MH reactor with a helical coil heat exchanger are modelled as a three-dimensional simulation during the hydrogenation process. For this simulation, the modelling cannot be simplified with constant heat flux or constant wall temperature boundary conditions at the HTF tube surface due to the nature of thermal generation within the reactor. The following assumptions are made to formulate and manage the complexities involved in the processes in line with published work [19, 21, 23, 104]:

- Hydrogen is considered as an ideal gas within the operating conditions of the reactor;
- Local thermal equilibrium is valid between hydrogen and powder particles;
- Radiative heat losses are neglected;
- The thickness of the reactor wall of the MH tank is neglected;
- Thermophysical properties of all materials except the HTF is constant;
- Hydrogen flow is neglected. According to Chaise et al. [21], the influence of the hydrogen flow on the reaction process can be ignored if the value of the dimensionless parameter, $N = \frac{\lambda_m . M . L_{gas}^2 . \mu}{P_{eq} . \frac{\Delta H^2}{RT^2} . K . L_{heat}^2 . \rho_{gas}}$ is less than 0.1, and,
- The volumetric expansion of the MH during absorption is neglected.

3.8.1 Metal hydride

Energy conservation equations for hydride bed:

$$(\rho C_P)_e \frac{\partial T_m}{\partial t} = \boldsymbol{\nabla} . (\lambda_e \boldsymbol{\nabla} T_m) + \dot{Q} \tag{3.5}$$

where $\dot{Q}$ is the source term which is expressed as,

$$\dot{Q} = (1 - \varepsilon) \rho_m wt \frac{dx}{dt} \frac{\Delta H}{M_g} \tag{3.6}$$

with the effective volumetric heat capacity as,

$$(\rho C_P)_e = (\varepsilon \rho C_P)_g + \left((1 - \varepsilon) \rho C_P\right)_m \tag{3.7}$$

The effective thermal conductivity is given by as,

$$\lambda_e = \varepsilon \lambda_g + (1 - \varepsilon) \lambda_m \tag{3.8}$$

The equilibrium pressure is determined by the Van't Hoff equation as,

$$\frac{P_{eq}}{P_{ref}} = exp^{\left(\frac{\Delta H}{RT_m} - \frac{\Delta S}{R}\right)} \tag{3.9}$$

where the reference pressure P_{ref}= 1 bar

3.8.2 Heat transfer fluid

Continuity equation for the HTF is described as

$$\nabla.\left(\rho\vec{V}\right)_{HTF} = 0 \tag{3.10}$$

The HTF flow through the helical tube is expressed by the Navier-Strokes equation as,

$$\rho_{HTF}\left(\frac{\partial\vec{V}_{HTF}}{\partial t} + \left(\vec{V}_{HTF}.\nabla\right)\vec{V}_{HTF}\right) = \left(\mu_{HTF}(\nabla^2\vec{V}_{HTF})\right) - \nabla P_{HTF} + (\rho_{HTF}g) \tag{3.11}$$

The energy equation of the HTF is given as,

$$\frac{\partial(\rho C_P T)_{HTF}}{\partial t} + \nabla.(\rho C_P\vec{V}T)_{HTF} = (\lambda\nabla^2 T)_{HTF} \tag{3.12}$$

3.8.3 Initial conditions

During the practical experiments, the MH was cycled, i.e. underwent both dehydrogenation and hydrogenation processes. The hydrogen pressure at the end of the dehydrogenation process was 9.58 bar, which is taken as the initial hydrogen pressure for hydrogenation.

The initial temperature of the MH reactor is found to be non-uniform over the length of the reactor. This temperature is a function of distance from the top of the cylinder. This is evidenced by the sudden drop of HTF temperature during the absorption process following desorption. Therefore, a linear relationship is used to express the initial temperature of the MH reactor in the model as,

$$T_{ini}(z) = 650.87 + (0.06083z) \tag{3.13}$$

where the initial reacted fraction of the MH reactor is taken as X_{ini} = 0.01. The maximum value of z = 0 and then goes to the negative value. The unit of 'z' in millimetres.

3.8.4 Boundary conditions

The hydrogen pressure applied in the reactor behaves transiently since the hydrogen is supplied from a tank with a fixed volume. The fitting equation (6^{th} order polynomial function) for the applied pressure is formulated by using MATLAB curve fitting tool (cf tool), and the degree of fit of the equation is ≈ 99 %. This transient pressure equation is only used for the validation against the experimental result.

$$P_{app} = \big((-3.35 \times 10^{-23}\, t^6) + (1.047 \times 10^{-18}\, t^5) - (1 \times 10^{14}\, t^4) + (2.99 \times 10^{-12}\, t^3) + (4.97 \times 10^{-7}\, t^2) - (2.99 \times 10^{-3}\, t) + 9.581\big) \times 10^5 \quad (3.14)$$

The adiabatic boundary condition is applied at the top and bottom walls of the MH reactor.

$$\frac{\partial T_{(y_{top})}}{\partial y} = 0, \frac{\partial T_{(y_{bottom})}}{\partial y} = 0 \quad (3.15)$$

The Churchill and Chu correlation [105] is used for the convective heat transfer calculation. These values are implemented in each time step at the outer boundary wall of the reactor by using a user-defined function (UDF).

$$Nu = 0.68 + \frac{0.67 Ra^{\frac{1}{4}}}{\left(1 + \left(\frac{0.492}{Pr}\right)^{\frac{9}{16}}\right)^{\frac{4}{9}}} \quad (3.16)$$

The heat transfer between the MH bed and HTF is expressed as,

$$-\lambda_e \frac{\partial T}{\partial r} = U(T_m - T_{HTF}) \quad (3.17)$$

where *U* is the overall heat transfer coefficient, determined by elements of internal flow convection and conductive resistance induced by the pipe thickness.

The inlet temperature and the velocity of HTF are taken as T_{in} = 598 K and V_{in} = 0.2358 m/s, respectively.

Outlet boundary of the HTF is defined by,

$$\boldsymbol{\nabla}.(\lambda_{HTF} \boldsymbol{\nabla}.T_{HTF}) = 0 \quad (3.18)$$

3.9 Numerical Procedure

The computational domain was generated by using commercial software DesignModeler, while the mesh was generated using ANSYS Meshing software. The model was numerically solved using a commercial finite volume software package, ANSYS Fluent Version 17.2. The reaction rate of hydrogenation, equilibrium pressure, the initial

temperature of MH bed and convective heat transfer value at the boundary surface of the reactor were incorporated through the user-defined functions (UDF). Second-Order Upwind and QUICK schemes were used to solve the momentum and energy equations, respectively.

3.10 Meshing Strategy

The three-dimensional geometry, along with the dynamic boundary, parametric and operating conditions (heat transfer coefficient boundary, HTF properties and applied hydrogen pressure), in the mathematical model demands an efficient meshing strategy for the current problem for preventing improper handling of a large number of control volume elements and reducing computational time. Therefore, the sweep meshing strategy was implemented along the helical fluid flow path to reduce the number of volume elements and to increase the hexagonal elements that are effective in lessening the computational time without compromising the quality of the mesh.

As shown in Figure 3.6, the geometry is divided into two regions. The first or top part consists of the HTF, HTF tube and the MH surrounding the HTF tube. The second or bottom part comprises only MH, which is not included in the first part of the domain. This division facilitates better control over the mesh elements along the entire length of the reactor. Thermal coupling is adopted in the model for the contact interfaces between the porous region and the HTF tube wall, and also the HTF tube wall and the HTF. Some important properties of the mesh elements are listed in Table 3.2. It is observed that the laminar flow through the helical coil is not influenced by the mesh elements, therefore in that region, the use of a fine meshing may not be required in the given geometry.

Table 3.2: Important properties of the generated grid

Percentage of hexagonal elements	99.60
Average skewness	0.19
Average orthogonal quality	0.95
Average aspect ratio	4.84

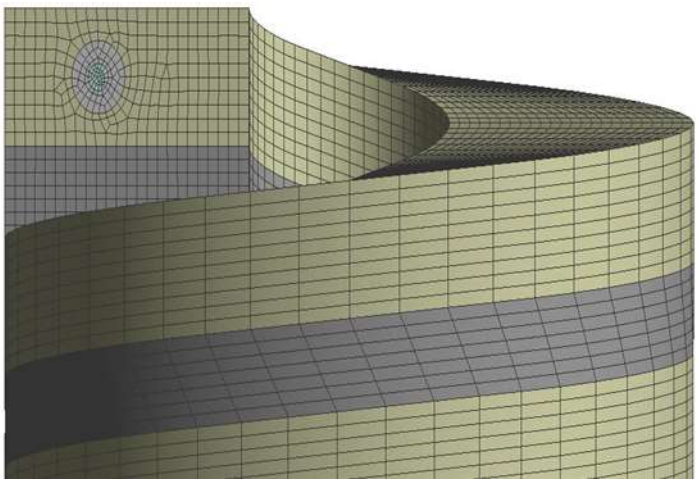

Figure 3.6: Mesh pattern for the MH reactor

Table 3.3: Parameters used in the mathematical model [19, 42]

Enthalpy of absorption (J/mol. H_2)	ΔH	−75000
Entropy of absorption (J/K/mol. H_2)	ΔS	−135.6
Density of MH (kg/m^3)	ρ_m	1800
Specific heat capacity of MH (J/kg.K)	C_{P_m}	1545
Porosity	ε	0.66
Gravimetric H_2 storage capacity (wt.%)	$wt.$	6
Hydrogen specific heat capacity (J/kg.K)	C_{P,H_2}	14000
Molecular weight of hydrogen (kg/mol)	M_{H_2}	0.002
Gas constant (J/mol K)	R	8.314
Dynamic Viscosity of Hydrogen (kg/m.s)	μ_{H_2}	8.9 x 10^{-6}
Thermal conductivity of Hydrogen (W/m.K)	λ_{H_2}	0.24
Thermal conductivity of Insulator (W/m.K)	λ_{ins}	0.065
Specific heat capacity of Insulator (J/kg.K)	$C_{P_{ins}}$	1000
Density of Insulator (kg/m^3)	ρ_{ins}	128
Ambient temperature (K)	T_{amb}	298

The properties of the HTF significantly varied within the experimental temperature range (520- 645 K) [106]. Hence, piecewise-linear and piecewise-polynomial functions were used in the model and listed in Tables 3.4 and 3.5.

Table 3.4: Piecewise-linear functions to describe the properties of HTF [106]

Properties	Data Points	
	520 K	645 K
Density (kg/m^3)	822.35	465.21
Thermal conductivity (W/m.K)	0.6459	0.4087
Viscosity (kg/m.s)	11.235	5.3635

Table 3.5: Polynomial function to describe the specific heat of HTF [106]

Temperature Range (K)	Polynomial function
520− 620	$C_p = (0.2852\,T^2) - (302.41\,T) + 84886$
620− 635	$C_p = (9.9784\,T^2) - (12331\,T) + 3816745$
635− 645	$C_p = (33.3493\,T^3) - (63801.15\ T^2) + (4.0687x10^7\ T\ ) - (8.6488x10^9)$

3.11 Results and Discussion

The processes within the MH reactor could be reviewed by evaluating the characteristics of temperature and the reacted fraction as two key indicators of thermo-chemical phase-change, across the entire reactor. Figure 3.7 and 3.8 illustrates the variation of temperature and reacted fraction during the hydrogenation process at time intervals of 1 s, 500 s, 1000 s, 2000 s, 3000 s and 4000 s, respectively. The temperature contour at 1 s indicates that there is a sudden rise in temperature in the reactor during the initial phase of the reaction. This occurs due to the presence of a large initial gradient in the applied pressure and equilibrium pressure of hydrogen. Subsequently, the temperature of the MH bed gradually decreases with respect to the reaction rate as the reaction progresses. This behaviour can be seen from the shift in temperature colour contour from red to blue

region with increasing time. Towards the end of the reaction, the temperature of the reactor drops below the inlet temperature of the HTF due to the heat loss from the reactor to its surroundings. It is important to notice that unlike previous simulations which assume adiabatic boundary condition, the radial temperature gradient in this case is negligible due to the combined effect of heat loss to the surroundings in addition to the heat exchange to the HTF from the MH bed and the shorter distance between the HTF and MH bed in the radial direction [26, 102]. Moreover, due to the consideration of the temperature rise of the HTF, the variable temperature contours were visible from top to bottom in the axial direction at different time steps.

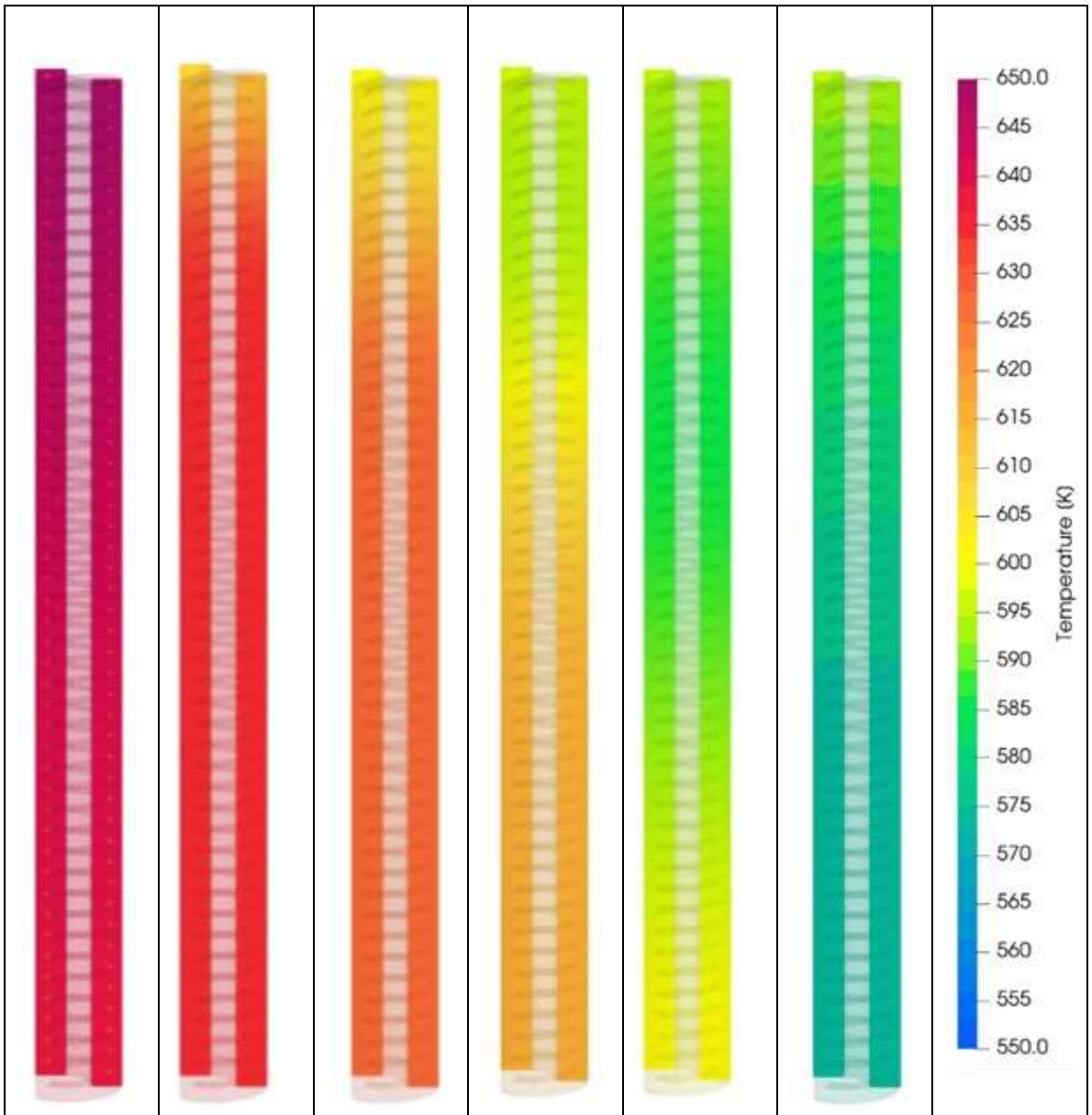

Figure 3.7: Distribution of the reactor temperature at various time intervals

Figure 3.8 represents the behaviour of the reacted fraction, as a scalar ranged between 0.01 and 1. As the reaction progresses, it is noted that the reacted fraction is always higher in the top region (i.e. closer to the HTF inlet) due to the greater heat exchange between the MH and the HTF compared to the bottom region. Therefore, the material in the top part of the reactor reaches the maximum value of the reacted fraction, before gradually propagating towards the bottom part.

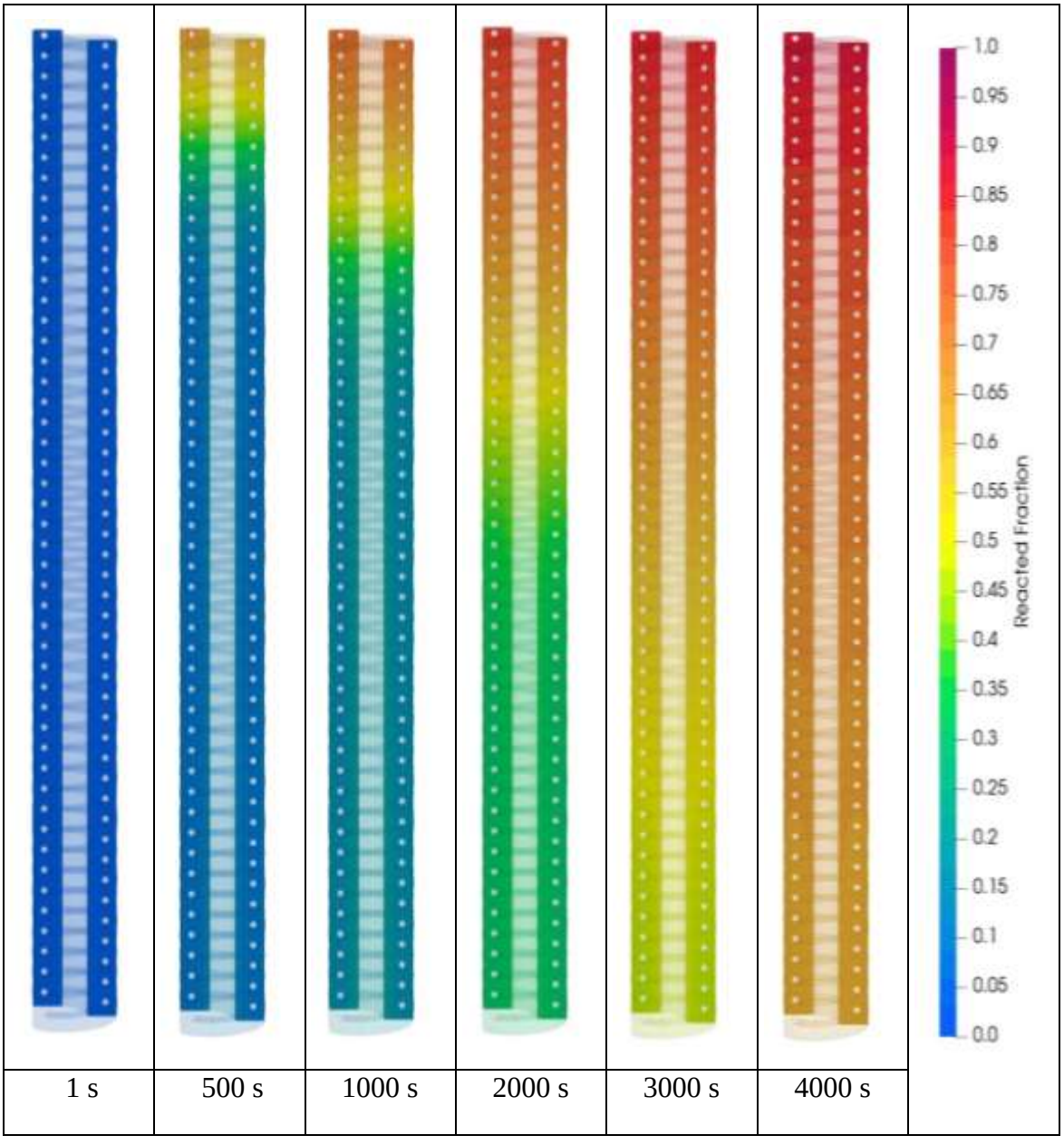

Figure 3.8: Distribution of the reacted fraction at various time intervals

Similar to the temperature contour shown in Figure 3.7, the reaction front, in this case, is also negligible in the radial direction due to negligible temperature gradient in the radial

direction, whereas it is significant in the axial direction due to the rise in temperature of the HTF. This variation of reacted fraction in the axial direction would not be observed if the temperature of the HTF was not considered in the modelling.

3.11.1 Sensitivity to thermal conductivity of metal hydride

Theoretically, a higher thermal conductivity of the MH is expected to improve reaction kinetics and improve the reactor performance. Based on this rationale, many studies have been conducted by introducing thermal conductivity enhancement techniques, such as the addition of metal mesh or ENG to the TES material [22, 23]. While determining the sensitivity of the system to thermal conductivity, the current simulation was carried out by considering the lowest and highest possible thermal conductivity values at a pressure of 9 bar hydrogen back pressure, under adiabatic operating conditions. The results thus obtained are depicted in Figure 3.9 for the temperature at two thermocouples positions (T1 and T4, Figure 3.4), for the two different conductivity values. From Figure 3.9, it is noticeable that the temperature variation at two different thermocouple positions in the MH bed only shows a marginal difference for the two thermal conductivity values chosen.

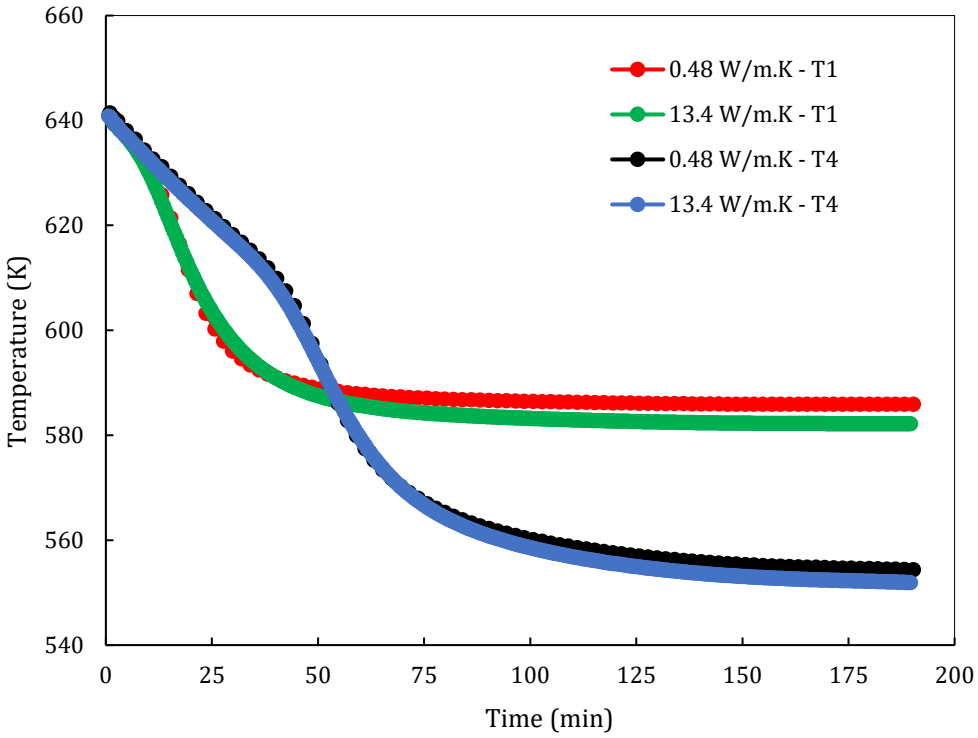

Figure 3.9: Comparison of temperature at two positions (T1 and T4) at two thermal conductivity values

Additionally, Figure 3.10 illustrates the volumetrically averaged reacted fraction over time, for the maximum and minimum thermal conductivities. It appears that this second key attribute of the process is impassive to the variations in MH thermal conductivity of the MH bed. Therefore, it can be stated that the addition of thermal conductivity enhancement materials does not benefit the TES material in the current reactor.

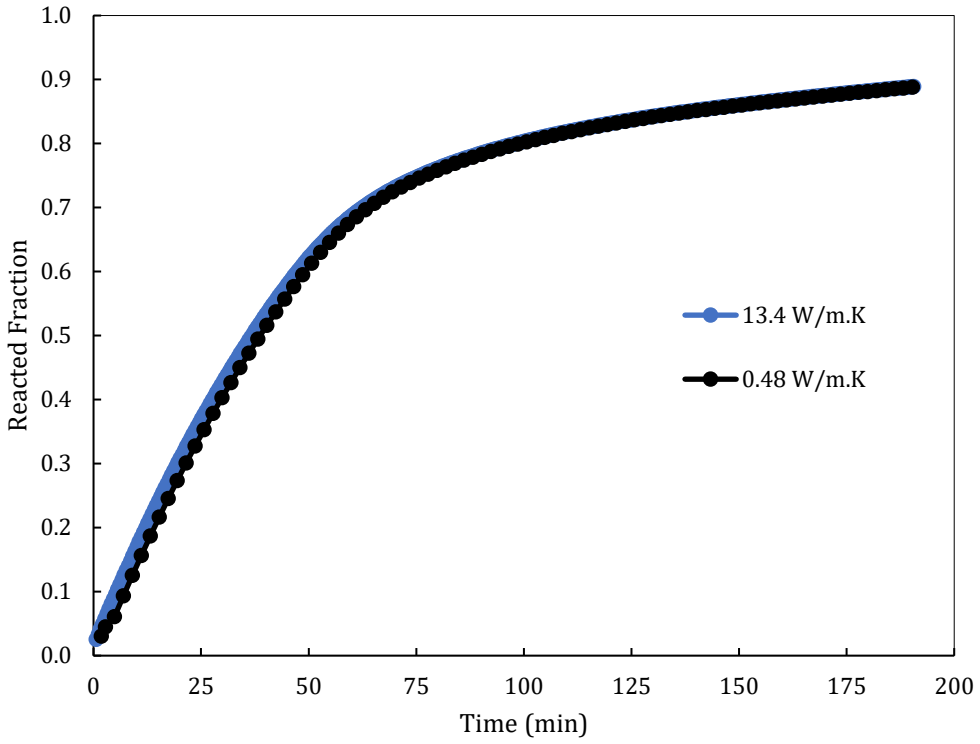

Figure 3.10: Comparison of volumetrically averaged reacted fraction at two thermal conductivities

Figure 3.11 compares the HTF outlet temperature for the two different conductivity values. It is observed that there is not any significant deviation in temperatures caused by variation in the MH thermal conductivity. The outlet temperature of the HTF is the most significant parameter from the point of view of thermal power generation and it is confirmed that this parameter is insensitive to the thermal conductivity of the current MH. It is evident from Figures 3.10 and 3.11 that all of the examined parameters are almost identical when studied at the two thermal conductivity values. This indicates that the thermal conductivity is not a major influencing factor on the thermal performance of the reactor. Therefore, any value of thermal conductivity within the range of 0.48 to 13.4 W/m.K is reasonable for the simulation validity check. Moreover, it can be concluded that the effectiveness of the addition of ENG (or any other thermal conductivity enhancing material) to TES materials should be examined on a case by case basis as the

addition of material only reduces the available energy density, hence inversely affecting on the overall performance of the MH reactor.

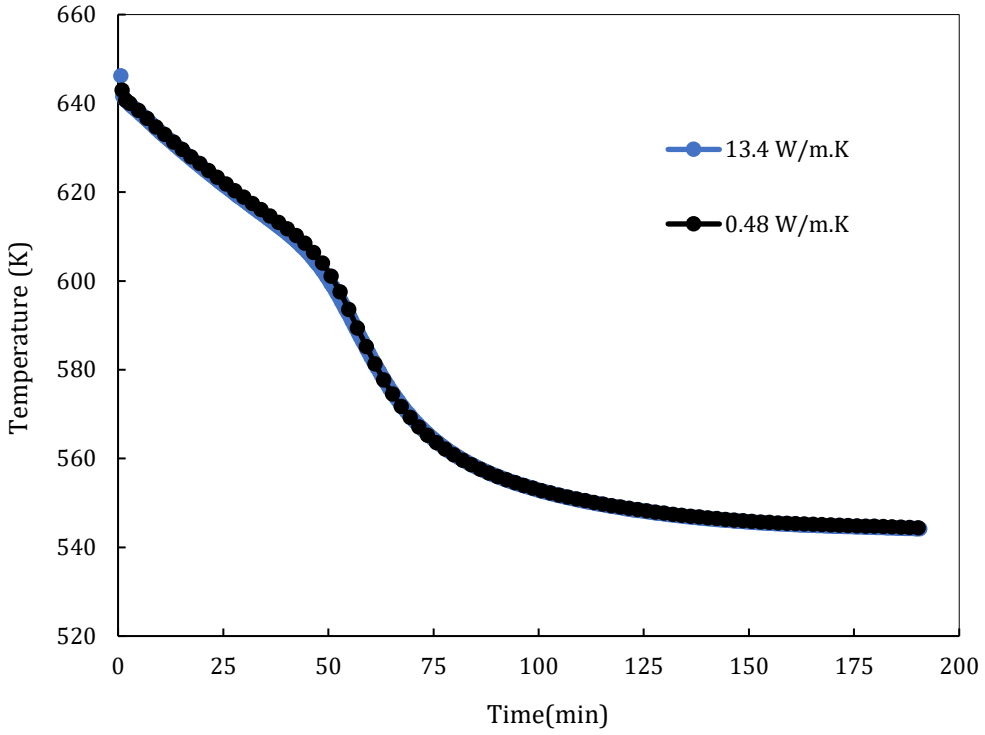

Figure 3.11: Comparison of outlet temperature of HTF at two thermal conductivities

3.11.2 Validation

The validation of the Computational Fluid Dynamics model was carried out by comparing simulated temperatures with the experimental values measured on a prototype MH reactor at the positions of four given thermocouples (T1 to T4) [42], as shown in Figure 3.12. The operating conditions for validation are given in Table 3.6.

Table 3.6: Operating conditions for validation.

Initial hydrogen pressure	9.58 bar
Initial reacted fraction	0.01
Velocity of HTF flow	0.2358 m/s
Initial temperature of HTF	598 K
Initial temperature of MH	$650.87 + (0.06083z)$

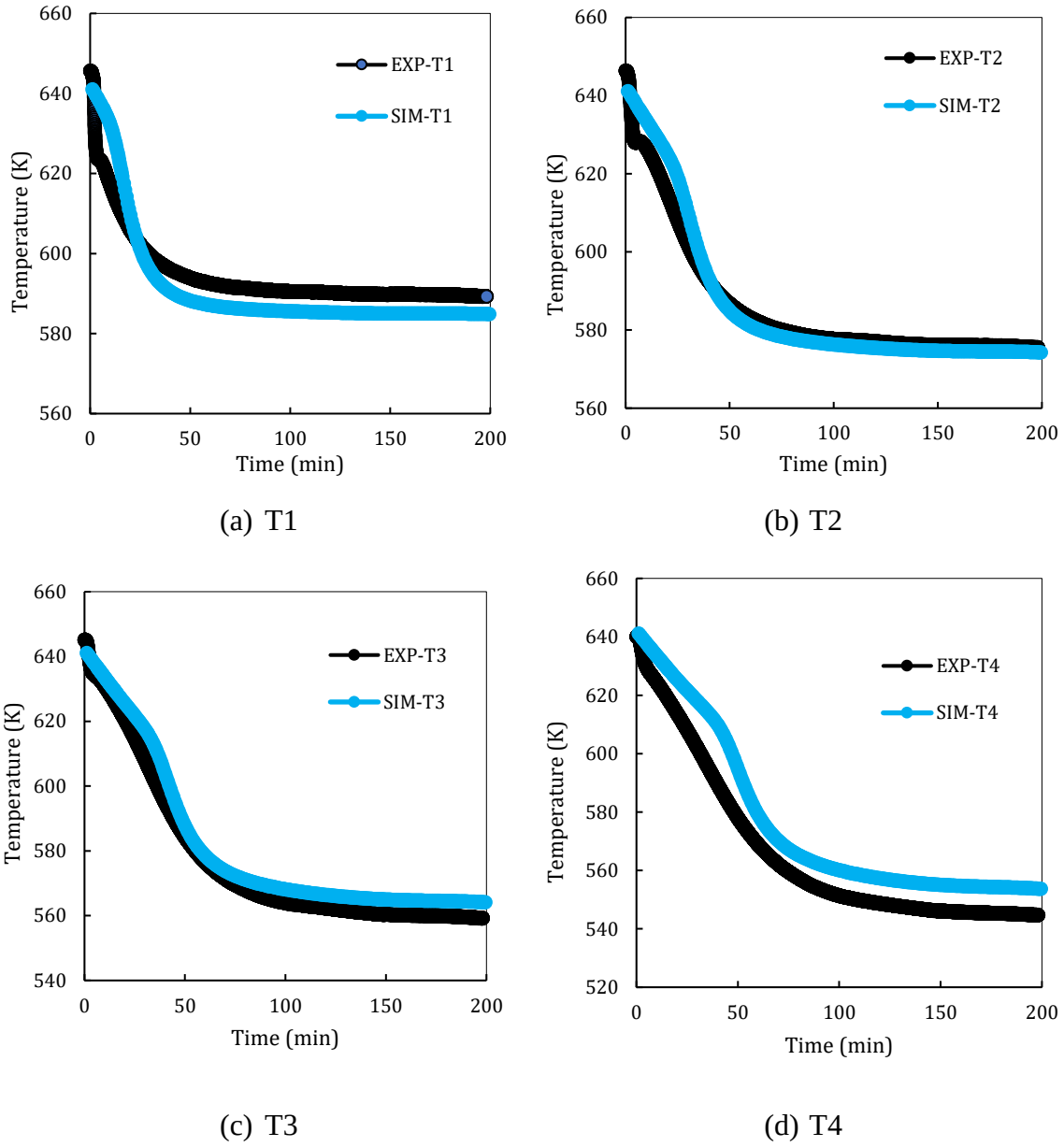

Figure 3.12: Temperature profile during hydrogenation of the MH bed at four thermocouple locations

It is clear from Figure 3.12 that the numerical simulation corroborates the experimental data under similar operating conditions. The slight mismatch observed may be attributed to the uncertainties involved in the kinetics measurements and the assumption of uniform porosity in the model. For the parametric analysis below, all the simulations described were carried out at adiabatic boundary conditions.

3.11.3 Effect of HTF flow rate

The effect of the HTF flow rate was investigated by evaluating the average reacted fraction of the MH, rate of heat absorption by the HTF and the outlet temperature of HTF at three HTF flow rates of 4, 7 and 10 ml/min (Figures 3.13 to 3.15). In all cases, a constant hydrogen pressure of 9.5 bar and inlet HTF temperature of 598 K was applied. Figure 3.13 illustrates the effect of the HTF flow rate on the averaged reacted fraction of MH in the reactor. It can be seen that faster hydrogenation occurs for higher HTF flow rates. It is evident that ≈90% hydrogenation occurs in 50 minutes when the flow rate is 10 ml/min, whereas the same level of hydrogenation takes 100 min for a HTF flow rate of 4 ml/min. Overall, increasing the flow rate by 2.5 times from 4 ml/min to 10 ml/min decreases the time by 50% to achieve 90% hydrogenation threshold.

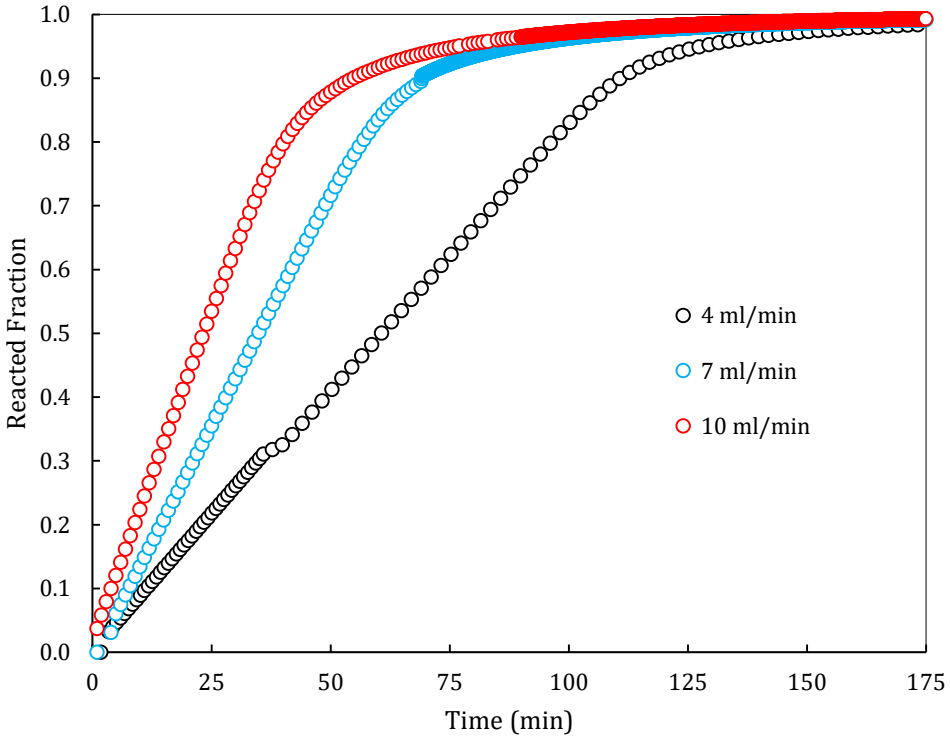

Figure 3.13: Comparison of averaged reacted fraction at different HTF flow rates

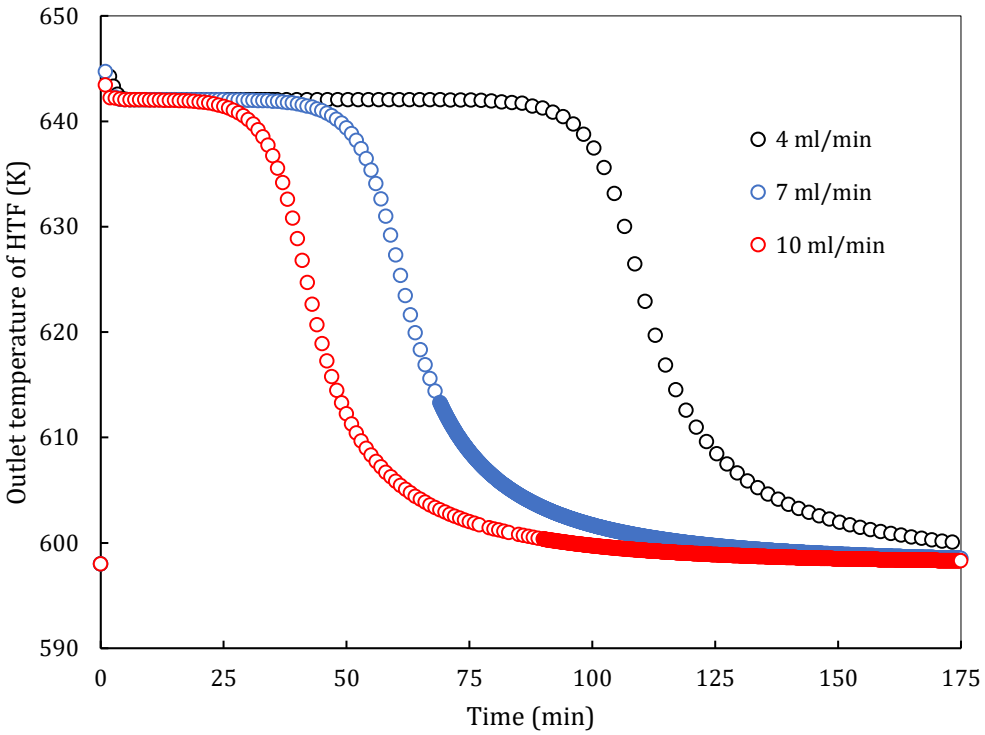

Figure 3.14: Comparison of outlet temperature of HTF at various flow rates

Figure 3.14 represents the effect of the HTF flow rate on the outlet temperature of HTF. At the beginning of hydrogenation, the outlet temperature of the HTF was identical (≈598 K) for each of the three flow rates. The initial temperature is expected to be identical as the system is in equilibrium with no reaction occurring. After 25 min with a flow rate of 10 ml/min, the HTF outlet temperature rapidly drops, while for a flow rate of 4 ml/min, this temperature drop occurs only after 95 min. This result is attributed to the higher flow rate causing faster heat exchange between the MH and HTF, hence accelerating the hydrogenation process and causing the reaction to reach completion in a shorter time span. This assumption is illustrated in Figure 3.15, where the effect of flow rate on the rate of heat absorption by the HTF during the hydrogenation process is plotted over time. It can be seen that the rate of heat transfer between the MH and HTF during the initial phase of the hydrogenation increases with higher flow rates. For a flow rate of 10 ml/min, the heat transfer rate remains at ≈35 W for 20 min and then rapidly decreases with time. However, for a flow rate of 4 ml/min, the highest heat transfer rate achieved is 14 W, of which is maintained for ≈100 min.

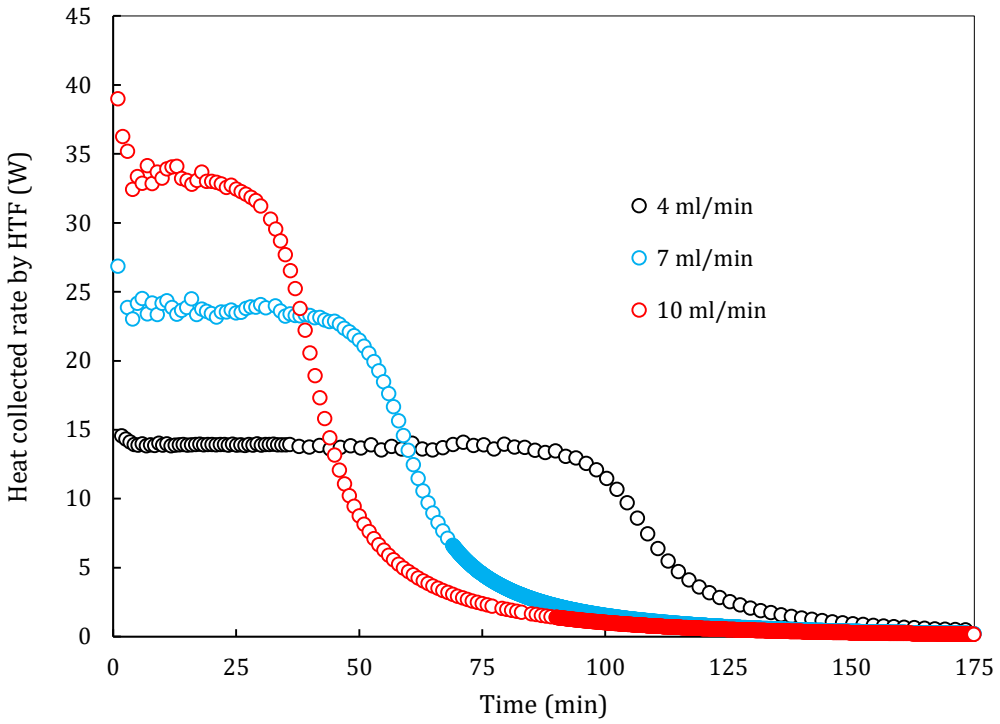

Figure 3.15: Comparison of heat absorption rate by HTF at various flow rates

3.11.4 Effects of hydrogen supply pressure

Using the computational simulation developed, a parametric analysis of hydrogen supply pressure on the MH reactor performance was evaluated using three constant hydrogen pressures of 7, 8 and 9 bar. The effect on the reacted fraction, the rate of heat absorption and the HTF outlet temperature are shown in Figures 3.16 to 3.18. The flow rate and the HTF inlet temperature were taken as 4 ml/min and 598 K, respectively. Figure 3.16 indicates that a higher initial hydrogen pressure gives rise to a faster reaction rate in the reactor, thereby shortening the time for hydrogenation. It is evident that a 23% increase in applied hydrogen pressure reduces the hydrogenation time by about 37%. This is due to the fact that higher hydrogen supply pressure induces a larger gradient between applied pressure and the equilibrium pressure required to trigger the absorption process.

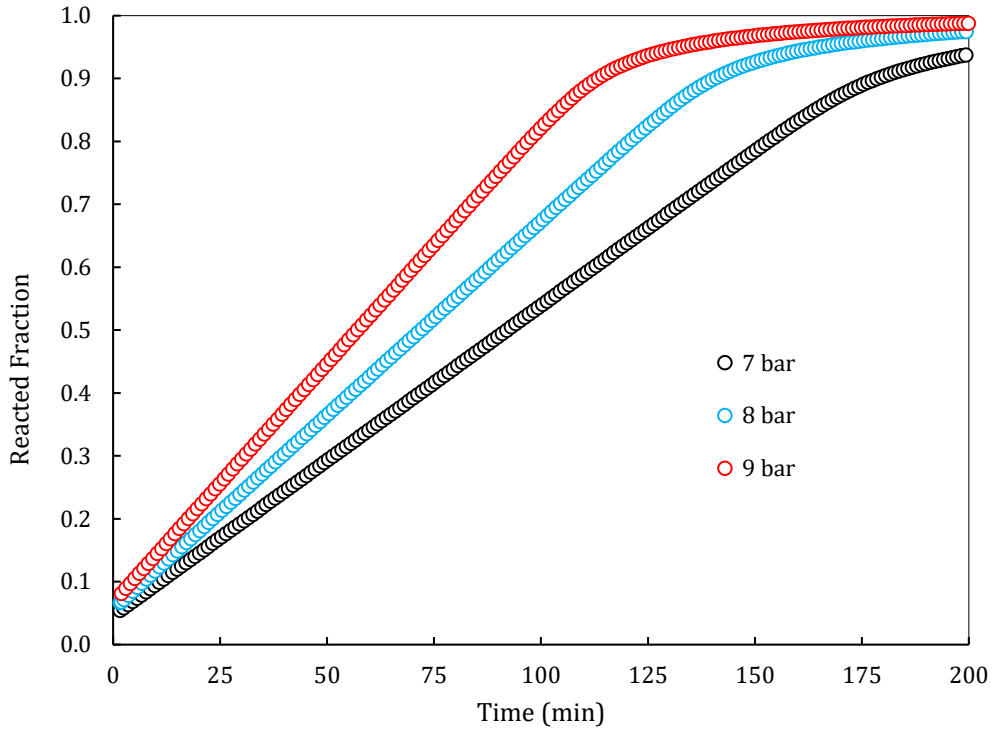

Figure 3.16: Comparison of averaged reacted fraction at different hydrogen supply pressures

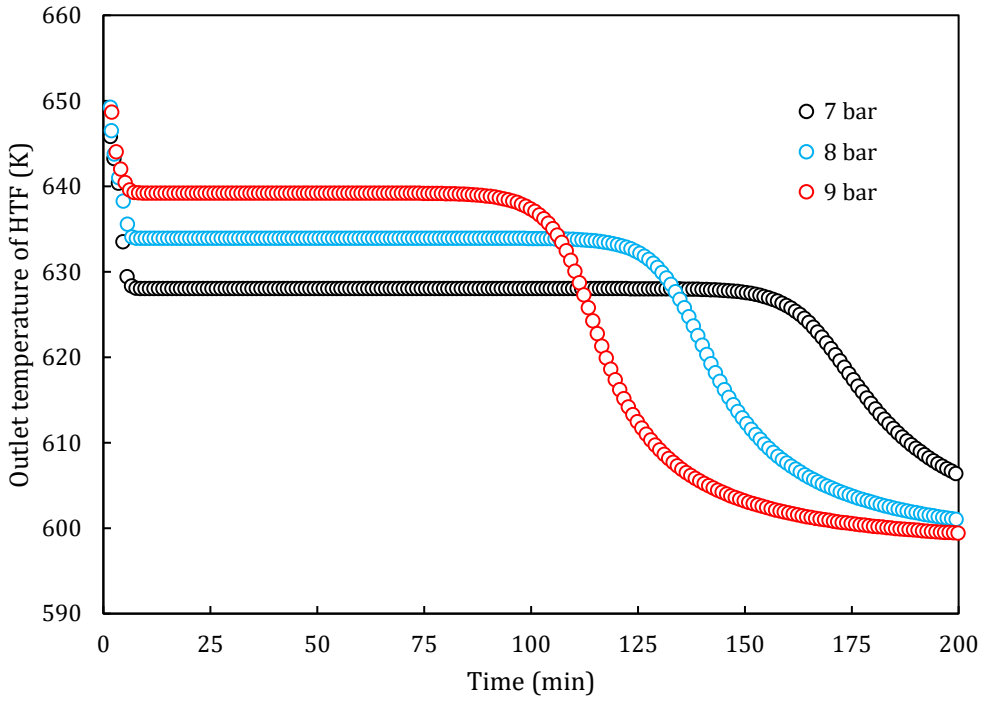

Figure 3.17: Comparison of outlet temperature of HTF at different hydrogen supply pressures

Figure 3.17 shows the effect of hydrogen supply pressure on the HTF outlet temperature. In all the cases shown, the maximum outlet temperature of HTF is ≈ 648 K for a few minutes from the beginning of hydrogenation. When the supply pressure is 9.0 bar, the outlet temperature rapidly falls from the peak value to 638 K and stays there for the next 90 min. However, when the hydrogen pressure is 7.0 bar, the peak temperature drops to ≈ 628 K and is held for a longer time of 150 min.

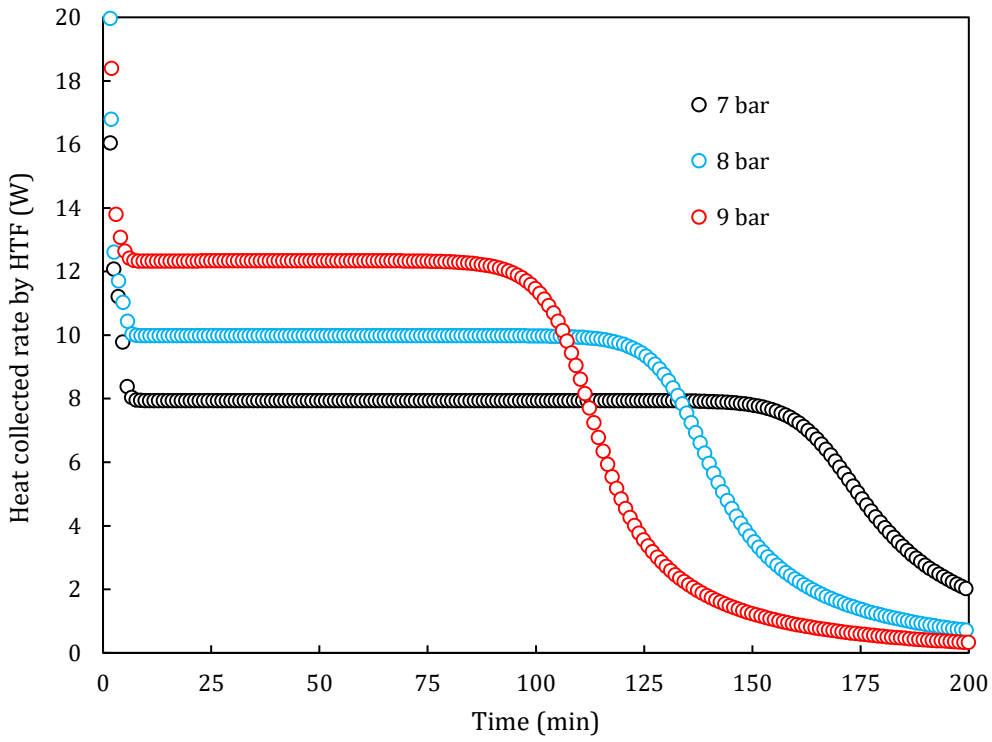

Figure 3.18: Comparison of rate of heat absorption by HTF at different hydrogen supply pressures

Figure 3.18 indicates the heat collected by the HTF for varying hydrogen supply pressures. It is evident that a higher operating pressure results in rapid heat collection by the HTF within a shorter time duration, whereas a low pressure impedes the heat absorption rate, but the effective heat collection period is extended. Similar to the outlet HTF temperature illustrated in Figure 3.17, the heat transfer rate into the HTF reaches a maximum during the initial phase of the reaction and remains at that level for some time before falling off towards the end of the reaction. In the case of higher pressure, the heat transfer rate shows a higher value and retains that value for a shorter duration, whilst the converse is observed at lower pressures.

3.12 Conclusions

This study has developed an accurate three-dimensional computational fluid dynamics model for simulating MH reactors to be used as thermal batteries to store thermal energy produced by concentrating solar thermal power plants or store excess energy from the grid as heat. In particular, this model describes a reactor filled with MgH_2 along with 0.02 mol% TiB_2 and 20 wt.% ENG, with an embedded helical coil heat exchanger using superheated water as the HTF. The model accounts for the diffusive heat transfer within the reactor and reaction kinetics, with the kinetic model being experimentally derived to ensure that the model could be validated against experimental results. The validated model was used to evaluate thermal performance with parametric analysis enabling the following key conclusions:

- Upon analysing the effect of the HTF flow rate on the averaged reacted fraction of MH, a 50% reduction in time for hydrogenation was determined when a flow rate of 10 ml/min was used compared to 4 ml/min. Moreover, a flow rate of 10 ml/min allows for a maximum heat absorption of 35 W compared to 14 W at 4 ml/min. Increasing the flow rate did not alter the initial outlet temperature of HTF.
- Initial hydrogen supply pressure increases the reaction kinetics for hydrogen absorption into the MH TES material. A 37% reduction in hydrogenation time was determined when supply pressure was increased from 7 bar to 9 bar. Unlike the parametric study of variable flow rate, the outlet temperature of the HTF was increased upon an increase of hydrogen pressure. An increase in heat energy absorbed by the HTF was also observed with pressure increase.
- Magnesium hydride powder is often mixed with ENG to increase the thermal conductivity of the powder bed. This study showed that using a thermal conductivity of 0.48 or 13.8 W/m.K did not improve the current TES reactor performance.

3.13 Conflicts of interest

There are no conflicts to declare.

3.14 Acknowledgements

The authors CEB, TDH, and MP acknowledge the financial support of the Australian Research Council (ARC) for ARC Linkage grants LP120101848 and LP150100730. CEB, TDH and MP acknowledge financial support from the Department of Industry Innovation and Science for the 2019 Global Innovation Linkage (GIL73589) grant. MP acknowledges his ARC Future Fellowship FT160100303. This work was supported by resources provided by the Pawsey Supercomputing Centre with funding from the Australian Government and the Government of Western Australia.

CHAPTER 4: INVESTIGATION OF BOILING HEAT TRANSFER FOR IMPROVED PERFORMANCE OF METAL HYDRIDE THERMAL ENERGY STORAGE

4.1 Preface

This chapter is based on a manuscript published in the International Journal of Hydrogen Energy in 2021 with the title ***"Investigation of boiling heat transfer for improved performance of metal hydride thermal energy storage"****. The text of this chapter is identical to that in the published paper, with minor formatting adjustments to allow for thesis referencing.*

Investigation of Boiling Heat Transfer for Improved Performance of Metal Hydride Thermal Energy Storage

Arun Mathew [a*] , Nima Nadim [a], Tilak. T. Chandratilleke [a] , Terry D. Humphries [b], Craig E. Buckley [b]

[a] School of Civil and Mechanical Engineering, Curtin University

Curtin University, GPO Box U1987, Perth, WA 6845, Australia

[b] Department of Physics and Astronomy, Fuels and Energy Technology Institute Curtin University, GPO Box U1987, Perth, WA 6845, Australia

4.2 Abstract

The inherent nature concerning the intermittency of concentrating solar power (CSP) plants can be overcome by the integration of efficient thermal energy storage (TES) systems. Current CSP plants employ molten salts at TES materials although metal hydrides (MH) have proven to be more efficient due to their increased operating temperatures. Nonetheless, the heat exchange between the MH bed and the heat transfer medium used to operate a heat engine is a critical factor in the overall efficiency of the TES system. In this work, a computational study is carried out to investigate the performance of a magnesium hydride TES packed bed using a multiphase (boiling) medium instead of single-phase heat absorption methods. The boiling heat transfer behaviour is simulated by using the Eulerian two-fluid framework. The simulations are conducted at a transient state using SST-*k*-ω Reynolds-Averaged Navier-Stokes equations. It is observed that, unlike the single-phase heat collection method, the multiphase heat absorption method maintains a constant temperature in the heat transfer fluid throughout the reactor. Consequently, a higher temperature gradient is realised between the MH bed and heat transfer fluid (HTF), leading to improvements in the overall reaction rate of the hydrogenation process.

Nomenclature

Symbols

C_P	Specific heat capacity, J/kg.K
E_a	Activation energy, J/mol
ΔH	Molar enthalpy of reaction, J/mol
wt	maximum mass content of hydrogen in the metal, %
k_0	kinetic law coefficient, 1/s
μ	dynamic viscosity of hydrogen, Pa.s
$\dot{Q}$	heat source, W/m^3
P	hydrogen pressure, Pa
ΔS	reaction entropy, J/ mol. K
R	universal gas constant, J/mol. K
T	temperature, K
t	time, s
$\vec{v}$	velocity vector, m/s
λ	thermal conductivity, W/m.K
ρ	density, kg/m^3
ε	porosity, dimensionless
dx/dt	hydriding velocity, 1/s
V	volume, m^3
m	mass flow rate, kg/s
h	heat transfer coefficient, $W/m^2.K$
A	area, m^2
ξ	area influence coefficient

d	Diameter, m^2
f	drag function, dimensionless
η_b	bubble relaxation time
α	volume fraction, dimensionless
Ja	Jacobs number, dimensionless
Re	Reynolds number, dimensionless
Pr	Prandtl Number, dimensionless
γ	Thermal diffusivity
Subscript	
eq	Equilibrium
m	bulk metal
g	gas, hydrogen
e	effective
ref	reference
l	liquid phase
v	vapour phase
sat	saturation
w	wall
E	evaporative
b	bubble
Abbreviation	
HTF	Heat transfer fluid
MH	Metal hydride

4.3 Introduction

An ever-increasing energy demand caused by population growth and technological advancement is a critical issue currently challenging humanity. In the long term, this energy demand cannot be entirely met by fossil fuels alone due to their resource limitations and the resulting environmental impact. Therefore, it is of paramount importance and essential that sustainable energy production systems are developed through renewable energy sources for future benefits. When considering various eco-friendly energy solutions, solar energy is regarded as one of the most promising and practically feasible options due to its vast expanse of global abundance [69]. However, in the absence of appropriate energy storage options, the inherent intermittent nature of solar energy practically hinders the potential use of this infinitely vast energy resource for uninterrupted energy production.

Efficient thermal energy storage (TES) is an attractive proposition to overcome the intermittency issue of solar power as a primary source for renewable energy production. Therefore, much research is currently being conducted to develop TES materials and Thermal Batteries [72, 107-111], wherein there are three categories of TES materials: sensible, latent, and thermochemical energy storage. Among the three options, thermochemical energy storage has major competitive advantages, including higher energy density and cheaper raw materials, making it more cost-effective in the future over other systems [10, 12, 71].

Among various media tested for thermochemical energy storage materials, metal hydrides (MH) have found to be an attractive option due to their favourable thermophysical properties [72, 81, 112-119]. MH based TES system is ideally suited as the primary energy storage component of concentrated solar power (CSP) plants and operates as follows: A solar receiver collects thermal energy from sunlight and is transferred to MH using a heat transfer fluid (HTF) [10, 12, 72]. Due to the thermodynamic properties of the MH, under specific pressures and temperatures, an endothermic reaction is initiated causing hydrogen to be released from the MH. The hydrogen generated is then collected and stored until it is subsequently required. During the night-time or off-peak hours, the stored hydrogen is reintroduced to the MH tank, where the material reacts with hydrogen triggering an exothermic process reforming the

original MH material. The heat generated from this reaction is then transferred to a heat engine, such as a Stirling engine, to produce electricity [54, 55, 120].

Previous studies have identified that, apart from developing MH materials that reversibly store hydrogen at the desired operating temperatures (>773 K), efficient heat exchange in the MH reactor is a crucial factor in improving the overall efficiency of the TES. Therefore, numerous investigations have been performed to improve the heat transfer characteristics within the MH bed [82, 87, 121]. These studies can broadly be classified into two major categories. The first category is the optimisation of the surface area for heat exchange in the MH reactor, that is mostly been realised by varying the geometry of MH bed, heat exchanger tubes or by the introduction of extended surfaces on either the MH tank or on the heat transfer tubes (e.g. fins) [23, 26, 95, 122-126]. The second category is the enhancement of thermal conductivity of the MH bed using a metallic mesh or carbon-based components including exfoliated natural graphite (ENG) or carbon nanotubes etc. [23, 30, 127-129].

The energy extracted by the HTF from the high-temperature MH reactor during the hydrogenation process has previously been investigated [23, 25, 42, 82]. In this process, the thermochemical energy produced by the MH is absorbed as sensible heat through the tubing that carries the HTF. Due to the temperature rise of the HTF as it flows through the reactor, the temperature gradient between the MH bed and HTF at the reactor outlet is always less than that at the inlet. The reaction rate, which is directly proportional to the temperature gradient between the MH bed and HTF, is reduced in the region close to the HTF outlet compared to the inlet. The adverse effect of the rise in temperature of HTF would be marginal in prototype scale reactors, and as such, the drop in performance of the MH reactor due to the temperature gradient has not been taken into consideration in previous studies. However, this effect could play a significant role in the overall system performance when scaling up the MH reactor for commercial application.

Two options are available to overcome the adverse effects of the temperature gradient between the HTF and reactor bed on the overall MH reactor performance. Firstly, this can be achieved by introducing a high HTF flow rate through the heat collector tubes. Thus, a constant HTF temperature can be maintained throughout the reactor. However, this method is not suitable for energy conversion devices associated with TES because it works based on the energy density of the HTF. Another option is to induce boiling heat

transfer inside the HTF tube. During the boiling heat transfer process of the HTF, a phase change of the HTF occurs from its liquid state to vapour state. The fluid, therefore, undergoes a latent heat absorption process and thus remains at a constant temperature. Therefore, a constant temperature gradient between MH bed and HTF would be achieved throughout the whole length of the reactor, unless superheating of the vapour occurs.

Realisable potential for enhanced performance of an MH reactor from convective boiling of HTF has never been examined. Bridging the knowledge gap, this study investigates the multiphase heat transfer characteristics of a magnesium hydride bed with convective boiling fluid flow that would mechanistically improve the reaction rate and reduce the time required to complete the hydrogenation process. A comparative numerical study of sensible and latent heat absorption on the MH reactor performance is also performed. Whilst the modelling of boiling process itself is an arduous task due to several concurrent physical processes in liquid-to-vapour phase change, additional complexities inherent to such simulation for it necessitates a transient energy source to represent the MH Bed hydrogenation process.

4.4 Boiling heat transfer process

Being a multiphase flow comprising of liquid and vapour phases in a fluid, boiling typically offers very large magnitudes of heat removal rates from a heated wall to a fluid with a small temperature difference. The boiling heat transfer characteristics are much regulated by whether the bulk liquid is below the saturation temperature (subcooled boiling) or near the saturation temperature (saturated boiling). The boiling process is initiated when the local wall temperature of heated surface reaches the saturation temperature corresponding to the operating pressure of the HTF system. The vapour bubbles are then nucleated at the heated wall and grow to depart carrying the latent heat into the bulk fluid. The number and the size of the bubbles on the heated wall depend on various thermophysical properties of the fluid and the wall, including the wall surface roughness. This process becomes intensified with increased wall heat flux whilst the fluid temperature gradually shifts towards saturation temperature, hence boiling migrates the state of subcooled to saturated boiling [130, 131]. The high potency of heat dissipation in the boiling process is a very effective and useful mechanism for thermal applications in the commercial energy conversion industry.

4.5 Numerical Modelling

Boiling is a complex physical problem for numerical simulation as it involves coupled heat and mass transfer sub-processes through latent heat of fusion in liquid/vapour phase transitions. Additionally, bubble formation, coalescence and departure at nucleation sites cause random and vigorous momentum exchanges leading to intense fluctuations of flow turbulence. These complex physical processes in boiling make it a very challenging task for accurate prediction of thermal-fluid dynamic behaviour.

Recent research has reported several wall-boiling models and their possibility of integration into the Eulerian two-fluid modelling framework. This has dramatically enhanced the prospects of using computational fluid dynamics (CFD) solvers for efficient simulation possibilities of complex flow-boiling phenomena. Various empirical and mechanistic correlations have also been developed to represent the key physical process associated with boiling [2], such as drag, lift, turbulent dispersion and wall lubrication.

In the current numerical model, saturated flow boiling is considered within the HTF tube situated at the annular region of a cylindrical pelletised magnesium hydride reactor. A non-equilibrium boiling model (allowing simulation of superheated vapour) is selected to model the saturated boiling process. In a non-equilibrium model, the heat flux from the heated wall is subdivided into four components, namely the liquid phase-convective, quenching, evaporative heat fluxes, convective heat flux to the vapour phase.

4.6 Geometry

The geometry and dimensions of the MH tank with the incorporated HTF system are considered for both single-phase (sensible heat absorption) and multiphase flow (latent heat absorption) cases are depicted in Figure 4.1. The length of the MH powder bed and HTF flow domain is 2000 mm, the diameter of the HTF flow region is 10 mm, the inner and outer diameter of the MH bed is 10 mm and 50 mm, respectively. The pelletised magnesium hydride and water are considered as the MH powder bed and HTF, respectively. The thermophysical properties of MH and HTF, except the operating pressure of HTF, is considered the same for both single-phase and multiphase flow cases.

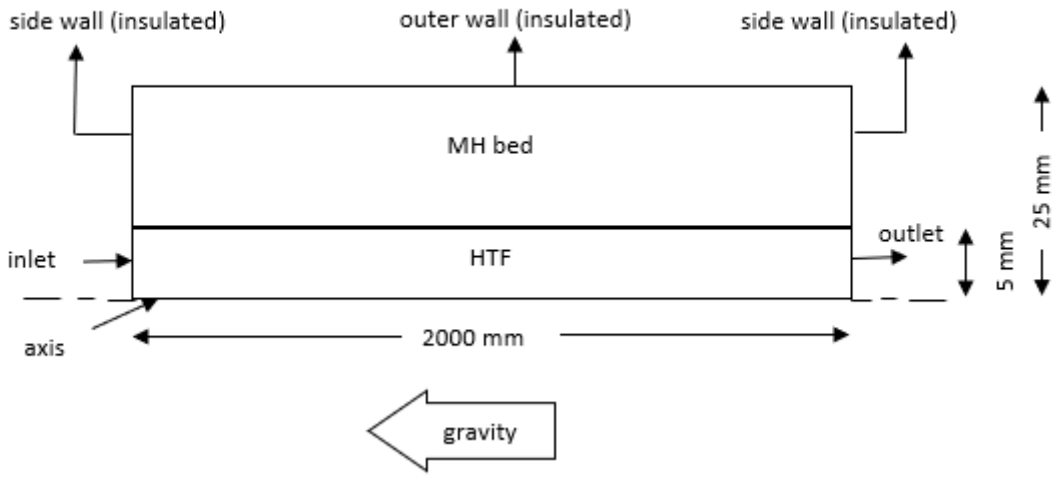

Figure 4.1: Schematic diagram of the MH reactor with HTF

4.7 Computational methodology

A boiling multiphase flow involves an exchange of mass, momentum, and heat between phases within the domain. The current study deploys Eulerian two-fluid formulation combined with the Rensselaer Polytechnic Institute (RPI) heat partitioning approach to simulate the convective boiling inside the heat transfer pipe. The Eulerian model solves conservation of mass, momentum and energy for each phase. The conservation of phasic volume fraction determines the distribution of water and vapour phases within the flow domain. The vapour bubbles formed during the boiling process are not considered a dispersed phase, and instead, a cumulative effect of bubble formation is considered by using empirical and/or analytical correlations. Both the single-phase and multiphase flow regions are modelled using the k-ω turbulence model, ideal for boiling heat flow modelling [132]. The governing equations associated with the single-phase and multiphase flows with transient heat source term associated with exothermic hydrogenation reaction are solved using ANSYS-FLUENT 2020 R1.

4.8 Governing equations and sub-closures

The following assumptions related to the MH bed have been made to simplify the simulation to a manageable level [17, 19, 21, 133]:

- Hydrogen is considered as an ideal gas within the operating conditions of the reactor.
- Local thermal equilibrium is valid between hydrogen and powder particles.

- Hydrogen flow inside the MH bed is neglected.
- The volumetric expansion MH due to hydrogenation is neglected.
- The thickness of the reactor wall of the MH tank is neglected.
- The MH tank is assumed to be perfectly insulated.
- Thermophysical properties of MH are constant.
- The numerical modelling of flow boiling adjacent to a porous region with a non-uniform heat source (MH bed) is extremely complex. Therefore, based on the above assumption, the porous MH bed is considered a solid region by accounting for the cumulative property values of hydrogen and metal in the MH region for both single-phase and multiphase flow cases.

4.8.1 The metal hydride bed

The energy equation for MH bed is given by:

$$(\rho C_P)_e \frac{\partial T_m}{\partial t} = \boldsymbol{\nabla}.(\lambda_e \boldsymbol{\nabla} T_m) + \dot{Q} \tag{4.1}$$

$\dot{Q}$ is the source term which is expressed as:

$$\dot{Q} = (1-\varepsilon)\rho_m wt \frac{dx}{dt}\frac{\Delta H}{M_g} \tag{4.2}$$

The rate of reaction $\left(\frac{dx}{dt}\right)$ of magnesium hydride was estimated by Chaise et al. [19], is used in the current numerical model.

$$\frac{dx}{dt} = \begin{cases} k_0 \dfrac{\alpha - 1}{2ln(1-\alpha)}\left(\dfrac{P}{P_{eq}} - 1\right)e^{-E_a/Rt}, & P > 2P_{eq} \\ k_0(1-\alpha)\left(\dfrac{P}{P_{eq}} - 1\right)e^{-E_a/Rt}, & P_{eq} < P < 2P_{eq} \end{cases} \tag{4.3}$$

where, E_a = 130 kJ/K mol H_2, $k_0 = 10^{10}$ s^{-1} [19].

with effective volumetric heat capacity

$$(\rho C_P)_e = (\varepsilon \rho C_P)_g + \left((1-\varepsilon)\rho C_P\right)_m \tag{4.4}$$

Effective thermal conductivity is expressed as:

$$\lambda_e = \varepsilon \lambda_g + (1-\varepsilon)\lambda_m \tag{4.5}$$

The equilibrium pressure is determined by the Van't Hoff equation:

$$\frac{P_{eq}}{P_{ref}} = exp^{\left(\frac{\Delta H}{RT_m} - \frac{\Delta S}{R}\right)} \tag{4.6}$$

where the reference pressure P_{ref}= 1 bar

4.8.2 Heat transfer fluid (Single-phase flow)

Continuity equation for the HTF is described as:

$$\boldsymbol{\nabla}.(\rho\vec{v})_{HTF} = 0 \tag{4.7}$$

The HTF flow is expressed by the Navier-Strokes equation:

$$\rho_{HTF}\left(\frac{\partial\vec{v}_{HTF}}{\partial t} + (\vec{v}_{HTF}.\boldsymbol{\nabla})\vec{v}_{HTF}\right) = (\mu_{HTF}(\boldsymbol{\nabla}^2 v_{HTF})) - \boldsymbol{\nabla}P_{HTF} + (\rho_{HTF}g) \tag{4.8}$$

The energy equation of the HTF is given by:

$$\frac{\partial(\rho C_P T)_{HTF}}{\partial t} + \boldsymbol{\nabla}.(\rho C_P\vec{v}T)_{HTF} = (\lambda\boldsymbol{\nabla}^2 T)_{HTF} \tag{4.9}$$

4.8.3 Heat transfer fluid (Multiphase flow)

The phasic volume of HTF is calculated from the volume fraction of each phase in HTF:

$$V_{(l\ or\ v)} = \int \alpha_{(l\ or\ v)} dV \tag{4.10}$$

$$\alpha_l + \alpha_v = 1 \tag{4.11}$$

where, the α_l and α_v denote the water and the vapour phase present in the fluid domain, respectively.

The continuity equation for each phase is calculated while accounting for the net rate of mass transfer (evaporation/condensation) across the phases.

$$\frac{\partial}{\partial t}(\alpha_l\rho_l) + \boldsymbol{\nabla}.(\alpha_l\rho_l\vec{v}_l) = \left(\dot{m}_{v,l} - \dot{m}_{l,v}\right) \tag{4.12}$$

where, $\vec{v}_l$ is the velocity of the water phase. $\dot{m}_{v,l}$ is interface mass transfer from the vapour phase to the water phase due to the condensation. $\dot{m}_{l,v}$ is the interface mass

exchange from the water phase to the vapour phase due to evaporation of the water near the heated wall (MH bed) during the boiling process.

$$\dot{m}_{v,l} = \frac{h_{RM} A_{int}}{h_{l,v}} (T_{sat} - T_l) \tag{4.13}$$

$$\dot{m}_{l,v} = \frac{q_E A_{w,l}}{h_{l,v} + c_{pl}(T_w - T_l)} \tag{4.14}$$

where, $A_{w,v}$ and $A_{w,l}$ are the area fraction of the heated wall occupied by the vapour phase and water phase, respectively. h_{RM} is the heat transfer coefficient at the liquid-side during the heat exchange between water-bubble interface.

$$A_{w,v} = \left[1 - A_{w,l}\right] = min\left(1, \frac{1}{4}\pi\xi N_w d_b^2\right) \tag{4.15}$$

where, ξ is the area influence coefficient given by the following expression:

$$\xi = 4.8e^{\frac{-Ja_{sub}}{80}} \tag{4.16}$$

where Jacob number

$$Ja_{sub} = \frac{\left(\rho C_p\right)_l \Delta T_{sub}}{\rho_v h_{l,v}} \tag{4.17}$$

N_w is the nucleation site density on the heated wall surface, which is expressed based on the Lemmert-Chawla correlation [134]:

$$N_w = 210^{1.805} (\Delta T_{sat})^{1.805} \tag{4.18}$$

A_{int} represent the interfacial area density which is defined as [135]:

$$A_{int} = \frac{6(1 - \alpha_v)\, min(\alpha_v, \alpha_{crit})}{d_b\left(1 - min(\alpha_v, \alpha_{crit})\right)} \tag{4.19}$$

where, $\alpha_{crit} = 0.25$.

The diameter of the vapour bubble (d_{bw}) detached from the heated surface is determined by Tolubinski-Kostanchuk empirical correlations expresses as [136]:

$$d_b = min\left(0.0014, 0.0006\, e^{-\Delta Tsub/45}\right) \tag{4.20}$$

The heat transfer coefficient at the liquid-side during the heat exchange between water-bubble interface (h_{RM}) in Equation (4.13) is calculated based on the well-established Ranz and Marshall empirical correlation as [137]:

$$h_{RM} = \left(2 + 0.6Re_b^{0.5}Pr_l^{0.33}\right)\frac{k_l}{d_b} \tag{4.21}$$

Conservation equation of momentum of each phase present in the Eulerian two-phase model is described as

$$\begin{aligned}\frac{\partial}{\partial t}(\alpha_i\rho_i\vec{v}_i) + \nabla.(\alpha_i\rho_i\vec{v}_i\vec{v}_i) \\ = -\alpha_i\nabla p + \nabla.\bar{\bar{\tau}}_i + \alpha_i\rho_i\vec{g} + \left[\dot{m}_{j,i}\vec{v}_{j,i} - \dot{m}_{i,j}\vec{v}_{i,j}\right] \\ + \vec{F}_{D,i} + \vec{F}_{L,i} + \vec{F}_{TD,i}\end{aligned} \tag{4.22}$$

where, α_i, ρ_i, $\vec{v}_i$, $\bar{\bar{\tau}}_i$ are the volume fraction, density, velocity and stress-strain tensor of the i^{th} phase, respectively. The stress-strain tensor of the i^{th} phase ($\bar{\bar{\tau}}_i$) is expressed as:

$$\bar{\bar{\tau}}_i = \alpha_i\mu_i\left(\nabla\vec{v}_i + \nabla\vec{v}_i^T\right) \tag{4.23}$$

Drag and lift coefficients are the key sub-closures for accurate prediction of momentum exchange between phases and need to be adopted to the specific multi-phase case.

The interface drag force ($\vec{F}_{D,i}$) in the Equation (4.22) is estimated as [138]:

$$F_{D,l} = -F_{D,v} = \frac{\alpha_l\alpha_v\rho_v f}{\eta_b}\left(\overrightarrow{v_v} - \overrightarrow{v_l}\right) \tag{4.24}$$

where, the term f is the drag function and η_b bubble relaxation time which are defined as:

$$f = \frac{C_D Re_m}{24} \tag{4.25}$$

$$\eta_b = \frac{\rho_v d_b^2}{18\mu_m} \tag{4.26}$$

where the term Re_m and μ_m are the Reynolds number between the liquid and vapour phases and the mixture phase viscosity, respectively.

$$Re_m = \frac{\rho_l d_b}{\mu_m}|\vec{v}_v - \vec{v}_l| \tag{4.27}$$

$$\mu_m = \frac{\mu_l}{1 - \alpha_v} \tag{4.28}$$

where, C_D is the drag coefficient based on Ishii et al. [138] is expressed as:

$$C_D = max\left(C_D^{vis}, C_D^{dis}\right) \tag{4.29}$$

where. C_D^{vis}, C_D^{dis} are the drag coefficients in the undistorted regime and the distorted regimes and defined as:

$$C_D^{vis} = \frac{24}{Re_m}(1 + 0.1Re_m^{0.75}) \tag{4.30}$$

$$C_D^{dis} = \frac{2d_b}{3\lambda_{RT}}\left(\frac{1 + 17.6\psi^{6/7}}{18.67\psi}\right) \tag{4.31}$$

where, λ_{RT} and ψ are the Rayleigh–Taylor instability wavelength and the void-function which are defined as:

$$\lambda_{RT} = \sqrt{\frac{\sigma}{g(\rho_l - \rho_v)}} \tag{4.32}$$

$$\psi = \frac{\mu_l}{\mu_m}\sqrt{1 - \alpha_v} \tag{4.33}$$

The term $F_{L,l}$ in the Equation (4.22) is lift force which is expressed as [139]:

$$F_{L,l} = -F_{L,v} = C_L\alpha_v\rho_l(\overrightarrow{v_v} - \overrightarrow{v_l}) \times (\nabla \times \overrightarrow{v_l}) \tag{4.34}$$

where, C_L is the coefficient of lift which is calculated based on the empirical model presented by Moraga et al. [139] as:

$$C_L = \begin{cases} 0.00767 & if\ \varphi \le 6 \times 10^3 \\ \left(0.12 - 0.2e^{\frac{-\varphi}{3.6\times10^5}}\right)e^{\frac{\varphi}{3\times10^7}} & if 6 \times 10^3 < \varphi < 1.9 \times 10^5 \\ -0.002 & if\ \varphi \ge 1.9 \times 10^5 \end{cases} \tag{4.35}$$

$$\varphi = Re_b Re_\nabla \tag{4.36}$$

Re_b and Re_∇ are the bubble and shear Reynolds numbers, respectively, which are calculated as:

$$Re_b = \frac{\rho_l d_b}{\mu_l} |\vec{v}_v - \vec{v}_l| \tag{4.37}$$

$$Re_\nabla = \frac{\rho_l d_b^2}{\mu_l} (\nabla . \vec{v}_l) \tag{4.38}$$

The turbulent dispersion $F_{TD,l}$ is calculated as:

$$F_{TD,l} = -F_{TD,v} = -C_{TD} \rho_l \kappa \nabla \alpha_v \tag{4.39}$$

where, C_{TD}=1 and $\sigma_{l,v}$ =0.9

The general transport equation for accounting the turbulence transport during the multiphase flow is defined as:

$$\frac{\partial}{\partial t}(\rho_m \phi) + \nabla . (\rho_m \vec{v}_m \phi) = \nabla . \left(\lambda_{\phi,eff,m} \nabla \phi\right) + S_{\phi,P} - S_{\phi,D} + \Omega_\phi \tag{4.40}$$

Based on the turbulence model (*k-e* or *k-ω* model) applied in the simulation, the term ϕ in the turbulence scalar term changes. $S_{\phi,P}$, $S_{\phi,D}$ *and* Ω_ϕ are the change in the kinetic energy in the flow domain due the production, dissipation, and source term, respectively. The turbulence scalar source term is for each turbulence model is calculated by using Troshko and Hassan *et al*. [140] model, which is as follows:

$$\Omega_k = \frac{\alpha_l \alpha_v \rho_v f}{\eta_b} |\vec{v}_v - \vec{v}_l|^2 \tag{4.41}$$

$$\Omega_\epsilon = \frac{0.45\, \Omega_k}{\tau_v} \tag{4.42}$$

$$\Omega_\omega = \frac{0.45\, \Omega_k}{\kappa \tau_v} \tag{4.43}$$

where, τ_v is the characteristic time for bubble induced turbulence, defined as:

$$\tau_v = \frac{2 C_{VM} d_b}{3 C_D |\vec{v}_v - \vec{v}_l|} \tag{4.44}$$

The conservation of energy equation in Eulerian multiphase flow is defined as:

$$\frac{\partial}{\partial t}(\alpha_i \rho_i h_i) + \nabla.(\alpha_i \rho_i \vec{v}_i h_i) = \alpha_i \frac{\partial p_i}{\partial t} + \bar{\bar{\tau}}_i : \nabla \vec{v}_i - \nabla.\vec{q}_i + \dot{Q}_{j.i} + \left[\dot{m}_{j,i} h_{j,i} - \dot{m}_{i,j} h_{i,j}\right] + \dot{Q}_{gen} \quad (4.45)$$

where $h_i \; and \; \vec{q}_i$ are the specific enthalpy and heat flux term for the i^{th} phase, respectively. $\dot{Q}_{j.i}$ is the energy transfer from the j^{th} (vapour) phase to the i^{th} (liquid) phase. $h_{i,j}$ is the latent heat of formation of phases, $\dot{Q}_{gen}$ is the source term in the i^{th} phase of the flow domain.

In the non-equilibrium model in Eulerian two-fluid framework (an extended version of RPI wall boiling model) the temperature of the vapour phase is not fixed at the saturation temperature, and heat transfer to the vapour phase is taken into account, and the total heat flux from the heated wall to the fluid is partitioned as follows [135, 136]:

$$q_T = \big(q_c + q_Q + q_E\big) f(\alpha_l) + \big(1 - f(\alpha_l)\big) q_v \quad (4.46)$$

where, q_c, q_Q and q_E are the liquid phase convective heat flux, quenching heat flux and evaporation heat flux, respectively. q_v is the convective heat flux of the vapour phase.

The three heat fluxes to the liquid are defined as,

The heat transfer from the heated wall to the liquid phase due to the convention is express as:

$$q_c = h_c\big(1 - A_{w,v}\big)(T_w - T_l) \quad (4.47)$$

where, h_c is the liquid phase heat transfer coefficient. The term $A_{w,v}$ already defined in Equation (4.14).

The heat transfer to the liquid phase, which comes into the vicinity of the heated wall when the vapour bubbles detached during the boiling process is defined by the quenching heat flux, which is expressed as :

$$q_Q = \frac{2k_l}{\sqrt{\pi \gamma_l T}}\,(T_w - T_l) \quad (4.48)$$

$$\gamma_l = \frac{k_l}{\rho_l C_{pl}} \quad (4.49)$$

The evaporative heat flux is defined as:

$$q_E = \left(\frac{\pi}{6}\right) d_{bw}^3 f_{bw} N_w \rho_v h_{l,v} \tag{4.50}$$

where, d_{bw}, f_{bw}, N_w and $h_{l,v}$ are the bubble departure diameter, bubble departure frequency, active nucleation site density and latent heat of vaporisation, respectively.

Frequency of bubble departure f_{bw} is expressed based on Cole [141] as:

$$f_{bw} = \sqrt{\frac{4g(\rho_l - \rho_v)}{3\rho_l d_{bw}}} \tag{4.51}$$

The literature-recommended Tolubinski-Kostanchuk empirical correlation is applied for the estimation of bubble departure diameter as [142]:

$$d_{bw} = min\left(0.0014, 0.0006e^{-\Delta Tsub/45}\right) \tag{4.52}$$

The heat flux partition to vapour phase q_v is expressed as:

$$q_v = h_v(T_w - T_v) \tag{4.53}$$

For the simulation, a uniform structured rectangular mesh with a maximum aspect ratio of 3.2 and skewness factor 1.31 x 10^{-10} is used for both the MH bed and HTF flow. The *k-ω* SST model, which has been found more suitable for multiphase in literature, has been employed to capture the turbulence in the flow [132, 143]. The transient governing equations described above are solved using the iterative techniques based on the finite volume method. A second-order discretisation scheme was used to solve all the equations except the energy equation. The Quadratic Upstream Interpolation for Convection Kinematics (QUICK) discretisation scheme has been used to solve the conservation of energy equation. The coupled scheme is used for pressure-velocity coupling. The multiphase flow convergence has been ensured by conditioning no residual (Fluent absolute criteria) less than 10^{-4} and monitoring mass imbalance between inlet and outlet flowrate throughout the hydrogenation process.

4.9 Initial and boundary conditions

The initial temperature of both the MH bed and HTF is uniform and equal to 580 K (T_0 = 580 K). The initial reacted fraction of the MH bed is assumed to be 0.01. A constant hydrogen pressure of 5 bar was applied throughout the hydrogenation process (P_0 = 5

bar). A relatively lower hydrogen pressure of 5 bar is intentionally chosen in the current model to avoid the numerical instability in the multiphase simulation caused by the high heat flux to the HTF during the initial phase of the reaction.

The adiabatic boundary condition is applied at the outer and the outer walls of the MH reactor and defined as:

$$\frac{\partial T_{(y_{top})}}{\partial y} = 0, \frac{\partial T_{(y_{bottom})}}{\partial y} = 0, \frac{\partial T_{(x_{outer\ wall})}}{\partial x} = 0 \tag{4.54}$$

The heat transfer between the MH bed and HTF is expressed as:

$$\lambda_e \frac{\partial T}{\partial r} = U(T_m - T_{HTF}) \tag{4.55}$$

The inlet boundary condition of HTF velocity and temperature are considered as T_{in} = 580 K and v_{in} = 0.01 m/s, respectively.

The flow velocity of HTF in this study is less than the recommended minimum (1 m/s) velocity in the heat exchanger tube. The velocity of HTF in a thermochemical reactor is selected based on the reactor's size and operating conditions. The low velocity (0.01 m/s) was chosen to highlight the effect of temperature rise of HTF on reactor performance and how this effect can be mitigated using multiphase flow.

The outer boundary condition for the HTF is taken as:

$$\nabla.(\lambda_{HTF} \nabla.T_{HTF}) = 0 \tag{4.56}$$

The operating pressure in the multiphase (boiling) HTF case is ~95 bar, which is chosen to make sure that the water entering at the inlet of HTF tube is in the saturated state corresponding to its inlet temperature of 580 K. The water in the single-phase case enters at a high operating pressure of 220 bar to prevent phase change during the sensible heat absorption of HTF. The thickness of the HTF tube and heat loss from the outer and sidewalls of the MH bed are neglected. The symmetric geometry, adaptable to vertical pipes, has been selected to use the axisymmetric simplification, which significantly reduces the computational effort.

The temperature-dependent thermophysical properties of the HTF are incorporated using piecewise and polynomial functions within the operating temperature range [144]. The

various constant thermophysical properties of the MH bed and HTF used in the computational model is described in Table 4.1.

Table 4.1: Thermo-physical properties used in the mathematical model [19]

Enthalpy of absorption (J/mol. H_2)	ΔH	−75000
Entropy of absorption (J/K/mol. H_2)	ΔS	−135.6
Density of MH (kg/m^3)	ρ_m	1800
Specific heat capacity of MH (J/kg.K)	C_{P_m}	1545
Porosity	ε	0.5
Gravimetric H_2 storage capacity (wt.%)	$wt.$	6
Hydrogen specific heat capacity (J/kg.K)	C_{P,H_2}	14000
Molecular weight of hydrogen (kg/mol)	M_{H_2}	0.002
Gas constant (J/mol K)	R	8.314
Dynamic Viscosity of Hydrogen (kg/m.s)	μ_{H_2}	8.9 x 10^{-6}
Thermal conductivity of Hydrogen (W/m.K)	λ_{H_2}	0.24
Thermal conductivity of magnesium hydride (W/m.K)	λ_m	4.2

4.10 Validation

The validation of the proposed MH reactor with multiphase HTF flow is essential to ensure physically meaningful results. Since there have not been any previous experimental measurements of a MH coupled with a boiling HTF available, the validation of the current MH reactor with boiling heat transfer is investigated for each system individually. Firstly, the validation of a magnesium hydride-based MH reactor is to be assessed for which a numerical validation of magnesium hydride reactor with helical heat exchanger could be considered [126]. This study represents the results of a 3D numerical modelling of a magnesium hydride reactor with a helical coil heat exchanger which correlated very well with experimental results.

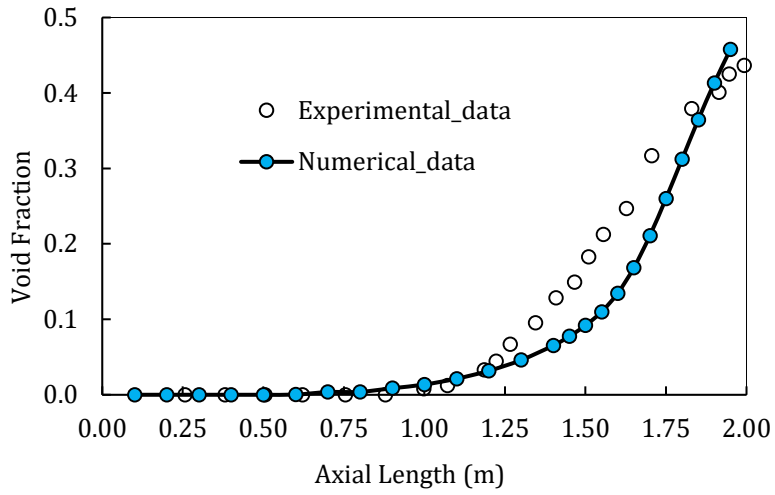

(a) Vapour volume fraction

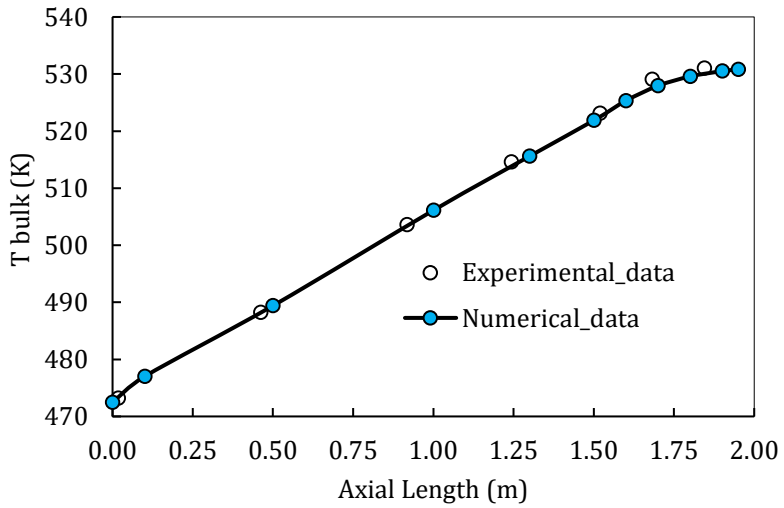

(b) Bulk fluid temperature

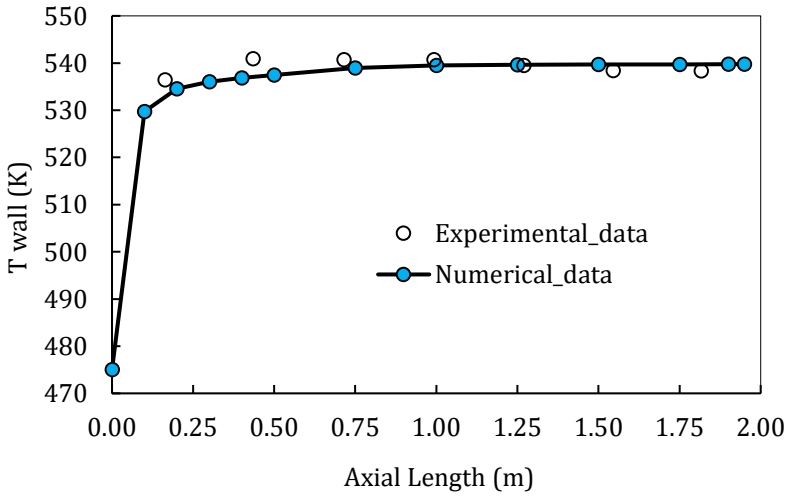

(c) Heated wall temperature

Figure 4.2: Comparison of boiling numerical results against experimental measurement [42]

Secondly, the explained model is deployed to simulate a convective boiling thermo-fluid field inside a vertical tube and compare the results against existing experimental measurements. For that, the experiment carried out by Bartolomei and Chanturiya [142], which has the same length, working fluid, and high operating pressure, as in the current simulations, was chosen. Moreover, the Bartolomei and Chanturiya [142] experiment is considered an experimental benchmark for boiling validation since it provides information such as fluid temperature, wall temperature and radially-averaged vapour fraction in a straight tube. The Bartolomei and Chanturiya [142] flow boiling experiment was conducted in a vertical tube with a heated length of 2000 mm and 15.4 mm in diameter. The water mass influx was 900 kg/m2s. The simulation for the validation was carried out using the k-ω SST turbulence model, which from previous studies suggested it as the most suitable for the internal flow boiling [132, 143]. Figures 4.2 (a-c) show the comparison between experimental and numerical data of bulk fluid temperature, heated wall temperature and radially averaged void fraction along the axial direction inside the vertical heated tube, respectively. Figures 4.2 (a-c) show the present numerical results correlate well with the experimental results of Bartolomei and Chanturiya [142] and hence it supports the validity of the numerical model.

4.11 Results and discussion

During the exothermic hydrogenation of the MH within the reactor, a large quantity of heat energy is released from the MH bed. The rate of exothermic reaction and the MH system performance can be improved by increasing the heat absorption rate from the MH bed to the HTF. The HTF collects the heat energy in a single-phase flow condition and undergoes a temperature increase. Due to the heat extraction from the MH bed, the temperature rise of the HTF eventually reduces the overall heat collection capacity of the HTF and thereby results in an overall performance reduction of the MH bed.

The drop in MH reactor performance can be overcome by introducing latent heat absorption in the HTF. The improvement of MH performance by multiphase flow over single-phase flow during the hydriding process is discussed in the following section.

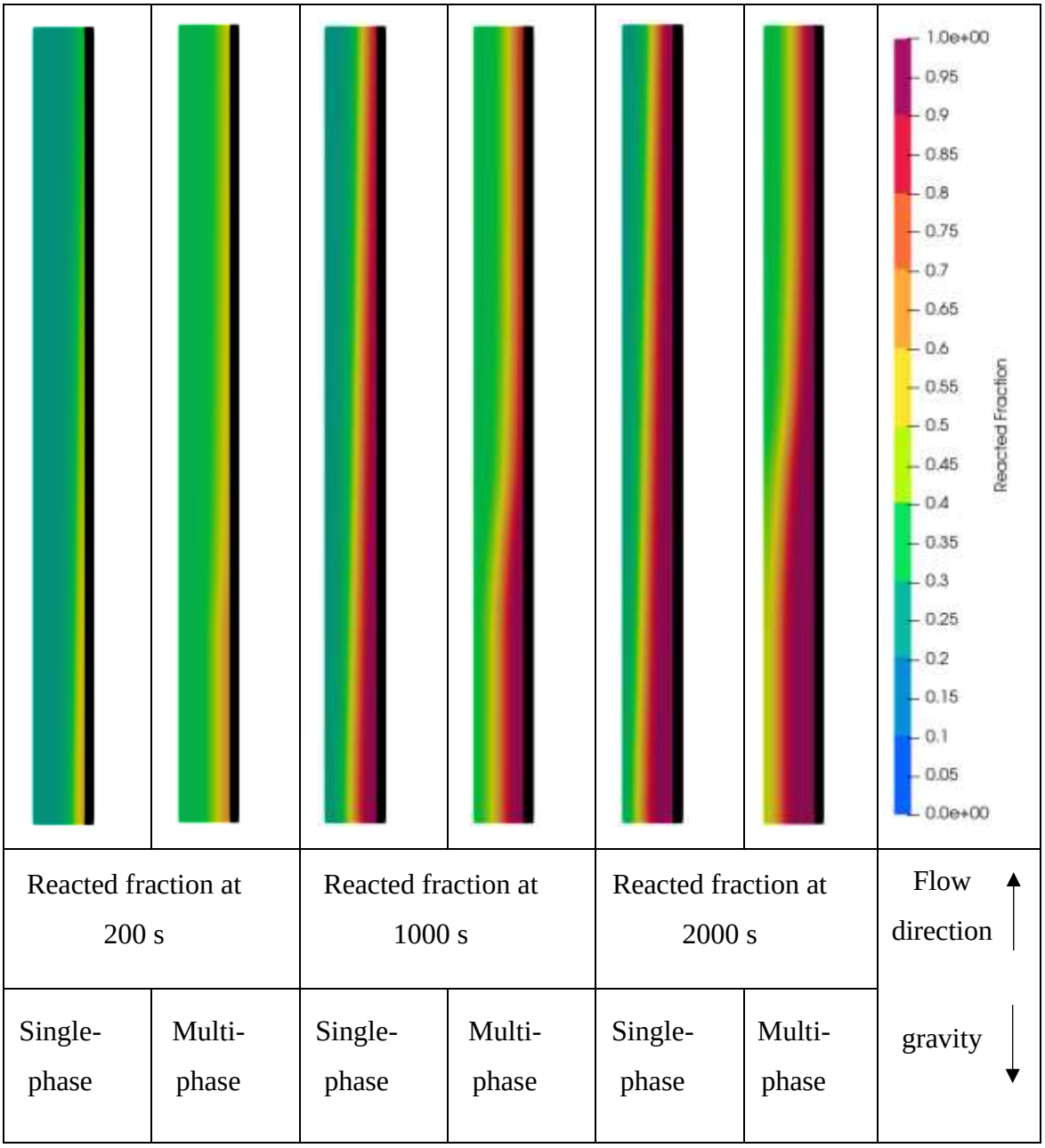

Figure 4.3: Comparison of reacted fraction in single-phase and multiphase flows at various time intervals (axisymmetric model)

Figure 4.3 shows the contours of the reacted fraction of MH in the bed during single-phase and multiphase heat absorption at 200 s, 1000 s and 2000 s. It is evident from Figure 4.3 that, the reacted fraction in the multiphase case is always higher than the corresponding single-phase flow case. This performance improvement is due to the higher temperature gradient between the HTF and MH when using multiphase rather than single-phase flow, which results in the faster hydrogenation process. For both the single-

phase and multiphase flow conditions, the maximum reacted fraction is always observed near the HTF inlet due to the larger temperature gradient between the MH and HTF.

Figure 4.4 compares the reacted fraction of single-phase and multiphase heat transfer cases over time. It is evident that during the hydrogenation process, the performance of the reactor is improved during multiphase flow over single-phase flow simulations. The rate of performance improvement in multiphase flow over single-phase flow is different at different reacted fractions of the MH bed. Owing to the large temperature gradient between the MH bed and HTF in the initial phase of the hydrogenation process, there is a spike in the reacted fraction in both single-phase and multiphase cases. In the initial 2 minutes of hydrogenation, the value of reacted fraction reaches ~0.33 in multiphase flow over ~0.23 in the single-phase flow. The boiling heat transfer enhancement contributes to the higher reacted fraction in multiphase flow over the single-phase flow.

The drop in performance due to the temperature rise of the HTF is significant in the single-phase flow case, whereas, it is eased in multiphase flow case. The uniform temperature condition is obtained as the HTF maintains at its saturation temperature during the boiling process. This improved state continues until the liquid film is fully evaporated (i.e. vapour volume fraction of 1) and boiling transits to dry-out regimes. Therefore, the multiphase flow reduces the negative impact of temperature rise of HTF to some degree. The percentage of improvement in the reacted fraction during the multiphase over the single-phase flow is ~85%, ~44%, ~32%, ~20% at reacted fraction of 0.3, 0.5, 0.8, 1, respectively. The results indicate a higher rate of performance enhancement in the initial phase of the reaction due to the significant rise in the temperature of the HTF in the single-phase flow compared to multiphase flow. The time taken to complete the hydrogenation process (reacted fraction = 1) in single-phase condition is ~154 minutes, whereas it is lowered to ~122 minutes in multiphase flow.

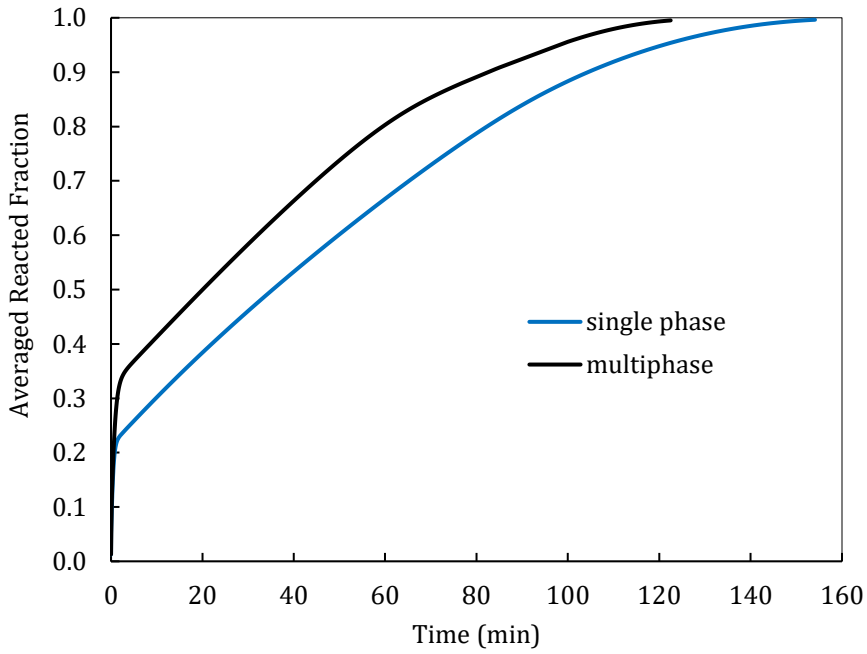

Figure 4.4: Comparison of overall reacted fraction of the MH reactor in single-phase and multiphase heat absorption

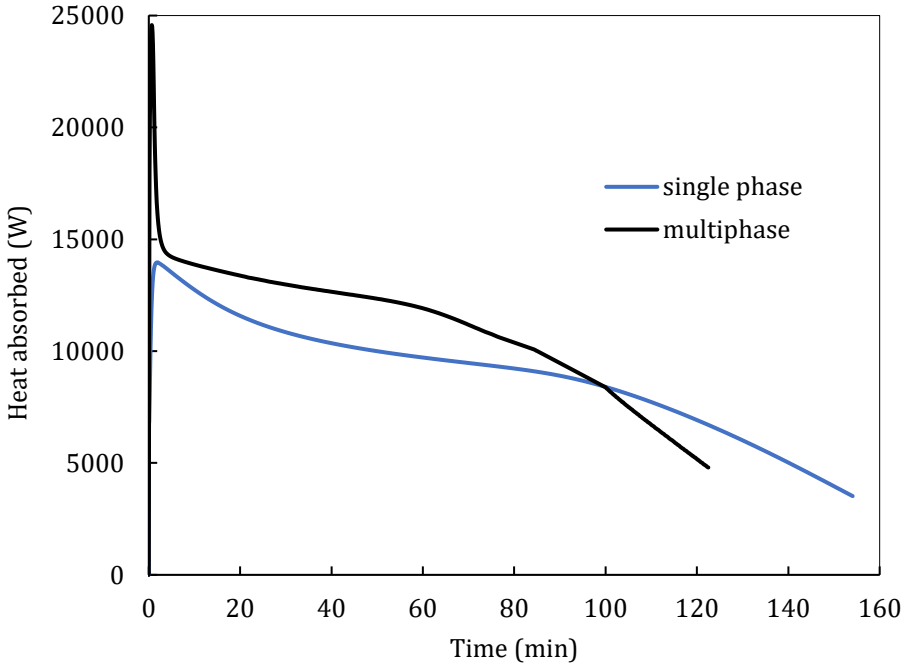

Figure 4.5: Comparison of heat absorbed by HTF in single-phase and multiphase cases

Figure 4.5 compares the overall heat collected from the MH bed by the HTF during the single-phase and multiphase flows. As expected from the reaction rate plot (Figure 4.4), the rate of heat collection with multiphase flow is higher than the single-phase flow. Similar to the reacted fraction plot trend, the rate of heat absorption in both cases is very high in the initial phase of the reaction. The maximum heat absorption rate is ~24 kW

and ~18 kW in the multiphase and single-phase flow, respectively. The rate of heat absorption in both single-phase and multiphase flow cases drops from the peak value as the reaction progresses due to reduced heat generation from the MH bed. During the majority of the reaction progression (until reaching 0.95 of the reacted fraction), the rate of heat absorption in multiphase flow is higher than the single-phase flow. Towards the end of the hydrogenation process (after the reacted fraction of ~0.95 is attained) in multiphase flow, the rate of heat absorption falls below the single-phase flow. The reduction in the heat collection rate is due to the reduced heat generation rate as the hydrogenation reaction of the MH nears completion.

Figure 4.6 represents the vapour profile at the wall between the MH domain and HT tube as the reaction progresses. The fluid enters the tube in the liquid state, where the vapour volume fraction remains zero at all times, and beyond this point, the vapour fraction increases in the streamwise direction. The distance over which the fluid phase converts from fully liquid ($\alpha_v = 0$) to dully vapour ($\alpha_v = 1$) depends on the heating intensity which, in this case, is supplied by the exothermic reaction in the MH medium. This transition is demonstrated, in Figure 4.6a, to happen over a shorter span of HTF tube at the earlier stage when the average reaction fraction is lower. This could be explained by more intense reaction rate and accordingly higher volumetric heat generation, which is mostly diffused toward the heat transfer tube and collected through the multi-phase convective mechanism.

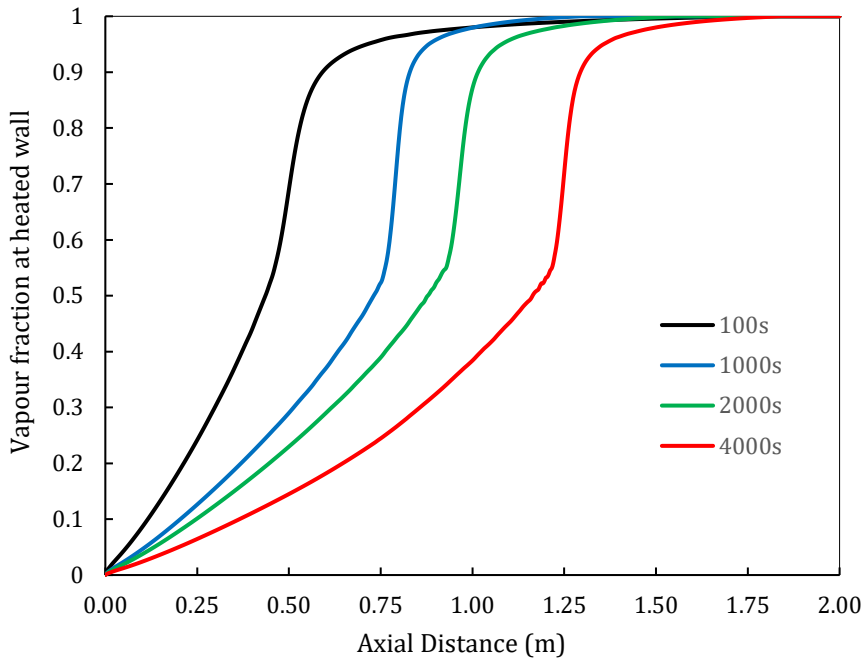

(a) Vapour fraction at the HTF tube

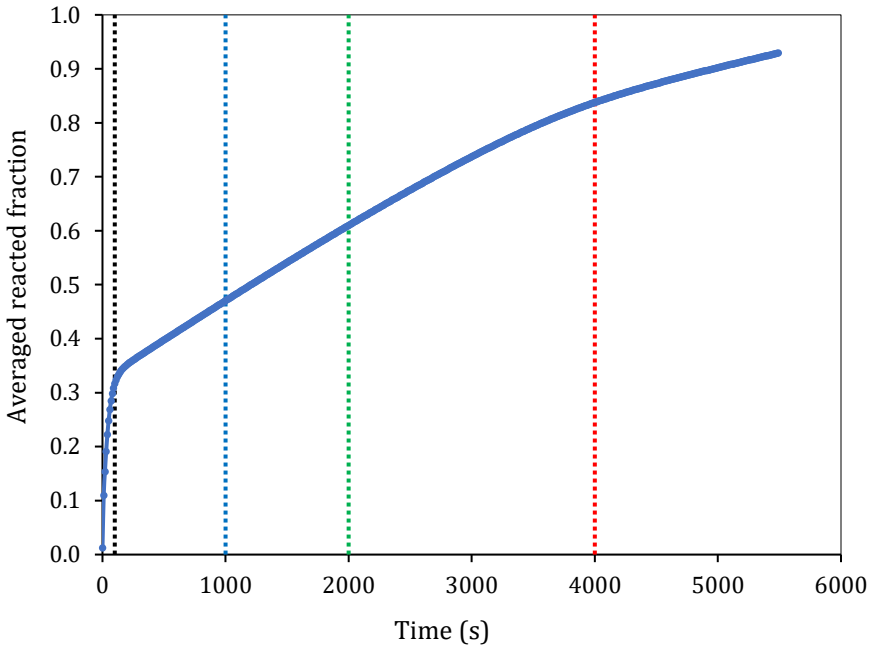

(b) Percentage of reaction

Figure 4.6: Vapour profile over the reaction period

The vapour volume fraction, which could be measured locally at the heated wall or averaged over the tube cross-section is an overall representation of the boiling process. Effectiveness of boiling heat transfer could be evaluated more comprehensively by interrogating the heat portioning components, explaining various physics involved in the

process. This unique privilege of RPI model also enables the development of an optimisation strategy to achieve more efficient convective conditions.

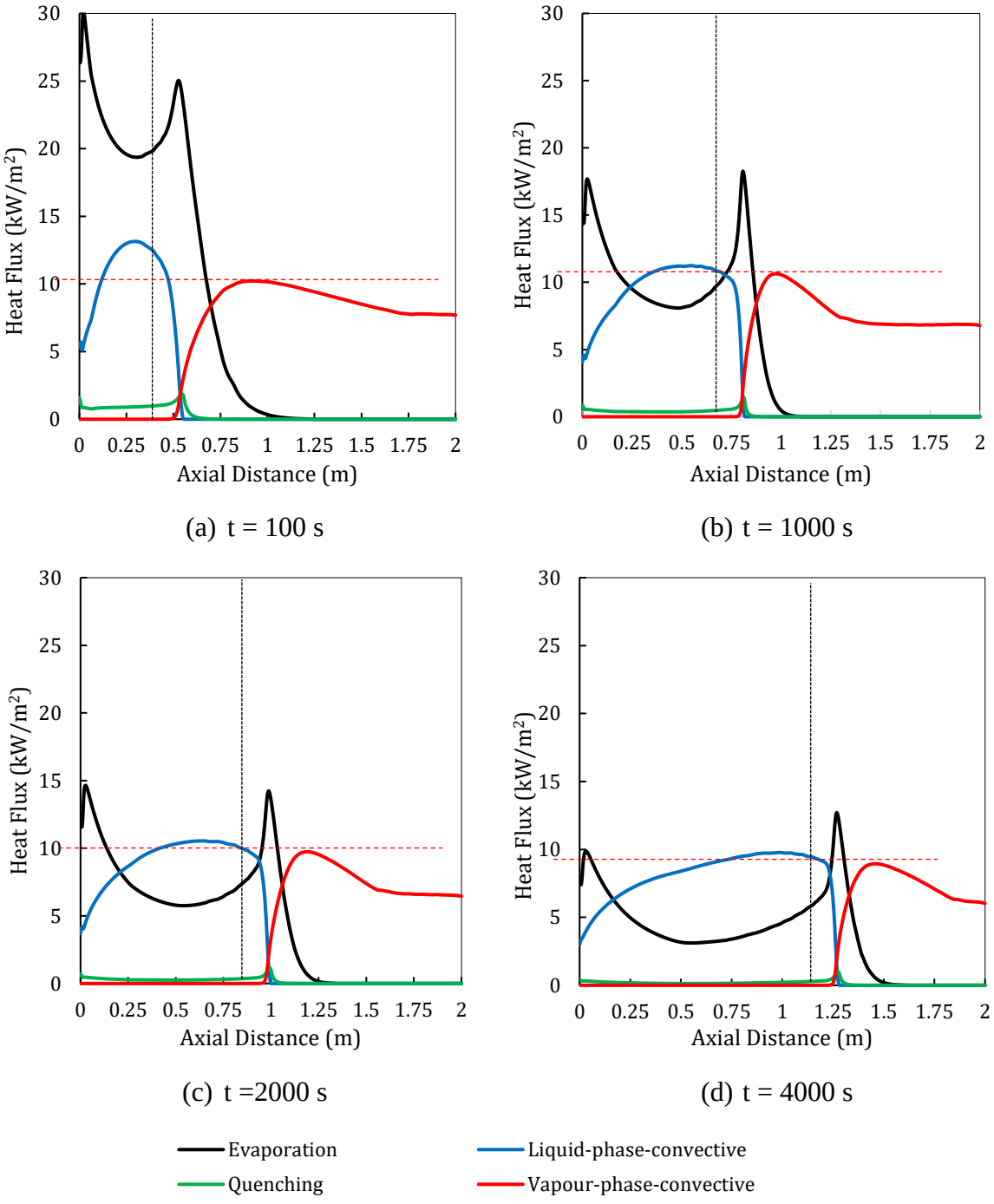

Figure 4.7: Evolution of heat partitions at the heated wall

Figure 4.7 demonstrates the key components of heat flux at the HT wall over four stages of the process. Evaporative and quenching components of heat flux are associated with the boiling process and are essentially averaged over the period of single bubble growth

and departure. The other two components represent the single-phase convective heat transfer of each phase (i.e. liquid and vapour). Prior to the second peak of evaporative heat flux (indicated by the black dash line), boiling (with evaporation being the dominant term) and liquid convection are the main mechanisms of heat transfer. Beyond this point, the heated wall is covered by a vapour jacket, and vapour convection is the only effective mechanism of heat removal. The intensity of vapour convection is generally lower than the evaporation and liquid convection. Such a reduction in heat removal capacity (when no further liquid is available on the heated surface) is referred to as dry-out in the boiling engineering context. These results indicate the potential for further optimisation of heat transfer by adjusting the subcooled temperature and flowrate of HT fluid, aiming for a more extended boiling domain and avoiding dry-out over the course of the reaction.

4.12 Other potential benefits of boiling HTF

Apart from the MH reactor's performance improvement during multiphase heat absorption, this method can also have some other practical benefits. The operating pressure of the HTF in a multiphase flow condition is always less than the single-phase flow. For example, in the current case, the operating pressure of the HTF in the multiphase case is ~95 bar, whereas in the single-phase it is ~220 bar. The higher operating pressure of HTF is required to prevent phase change in single-phase flow situations. Therefore, the lower working pressure of HTF will reduce the energy required to pressurise the HTF during operation. This will also enhance the safety of the MH system. Additionally, higher operating pressures have a higher associated cost due to the price of high-pressure tubing. Furthermore, a reduced operating pressure would allow HTF tubing with thinner wall thickness. This would reduce the thermal resistance across the HTF tube wall during the heat collection from the MH bed to HTF.

Furthermore, most of the current commercial thermal energy conversion devices use steam as the working fluid and utilises the phase change process of steam to generate the required energy output. So, utilising the same working fluid in the MH reactor would be more appealing to integrate the MH based TES into the CSP plants**.**

4.13 Conclusions

A comparative numerical investigation on a high-temperature thermochemical energy storage system based on magnesium hydride reactor's performance has been performed using water as a single-phase and multiphase heat transfer fluid (HTF). The transient boiling heat transfer process in the HTF flow has been simulated using the Eulerian two-fluid concept based on the CFD model. The boiling heat transfer has been numerically solved in the multiphase flow conditions. The comparative study of a single-phase and multiphase heat absorption method on a magnesium hydride reactor revealed that the heat absorbed by a multiphase flow from a MH reactor is much greater than by a single-phase flow. This results in a faster hydrogenation process and reduces the time duration for the reaction to complete. The reacted fraction in the multiphase flow over a single-phase flow is ~85%, ~44%, ~32%, ~20% at overall reacted fractions of 0.3, 0.5, 0.8, 1, respectively. In commercial application, this would mean that power can be generated more quickly and efficiently without as much lag.

The performance of the MH reactor can be further improved by optimising flow conditions of the multi-phase flow (like higher operating pressure and higher flow rates) to prevent the HTF from entering the dry-out region during the boiling process. This was not investigated in this study due to the numerical instability of the current model. A detailed study of the numerical standability of the mathematical model can be an investigation and can further result in more performance improvement of MH reactor in multiphase flows.

4.14 Declaration of competing interest

The authors declare that they have no known competing financial interests or personal relationships that could have appeared to influence the work reported in this paper.

4.15 Acknowledgements

This work was supported by resources provided by the Pawsey Supercomputing Centre with funding from the Australian Government and the Government of Western Australia. The authors acknowledge the financial support of the Australian Research Council (ARC) for ARC Linkage grant LP150100730. CEB and TDH acknowledge financial support from the Department of Industry Innovation and Science for the 2019 Global Innovation Linkage (GIL73589) grant.

CHAPTER 5: KINETIC INVESTIGATION AND NUMERICAL MODELLING OF $CaCO_3/Al_2O_3$ REACTOR FOR HIGH-TEMPERATURE THERMAL ENERGY STORAGE APPLICATION

5.1 Preface

This chapter is based on a manuscript submitted in the Journal of Energy Storage titled " ***Kinetic investigation and numerical modelling of $CaCO_3/Al_2O_3$ reactor for high-temperature thermal energy storage application*** *". This chapter contains the same text as the submitted manuscript, with minor formatting changes to enable thesis referencing.*

Kinetic investigation and numerical modelling of $CaCO_3/Al_2O_3$ reactor for high-temperature thermal energy storage application.

Arun Mathew [a,] , Nima Nadim [a], Tilak. T. Chandratilleke [a],

Mark Paskevicius [b], Terry D. Humphries [b], Craig E. Buckley [b]

[a] School of Civil and Mechanical Engineering, Curtin University

Curtin University, GPO Box U1987, Perth, WA 6845, Australia

[b] Department of Physics and Astronomy, Fuels and Energy Technology Institute

Curtin University, GPO Box U1987, Perth, WA 6845, Australia

5.2 Abstract

This study conducts kinetic analyses of the carbonation reaction of $CaCO_3$ doped with Al_2O_3 as well as parametric analyses of the performance of a thermochemical reactor, which can act as a thermal battery. Kinetic measurements were carried out using thermogravimetric analysis (TGA) at 1088, 1103 and 1118 K on a $CaCO_3/Al_2O_3$ sample that had been previously cycled over 500 times. The rapid reaction kinetics revealed that the Avrami nucleation growth model with exponent 3 fits well to explain the carbonation reaction. The numerical study considered a cylindrical reactor with a height and diameter of 100 mm. According to numerical analysis, at applied CO_2 pressure of 1 bar, increasing the thermal conductivity of the reactor bed from 1.33 to 5 W/m.K increases the rate of carbonation reaction by 73 %. When the applied CO_2 pressure is increased from 1 to 2 bar, the performance of the reactor bed with thermal conductivity of 1.33 W/m.K improves by 37%; however, when the applied CO_2 pressure is increased from 2 to 3 bar, the performance improves by only 16%. Additionally, when the boundary temperature of the reactor was lowered by 30 K, performance was enhanced by 34% at an applied CO_2 pressure of 1 bar. This study also examined the effect of using a graphite fin as a heat extraction system. The graphite fin allowed for rapid heat extraction and increased the carbonation reaction by 44% in the reactor bed with poor thermal conductivity (1.33 W/m.K) but had no effect in the reactor with modest thermal conductivity of (5 W/m.K) due to its ability to already transfer heat effectively to the reactor shell. The study demonstrates some of the limitations of poor thermal transport in a thermochemical battery.

Nomenclature	
Symbols	
C_P	specific heat capacity, J/kg.K
E_a	activation energy, J/mol
ΔH	molar enthalpy of reaction, J/mol
k	kinetic coefficient, 1/s
k_0	pre-exponential factor, 1/s
M	molar mass of CO_2, kg/mol
$\dot{Q}$	heat source, W/m^3
P	CO_2 pressure, Pa
ΔS	reaction entropy, J/ mol. K
R	universal gas constant, J/mol. K
T	temperature, K
λ	thermal conductivity, W/m.K
wt	maximum mass content of CO_2, %
t	time, s
ρ	density, kg/m^3
ε	porosity
dx/dt	carbonation velocity, 1/s
Subscript	
s	Solid reactant
eq	equilibrium
gas	gas, CO_2
e	effective
ref	reference
ini	initial
app	applied

5.3 Introduction

The transition of energy harnessing from non-renewable to renewable energy is inexorable in the coming decades due to the environmental impact and limited availability of fossil fuels. A great technological challenge surrounds the storage of energy that can be generated by the raft of emerging renewables to provide base-load power. A thermal energy storage (TES) system integrated with concentrated solar plants (CSP) can effectively counter the intermittency issue and provide a continuous energy supply. Compared to energy storage in batteries, the low cost and ease of integration of TES into large facilities are significant advantages of CSP over other technologies [145, 146]. According to the energy storage technique used, TES can be classified as sensible, latent, or thermochemical. Among the three options, thermochemical energy storage's superior characteristics such as higher energy density, the potential to be a low-cost system, and theoretically infinite energy storage duration have made it an appealing option [54, 147]. However, thermochemical energy storage remains a laboratory-scale endeavour due to the complexities associated with its more complicated reactions and overall system complexity [78, 148].

One of the critical requirements for developing a successful thermochemical energy storage system is the development of an appropriate energy storage material. A prospective storage material should possess the necessary chemical, thermophysical, and economic properties. Numerous materials have been considered in these aspects, including metal hydrides, hydroxides, oxides and carbonates [149]. Among the energy storage materials available, calcium carbonate ($CaCO_3$) is an attractive option due to its high energy storage density (1790 kJ/kg), abundant supply of limestone, low cost (10 €/ton), non-toxicity, and high operating temperature (near 1173 K) [150].

Using $CaCO_3$ as an energy storage material is reminiscent of its use in the calcium-looping (CaL) process for carbon sequestration [151]. The CaL technology utilises the carbonation reaction of calcium oxide (CaO) and the calcination reaction of $CaCO_3$ to store and reject carbon dioxide (CO_2), effectively concentrating it for carbon capture and sequestration purposes. The same concept can be applied to thermochemical energy storage due to the highly endothermic and exothermic reactions involved with CO_2 release and absorption, respectively. In TES applications, the CaO and $CaCO_3$ powders do not move between the calciner and carbonator reactors, but are usually contained in a

single packed bed reactor. In periods of excess energy generation, i.e. during the daytime, $CaCO_3$ absorbs thermal energy, undergoing an endothermic reaction, and the material decomposes into CaO and CO_2 gas. This process is called calcination. During hours of energy demand, the previously stored CO_2 gas is fed back into the reactor, where the solid CaO reacts with CO_2 and dissipates heat equal to the enthalpy of the carbonation reaction. This reversible exothermic reaction is called carbonation and can be expressed by [152]:

$$CaCO_3 \leftrightarrow CaO + CO_2 \ (\Delta H_{1173\,K} = 165.5\,kJ/mol) \quad (5.\ 1)$$

Utilising $CaCO_3$-based thermochemical reactions for heat storage has gained momentum in recent years, although Baker *et al.* [53] introduced the concept in the 1970s. Recently, process engineering studies of integrating $CaCO_3$ reactors for TES were conducted, and it was determined that the system possesses the necessary characteristics for commercial energy storage applications. Chacartegui *et al.* [46] investigated the application of CaL technology to TES in conjunction with a closed CO_2 power cycle for energy generation. When the pressure ratio of the carbonator to the turbine outlet was 3:1 and the recyclability of $CaCO_3$ was greater than 0.5 at 1148 K, the proposed model achieved a 45% of global plant efficiency. Additionally, this study discovered that the global plant efficiency could decline significantly when the reversibility of $CaCO_3$ falls below 0.2, of which it frequently does after multiple calcination/carbonation cycles [57].

Despite the favourable characteristics of $CaCO_3$, the decay in cyclic CO_2 storage capacity of the material has previously precluded it from becoming a suitable TES material. A TES system is expected to undergo thousands of absorption/desorption cycles without significant loss in energy storage capacity to become commercially viable. The storage capacity of pure $CaCO_3$ drops considerably after each carbonation/calcination reaction and reaches 25% of its initial capacity after 10 cycles and ~8% after 500 cycles [65, 153, 154]. The drop in multicyclic activity of $CaCO_3$ is due to sintering (pore-plugging) phenomena under the high temperatures used during thermochemical reactions [46, 150, 155-158].

Investigations have been conducted to improve the multicycle activity of the $CaCO_3$, with most of the focus being on reducing the sintering issue of CaO-based sorbents [150]. The addition of foreign elements (such as MgO, TiO_2, SiO_2, CuO, $CaZrO_3$) to $CaCO_3$ can cause chemical and morphological changes, limiting the particle size and controlling the

microstructure of $CaCO_3$ [65, 159-170]. Wu *et al.* [171] found that a nano-sized CaO/Al_2O_3 composite showed cyclic stability of 68.3% after 50 cycles when cycling between 923 K and 1073 K carbonation and calcination temperatures. The sintering issue was more recently addressed at 1173 K using $CaCO_3/Al_2O_3$ composites that formed $Ca_5Al_6O_{14}$, which acted as a barrier to sintering, but also an ion conductor to promote reaction kinetics [65]. The study revealed that $CaCO_3$ doped with 20 wt% Al_2O_3 maintained cyclic stability of ~70% over 500 cycles. This incomparable cyclic stability addresses many issues seen in CaL studies and demonstrates great potential for TES applications.

Numerous modelling studies of high-temperature thermochemical reactors, including those using metal hydrides, metal oxides, and metal hydroxides, are already underway. However, there have been just a few numerical studies of calcium carbonate reactors for thermochemical energy storage, most of which have been conducted recently [46, 47, 172]. The lack of research on $CaCO_3$ reactors for TES applications is mostly owing to the recyclability issue associated with $CaCO_3$ material, which is unfavourable for TES applications. Recent research, however, has shown techniques for greatly enhancing $CaCO_3$'s multicyclic activity. The recent experimental and numerical studies of the carbonation process for TES have mostly used fluidised bed and rotary kiln reactors [47, 173-175]. However, the operation and numerical investigations of the carbonation reaction in fluidised or rotary kiln $CaCO_3$ reactors differ from those in the packed bed reactor used in the current work.

In the current study, initially, the reaction kinetics of ball-milled $CaCO_3/Al_2O_3$ were measured. The calculation of the reaction kinetics of the material enables the numerical investigation of the $CaCO_3/Al_2O_3$ reactor under various operating conditions. Furthermore, the kinetic model is used to conduct the numerical investigation of the packed bed reactor for TES application. The operating temperature, thermal conductivity of the composite bed, CO_2 applied pressure, and bed porosity are all parametrically analysed. This investigation provides optimisation of operating conditions for large-scale TES operating conditions.

5.4 Experimental Analysis

$CaCO_3$ (≥99 %, Sigma-Aldrich) was ball milled with 20 wt% Al_2O_3 (≥ 98 %, Sigma-Aldrich) and CO_2 cycled 500 times at 1173 K according to a previous study by Møller *et al.* [65]. This material was used for reaction kinetic analysis. Thermogravimetric analysis (TGA) was performed on a Netzsch (STA 449 F3 Jupiter). The sample (13.74 mg) was measured using an Al_2O_3 crucible with a lid possessing a pin-hole to allow gas exchange. The sample was cycled under varying CO_2 partial pressures (0.5, 0.6, 0.7, 0.8 bar) under three isothermal conditions (1088, 1103 and 1118 K), see Figure 5.1.

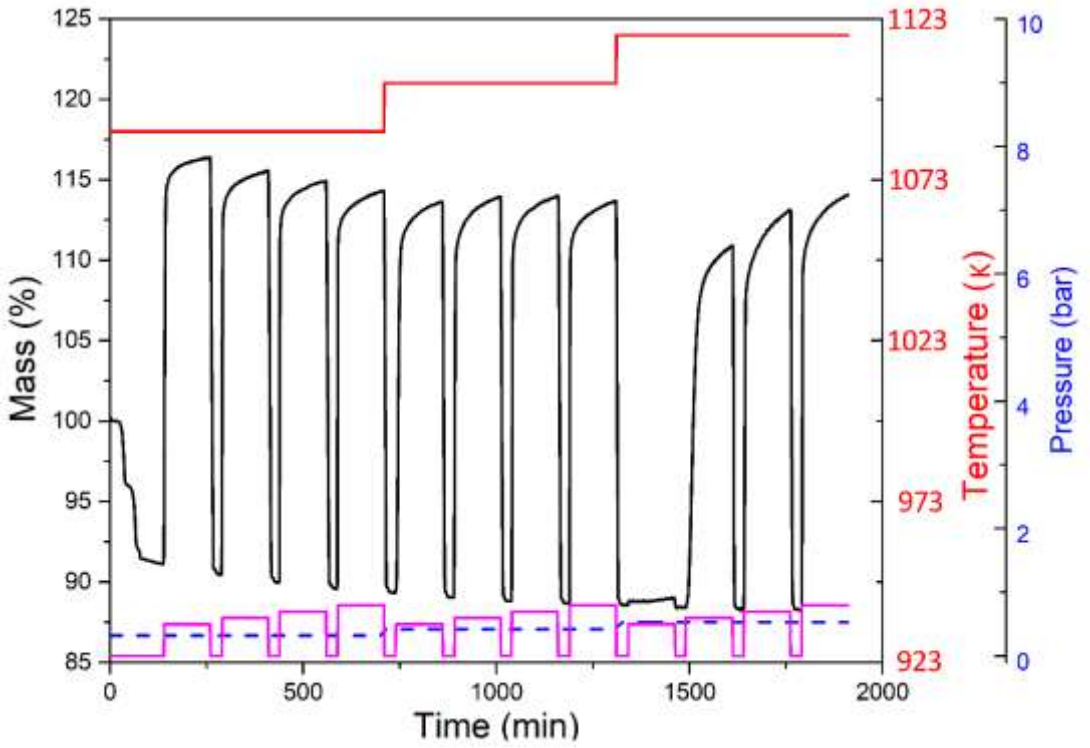

Figure 5.1: Reaction kinetics of $CaCO_3$ + 20 wt% Al_2O_3 data measured by TGA. Black line represents the mass loss/gain of the sample during absorption and desorption of CO_2. The red line is the isothermal temperature stages. The blue dashed line is the calculated equilibrium pressure of the material determined from thermodynamic measurements, and the purple line is the CO_2 partial pressure during the experiment. It is noted that no mass gain was measured at 1118 K and 0.5 bar CO_2 pressure as it is below the equilibrium gas pressure

The CO_2 partial pressures were attained by varying a mixture of Ar and CO_2 flow rates in the purge gas. In general, the program consisted of a ramp-up to 1088 K under a pure Ar flow to ensure decomposition of the starting material. An Ar/CO_2 mixture was then flowed over the sample under isothermal conditions for 1 h, after which a pure argon flow was again passed over the sample for 30 mins to decompose the sample again. The

material was then cycled under varying gas concentrations and temperatures using identical parameters. The temperature and sensitivity of the DSC were calibrated using In, Zn, Al, Ag and Au reference materials, resulting in a temperature accuracy of ± 0.2 K, while the balance has an accuracy of ± 20 μg.

5.5 Reaction Kinetics of $CaCO_3/Al_2O_3$

The reaction kinetics of pure $CaCO_3$ were previously studied for CO_2 storage applications, where the carbonation kinetics of CaO with CO_2 were found to be a two-stage process [176-178]. The initial phase of the carbonation is a rapid and kinetically controlled surface reaction, where the later stage is relatively sluggish and controlled by the diffusion of CO_2 through the as-formed $CaCO_3$ [151]. Inconsistencies in kinetic measurements have caused discrepancies in the kinetic models due to the type of material used (e.g. limestones, calcite crystals, precipitated $CaCO_3$), experimental apparatus used for absorption/desorption measurement (e.g. thermogravimetric analysers, flow reactors), the operating conditions for carbonation/calcination reaction (temperature, pressure of CO_2) and sample size of $CaCO_3$ [179-181]. As such, a new kinetic model is required for $CaCO_3/Al_2O_3$.

It was revealed from previous investigations that the $CaCO_3$/20% Al_2O_3 composite degrades to ≈ 70% of the initial CO_2 storage capacity over 500 cycles and maintains the same capacity for extended cycles [16]. As such, this cycled material was used to determine the typical kinetic parameters for $CaCO_3$ during absorption of CO_2 under typical reaction conditions. The absorption kinetics study was conducted at three different CO_2 pressures (0.6, 0.7, 0.8 bar) and temperatures (1088, 1103 and 1118 K). The TGA apparatus measurement shows that the carbonation reaction in $CaCO_3/Al_2O_3$ occurs rapidly (Figure 5.1). The majority of the reaction (90%) was completed in less than 60 seconds, which is much faster than the previously published result of pure $CaCO_3$ carbonation reaction kinetics for TES applications [182].

The reaction rate equation for any solid-gas reaction is generally expressed as follows [183]:

$$\frac{dx}{dt} = kf(x) \qquad (5.\ 2)$$

where x is the reacted fraction of the solid, k is the kinetic coefficient, which is a function of temperature (T) and pressure (P), and $f(x)$ is a function determining the mechanism of the reaction, and t is the reaction time.

Using the Arrhenius equation, the kinetic coefficient, k, can be expressed as [184]:

$$k = k_0 \, f(P) \, e^{-\frac{E_a}{RT}} \tag{5. 3}$$

where k_o is a pre-exponential factor, $f(P)$ is a pressure-dependent term, E_a is the activation energy, and R is the universal gas constant. After separating the variables and integrating Equation 2, the integral form of the reaction rate law, ($g(x)$), is obtained.

$$g(x) = \int \frac{dx}{f(x)} = kt \tag{5. 4}$$

Numerous kinetic functions representing chemical reactions, diffusion, nucleation, and nuclei growth mechanisms are currently available for gas-solid absorption systems [68, 185]. The volume of CO_2 absorption measured at three temperatures and pressures is fitted using known kinetic models. Model fitting approaches are based on fitting experimental data to a number of well-known solid-state reaction models listed in Table 2.3 in order to obtain the Ea and ko [68, 184, 186].

The integral forms ($g(x)$) of the various kinetic models listed in Table 2.3 are plotted against the time taken for the carbonation reaction at CO_2 pressure of 0.8 bar and temperature of 1118 K are depicted in Figure 5.2. According to the kinetic fitting analysis, the Avrami-nucleation and growth model ($(-\ln(1-x))^r$) with exponent r = 3, provides the best linear match for the majority of carbonation processes.

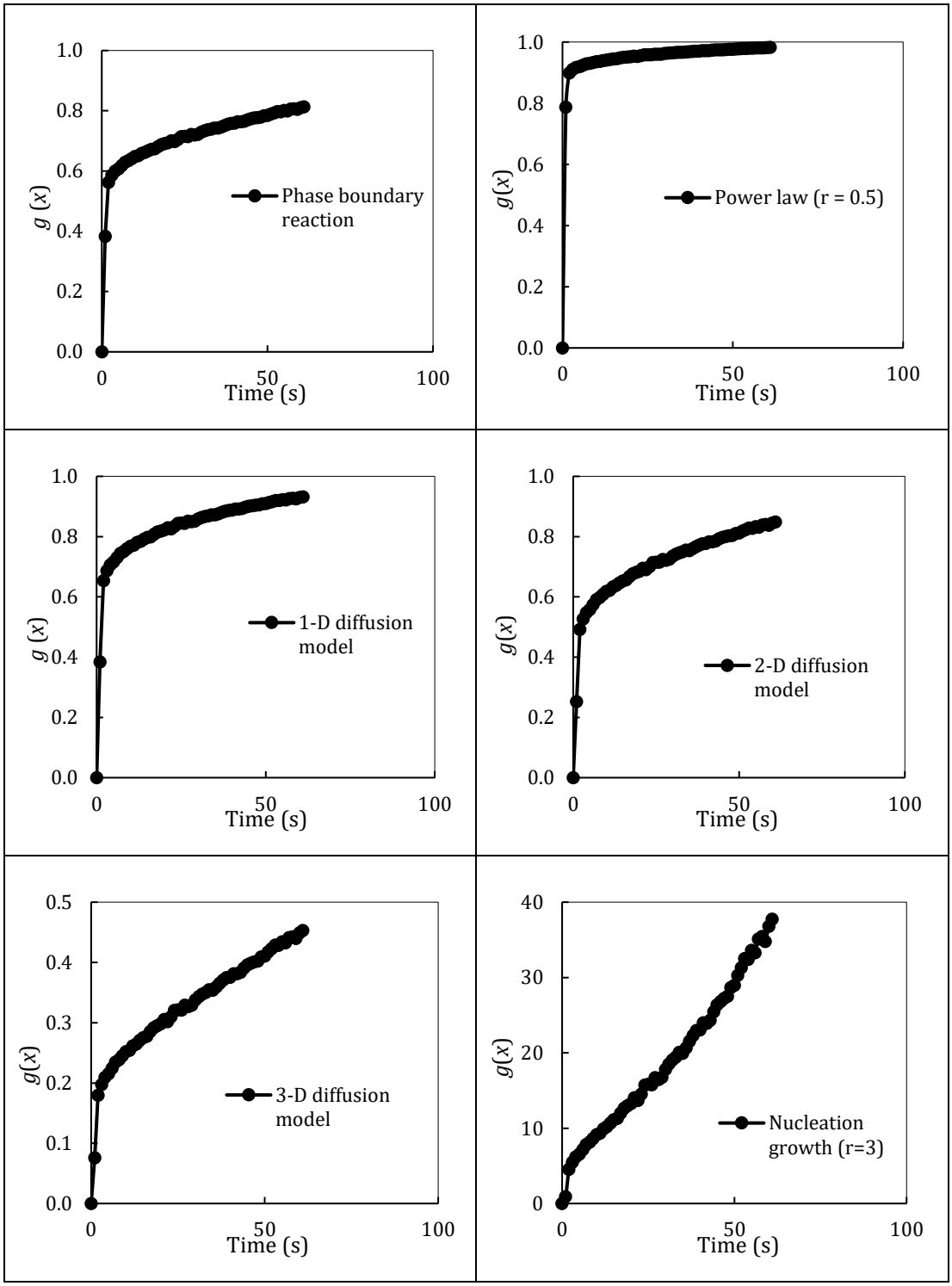

Figure 5.2: Comparison of the degree of fit of integral form of different kinetic models (g(x)) vs the time for carbonation (t) at 0.8 bar CO_2 pressure and temperature of 1118 K

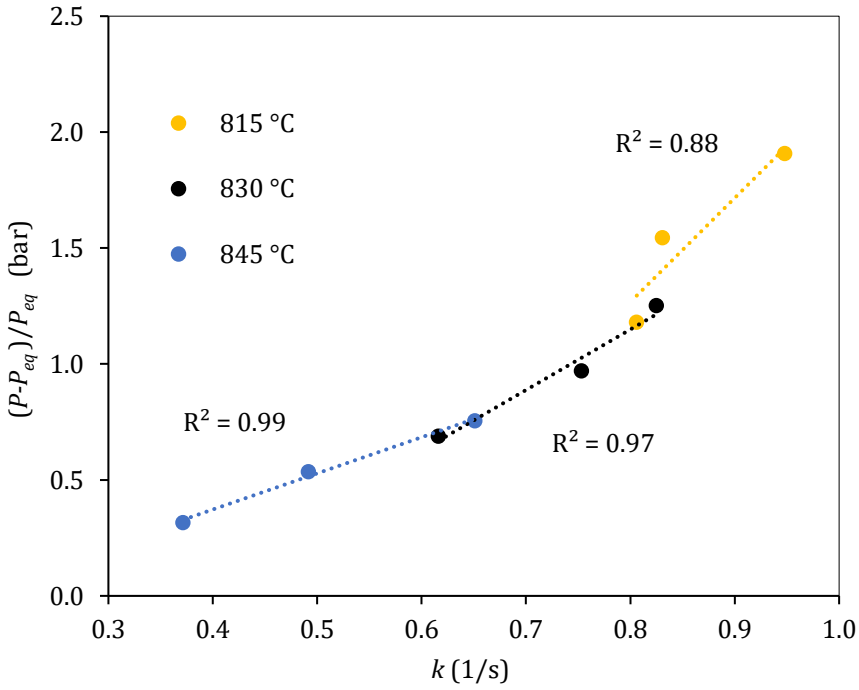

Figure 5.3: Plot of pressure function (($P–P_{eq}$)/P_{eq}) on the reaction vs kinetic coefficient (k) at CO_2 pressure of 0.8 bar and different temperatures

By substituting the pressure function, $f(P)$, into equation (3) yields

$$k = k_0 \left(\frac{P - Peq}{Peq}\right) e^{-\frac{E_a}{RT}} \qquad (5.5)$$

By taking the logarithm of both sides and combining with Equation 6, it can be rewritten in the form of a general equation of a line ($y = mx + c$) as

$$ln\,(k) - ln\left(\frac{P - Peq}{Peq}\right) = -\frac{Ea}{R}\frac{1}{T} + lnk_0 \qquad (5.6)$$

Plotting (ln (k) –ln ((P−P_{eq})/P_{eq})) against (1/T) for various CO_2 pressures gives a straight line with slope (–E_a/R) and intercept on the y axis (ln k_0). The value of activation energy (E_a) and pre-exponential factor (k_0) calculated from the slope and intercept values at CO_2 pressure of 0.6, 0.7 and 0.8 bar are listed in Table 5.1.

Table 5.1: Values of activation energy (Ea) and pre-exponential factor (k_0) of carbonation reaction at different pressures

Pressure (bar)	E_a (kJ/mol CO_2)	k_0 (s^{-1})
0.6	215.21	1.44×10^{10}
0.7	217.61	1.52×10^{10}
0.8	219.16	1.63×10^{10}

Similarly, substituting the integral form of the kinetic model, $g(x)$, and the pressure-dependent function, $f(P)$, into Equation 4 and rearranging the terms results in the reaction rate expression as

$$\frac{dx}{dt} = k_0 \frac{(1-x)}{3[-ln(1-x)]^2}\left(\frac{P-P_{eq}}{P_{eq}}\right) e^{\frac{-Ea}{RT}} \quad (5.\ 7)$$

5.6 Numerical Analysis

5.6.1 Physical model of the reactor

The physical model of the $CaCO_3$ reactor considered in the present work is shown in Figure 5.4. A cylindrical reactor with a length and diameter of 100 mm is considered for parametric investigations. It is assumed that the bottom and top faces of the cylinder are perfectly insulated. A constant temperature boundary condition is assumed at the outer wall of the cylinder. It is analogous to a rector, with the heat transfer fluid flowing through the outer wall of the cylinder at a constant temperature. This could be accomplished by using either a high heat transfer fluid flow rate or boiling heat transfer fluid flow, the latter of which was numerically explored in our previous study [187].

The following assumptions are made to simplify the simulations:

- CO_2 is considered as an ideal gas;
- Local thermal equilibrium is valid between CO_2 and powder particles;
- Thermophysical properties of reactor bed are constant and homogenous;
- CO_2 flow is neglected;
- The volumetric expansion of the reactor bed during carbonation is neglected.

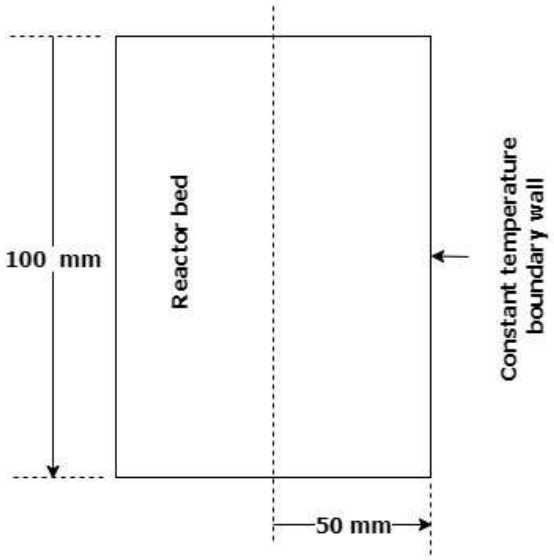

Figure 5.4: Schematic diagram of the reactor bed for numerical modelling

5.6.2 Governing Equations

The energy equation for $CaCO_3$ bed is given by [2]:

$$(\rho C_P)_e \frac{\partial T_m}{\partial t} = \nabla.(\lambda_e \nabla T_s) + \dot{Q} \quad (5.\ 8)$$

where ρ is the density, C_p is specific heat, T is the temperature, t is time, λ is the thermal conductivity and $\dot{Q}$ is the heat source term which is expressed as:

$$\dot{Q} = (1-\varepsilon)\rho_s wt \frac{dx}{dt}\frac{\Delta H}{M} \quad (5.\ 9)$$

where ε is the porosity of the bed, wt is the maximum mass content of CO_2, dx/dt is the reaction rate, ΔH is the enthalpy of reaction, and M is the molar mass of CO_2.

The effective volumetric heat capacity is expressed as:

$$(\rho C_P)_e = (\varepsilon \rho C_P)_{gas} + \left((1-\varepsilon)\rho C_P\right)_s \quad (5.\ 10)$$

The subscript, gas, represents the gas phase, while the subscript, s, denotes the solid phase.

The effective thermal conductivity is expressed as:

$$\lambda_e = \varepsilon \lambda_g + (1-\varepsilon)\lambda_s \quad (5.\ 11)$$

Table 5.2: Thermo-physical properties used in the numerical model [65, 106, 188]

Enthalpy of absorption (J/mol. CO_2)	ΔH	-16550
Entropy of absorption (J/K/mol. CO_2)	ΔS	-143
Density of $CaCO_3$ bed (kg/m^3)	ρ_{CaCO_3}	1850
Density of the Al_2O_3	$\rho_{Al_2O_3}$	3800
Density of the reactor bed (80% $CaCO_3$/ 20% Al_2O_3)	ρ_s	2240
Specific heat capacity of $CaCO_3$ (J/kg.K)	C_{CaCO_3}	910
Specific heat capacity of Al_2O_3 (J/kg.K)	$C_{Al_2O_3}$	775
Specific heat of the reactor bed (80% $CaCO_3$/20% Al_2O_3)	C_{P_s}	883
Porosity	ε	0.66
Gravimetric CO_2 storage capacity (wt%)	wt	25
Specific heat capacity of CO_2 (J/kg.K)	C_P	1257
Molecular weight of CO_2 (kg/mol)	M	0.044
Gas constant (J/mol K)	R	8.314
Thermal conductivity of $CaCO_3$ bed (W/m.K)	λ_m	1.33

5.6.3 Solution procedure

The CFD modelling of the $CaCO_3$ reactor was performed using a commercial finite volume software package, ANSYS Version 2020 R1. The computational domain was generated using the Design Modeler and ANSYS Meshing used for mesh generation. The user-defined functions (UDF) have been incorporated into the CFD model to actively estimate the reaction rate of the carbonation process and equilibrium pressure. The energy equation was solved using the QUICK differencing scheme. Previously, the computational modelling of a high-temperature thermochemical reactor for TES application was validated. The kinetic study and numerical modelling of a thermochemical reactor with helical coil heat exchanger and convective heat loss conditions were accurately simulated, and the results were found to be in good agreement with the experimental data [126].

5.7 Results

5.7.1 Effect of CO_2 supply pressure

The influence of applied CO_2 pressure on the carbonation reaction in the reactor bed was investigated by evaluating the averaged carbonation reacted fraction, averaged bed temperature, and rate of heat absorption from the reactor. The CO_2 supply pressure of 1, 2, and 3 bar were considered for the study. A constant temperature of 1073 K was maintained at the outer wall of the reactor. The initial reacted fraction and temperature of the bed were considered as 0.01 and 1073 K, respectively.

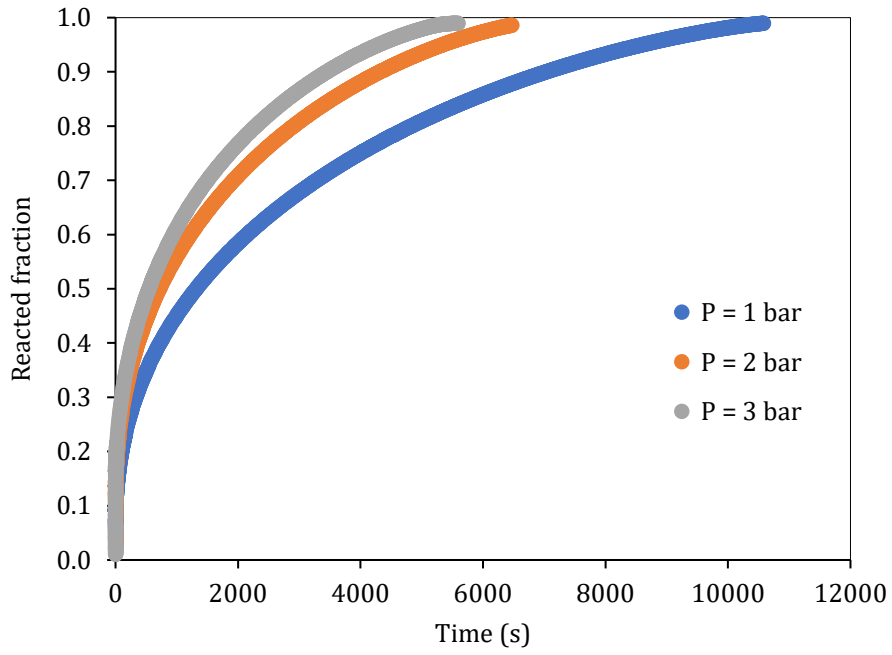

Figure 5.5: Effect of carbon dioxide supply pressure on average reacted fraction of $CaCO_3$ during carbonation

Figure 5.5 depicts the effect of supply pressure on the averaged reacted fraction. An increase in applied pressure of CO_2 accelerates the carbonation reactions in the reactor bed. The time required to complete the reaction is ~10580, ~6680, and ~5590 s when the applied CO_2 pressure of 1, 2, and 3 bar, respectively. It is discovered that increasing the applied pressure from 1 bar to 2 bar results in a 37% faster reaction but increasing the pressure from 2 bar to 3 bar results in only a 16% improvement. This variation in the performance improvement of the reactor with pressure is due to the change in kinetic parameters as the pressure increases.

Figure 5.6 shows the effect of applied CO_2 pressure on the temperature of the reactor bed. The bed temperature rapidly increases in the initial phase of the reaction in all three pressure scenarios. The sudden temperature rise is due to a large pressure gradient between applied pressure and equilibrium pressure. As a result, the maximum temperature of the bed reaches ~1229 K in the 3 bar scenario, while it reaches only ~1159 K under 1 bar CO_2 pressure. As the reaction progresses, the bed temperature decreases due to heat exchange to the outer wall of the reactor.

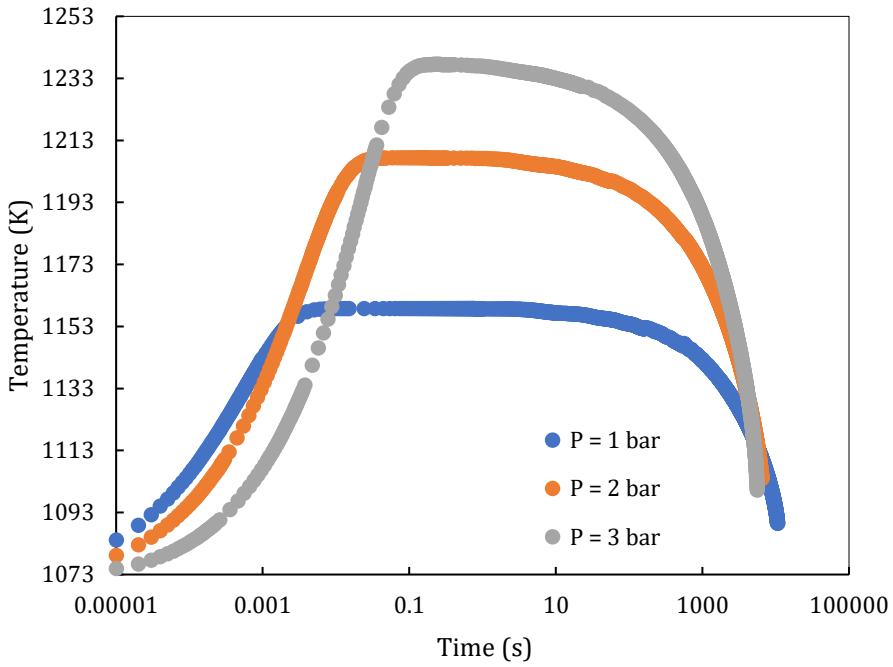

Figure 5.6: Effect of carbon dioxide supply pressure on temperature of the reactor bed with thermal conductivity of 1.33 W/m.K

Figure 5.7 shows the variation in the heat transfer rate under varied pressures. Due to the large temperature gradient between the reactor bed and outer wall, the heat transfer rate is much higher during the initial phase of the reaction. Therefore, the maximum heat transfer rate under 3 bar CO_2 pressure exceeds 4500 W/m^2, but it is less than 2500 W/m^2 under 1 bar CO_2 in the initial reaction phase. However, as the reaction progresses, there is a significant drop in the heat transfer rate due to a drop in the temperature of the reactor bed. The heat transfer rate falls below 200 W/m^2 in all cases within 500 s of reaction.

The abrupt decrease in the heat transfer rate is caused by the characteristics of the reaction that occurs in the reactor. During the initial phase of the reaction, the reactor bed closest to the exterior wall has a faster reaction rate due to increased heat transfer to the outer wall, causing the reaction to complete more quickly. However, a large portion of the

powder bed in the centre of the reactor remains unreacted. As time progresses, the fully finished reacted bed region adjacent to the reactor's outer wall restricts heat transfer from the reactor's core to the outer wall.

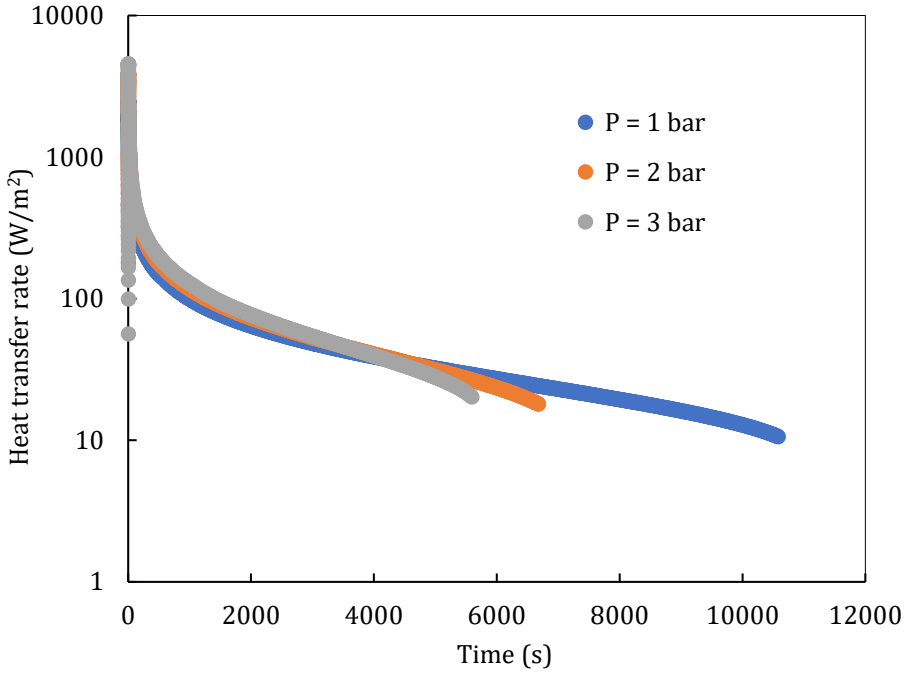

Figure 5.7: Effect of carbon dioxide supply pressure on heat transfer rate from the reactor bed

5.7.2 Effect of thermal conductivity

A parametric investigation of thermal conductivity of the reactor bed was numerically studied using the values of 1.33, 3, and 5 W/m.K. The boundary wall temperature and initial temperature were maintained at 1073 K. A constant pressure of 1 bar CO_2 was applied for this study. Figure 5.8 shows that an increase in thermal conductivity has a profound effect on reactor performance. An increase in thermal conductivity of the bed from 1.33 to 5 W/m.K reduces the overall time to complete the carbonation reaction from ~10580 to ~2865 s. The improved performance due to the thermal conductivity enhancement is marginal until the reacted fraction reaches 0.2. However, as the reaction progresses, the effect propagates. The enhanced reaction rate in the later stages of the reaction in the high thermal conductivity scenario is owing to the faster heat transfer across the fully reacted reactor bed adjacent to the outer wall.

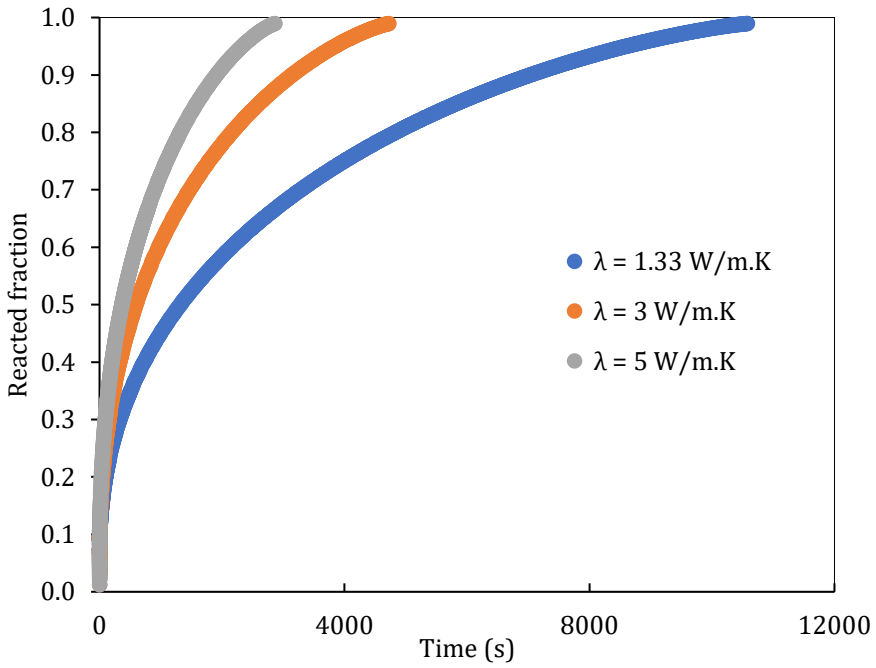

Figure 5.8: Effect of thermal conductivity of reactor bed on the reacted fraction at CO_2 pressure of 1 bar

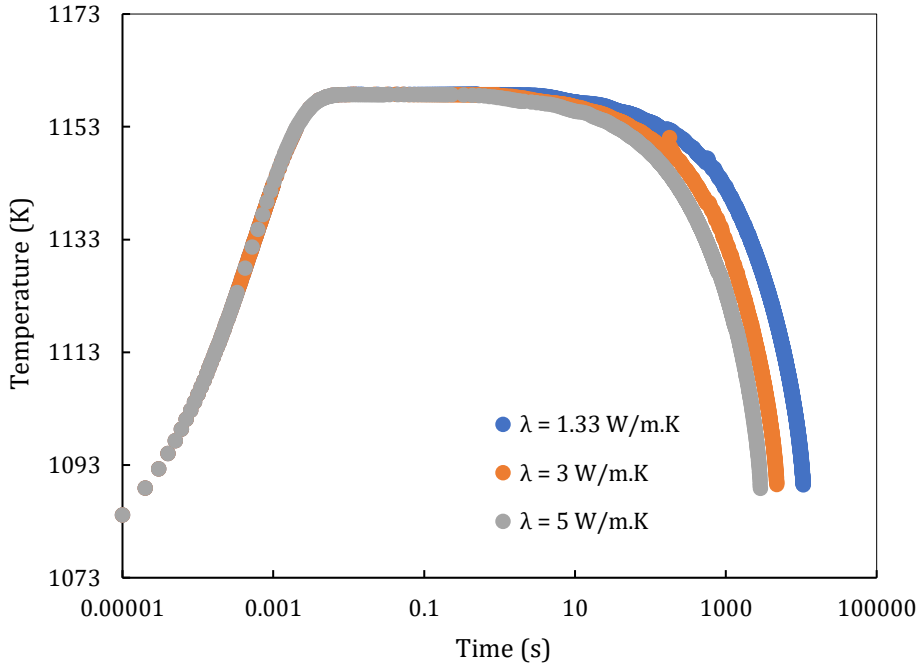

Figure 5.9: Effect of thermal conductivity of the bed on reactor temperature at CO_2 pressure of 1 bar

Figure 5.9 shows the averaged temperature of the reactor bed at various thermal conductivity values. It can be seen from the plot that the thermal conductivity augmentation has a negligible effect on the maximum temperature of the reactor bed.

The maximum temperature of the reactor bed reaches ~1158 K for all cases resulting in a similar performance of the reactor in the initial phase of the reaction. The bed with a higher thermal conductivity cools down faster as the reaction progresses due to more effective heat exchange to the outer wall of the reactor bed. As such, for a thermal conductivity of 5 W/m.K it takes 2865 s for the bed temperature to reach 1088 K, while it requires 10580 s for a thermal conductivity of 1.33 W/m.K.

The influence of thermal conductivity on the heat transfer rate is depicted in Figure 5.10. Unlike the average temperature profile of the reactor bed, the total heat transfer rate is much higher when thermal conductivity is increased. For example, the maximum heat transfer rate reaches ~9150 W/m^2 in the 5 W/m.K case, whereas it reaches ~2480 W/m^2 when thermal conductivity is 1.33 W/m.K. Furthermore, the elevated heat transfer rate is only visible for a few seconds before dropping below 660 W/m^2 in all scenarios within 100 seconds.

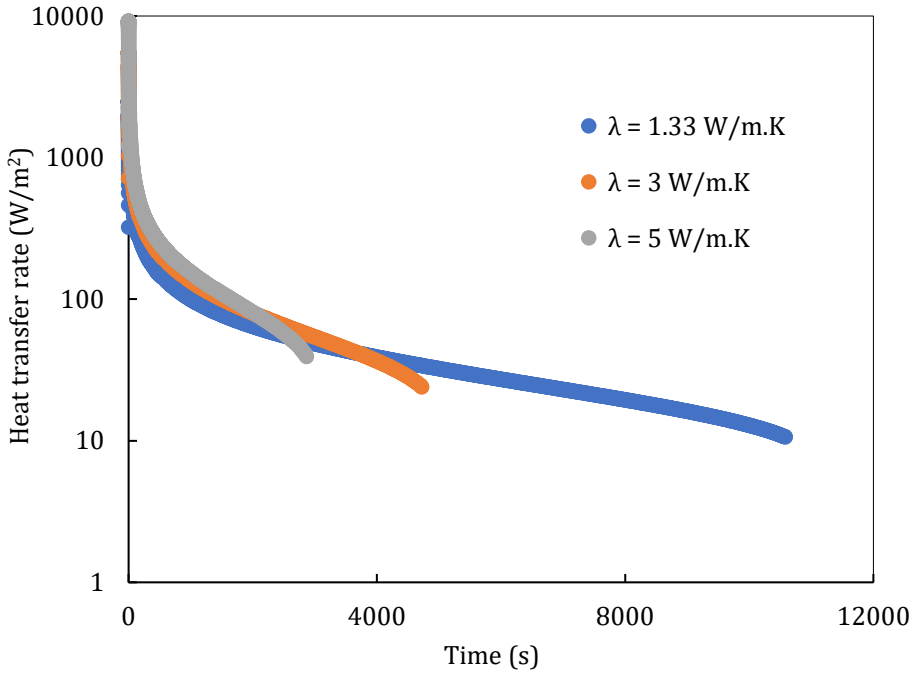

Figure 5.10: Effect of thermal conductivity of bed on heat transfer rate at CO_2 pressure of 1 bar

5.7.3 Boundary temperature

The influence of boundary temperature of the reactor bed was investigated by maintaining boundary temperatures of 1073, 1088, 1103 K under constant CO_2 pressure of 1 bar. The effect of the boundary wall temperature on the reactor performance is depicted in Figure 5.11. The rise in the boundary temperature increases the time required

to complete the carbonation reaction. This effect is minor until the reacted fraction reaches 0.3 but becomes more noticeable as the reaction process. The time taken to complete the reaction is ~10580, ~12590, ~16100 s, when the boundary temperatures are 1073, 1088, 1103 K, respectively. Therefore, a decrease in wall temperature by 30 K decreases the reaction completion time by ~34%. Increased heat transfer from the reactor bed results in a faster reaction at low-temperature boundary conditions. The higher heat transfer from the reactor bed contributes to a faster reaction in the low-temperature boundary cases. The temperature variation of the exterior wall of the reactor can be interpreted as the temperature of the heat transfer fluid flowing through the real-world application. When a single-phase heat transfer fluid flow is supplied to the reactor's outer wall, the results indicate how increasing the temperature of the heat transfer fluid as it passes through the reactor affects reactor performance.

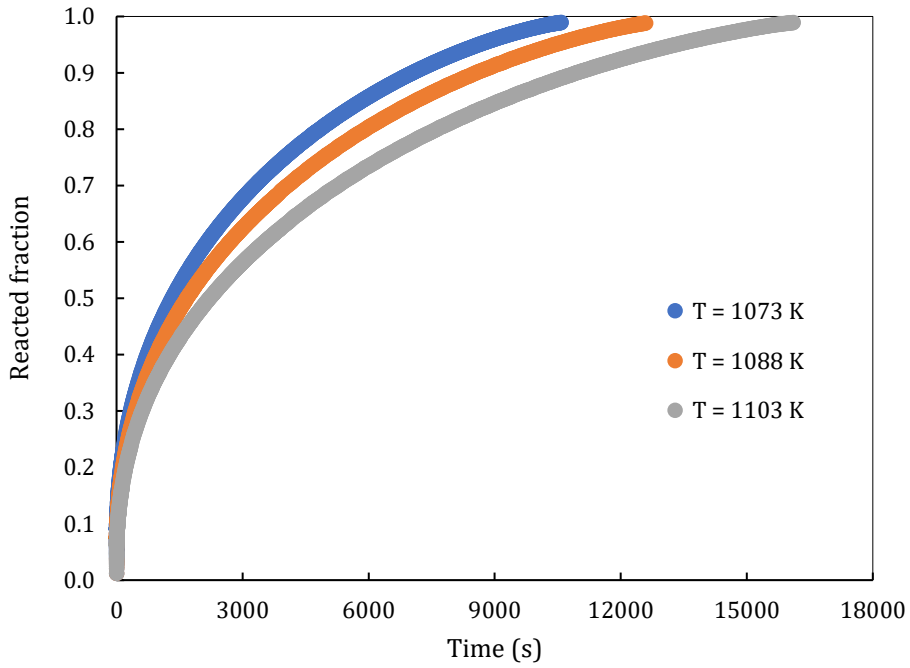

Figure 5.11: Effect of reactor's boundary temperature on the reacted fraction at CO_2 pressure of 1 bar

Figure 5.12 shows the temperature variation of the reacted fraction at different boundary wall temperatures. Similar to the previous parametric investigations in this study, the temperature of the bed rises rapidly in the initial few seconds. The study suggests that the boundary temperature does not effectively influence the maximum temperature of the bed, as for all cases the highest temperature of the bed reaches 1158 K within a few seconds of reaction initiation. Due to faster heat exchange to the outer wall of the reactor,

the temperature of the bed drops faster when the boundary wall is at a minimum (1073 K).

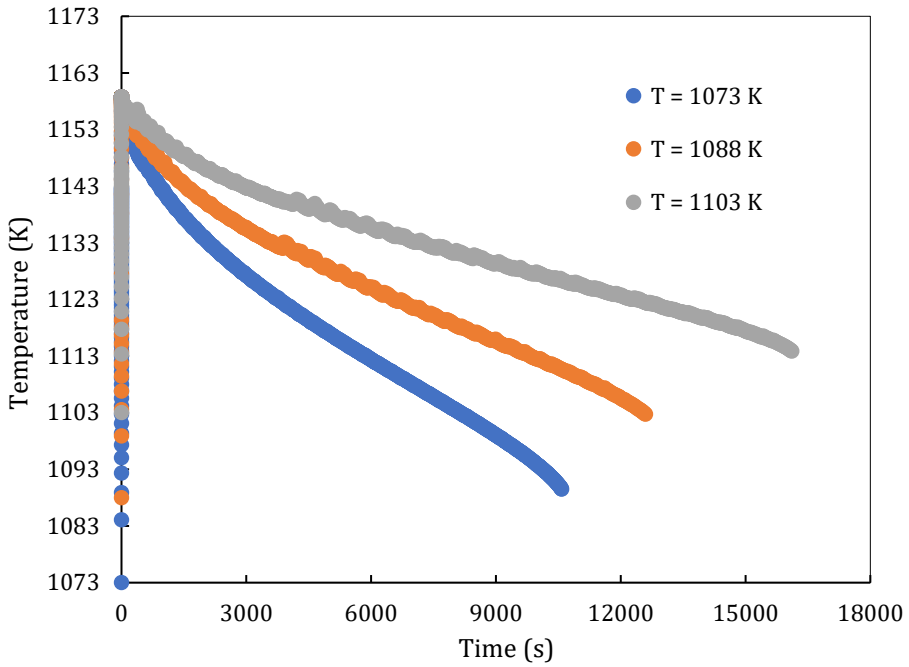

Figure 5.12: Effect of boundary temperature of the reactor temperature at CO_2 pressure of 1 bar

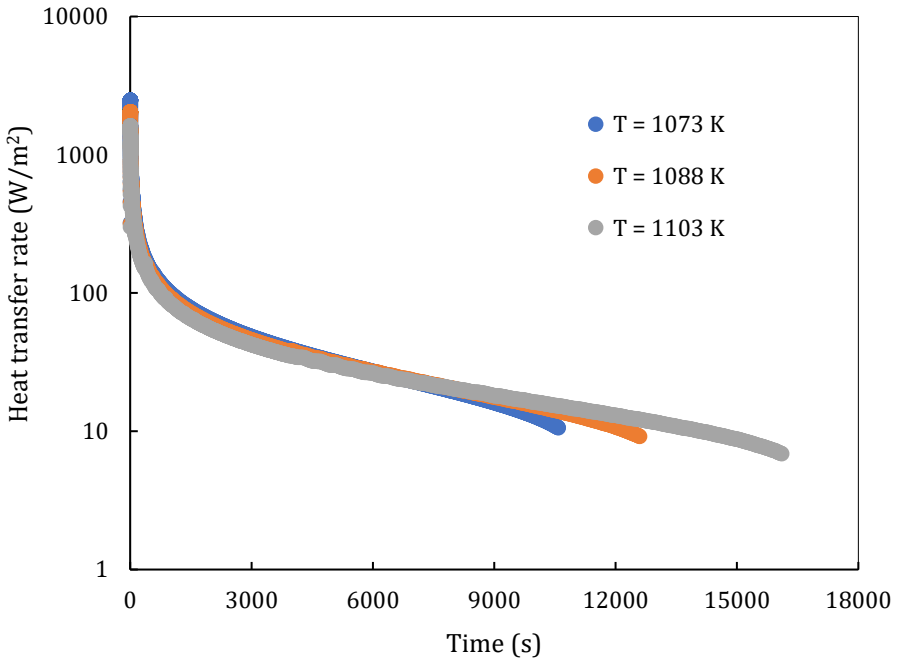

Figure 5.13: Effect of boundary temperature on the heat transfer rate at CO_2 pressure of 1 bar

Figure 5.13 illustrates the impact of the boundary temperature of the reactor on the heat transfer rate from the reactor. The heat transfer rate is highest when the temperature is

1073 K due to the more significant temperature gradient between the reactor bed and outer wall. The maximum heat transfer rate is ~2480, ~2050, and ~1610 W/m^2 when the boundary temperature is 1073, 1088, 1103 K, respectively. For all scenarios, the higher heat transfer rate is observed only in the initial phase of the reaction before quickly dropping to below 525 W/m^2 within 50 s.

5.7.4 Study of calcium carbonate reactor with graphite fin

Previous research has demonstrated that integrating an extended surface fin into a thermochemical reactor improves the reactor's heat transfer rate and performance. Therefore, a study was carried out to ascertain whether improved performance of a carbonate TES reactor would be improved with a graphite fin inserted into the centre of the reactor, as illustrated in Figure 5.14. To compare the performance of the reactor with and without the fin, the reactor bed thickness and height were kept constant at 100 mm (see Figure 5.4). The graphite fin has an outside diameter of 15.9 mm (5/8 inch) and a total length of 200 mm, of which 100 mm extends beyond the reactor bed. The thermophysical properties of the graphite fin provided by Toyo Tanso Co.Ltd were used in this investigation [189].

A constant boundary temperature of 1073 K was applied at the outer wall of the reactor bed. The extended graphite fin was assumed to undergo natural convective heat loss to the ambient. The ambient temperature was set to 298 K, and a heat transfer coefficient of 10 W/m^2.K (average value for natural convection for a vertical fin) was assumed. The initial temperature of both the reactor bed and the graphite fin was 1073 K, while a constant CO_2 supply pressure of 1 bar was applied. The investigations were performed under assumed thermal conductivity conditions of 1.33 and 5 W/m.K for the carbonate bed.

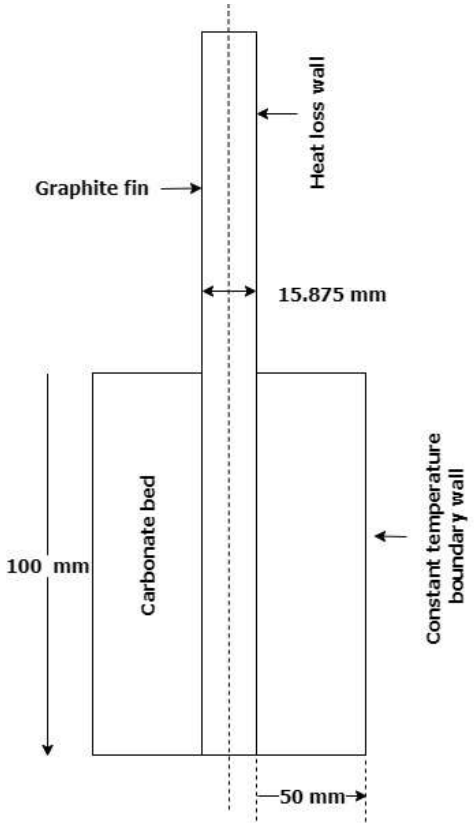

Figure 5.14: Schematic of carbonate reactor bed with graphite fin for numerical modelling

Figures 5.15 and 5.16 depict the contours of temperature and reacted fraction in the reactor bed over time intervals of 100, 500, 1000, and 2000 s. The temperature contour plots demonstrate that during the initial stages of the reaction, the temperature inside the reactor bed approaches ~ 1173 K for the two thermal conductivity values. The temperature of the reactor decreases over time as a result of heat absorption from the reactor bed. Due to the increased heat transfer, a faster temperature drops occur in the 5 W/m.K case than in the 1.33 W/m.K case. As a result, in the 5 W/m.K scenario, the carbonation process advances more rapidly. The reacted fraction contour indicates that most reactor materials are carbonated at 2000 s when the thermal conductivity of the bed was 5 W/m.K, whereas a significant amount of materials remain unreacted at 1.33 W/m.K. In addition, the reacted fraction contour demonstrates that the material at the outer boundary of the reactor and near the graphite fin carbonates more rapidly at higher thermal conductivity values. This is because these locations experience a significantly increased heat transfer coefficient, as such the reaction rate is increased when the thermal conductivity is higher.

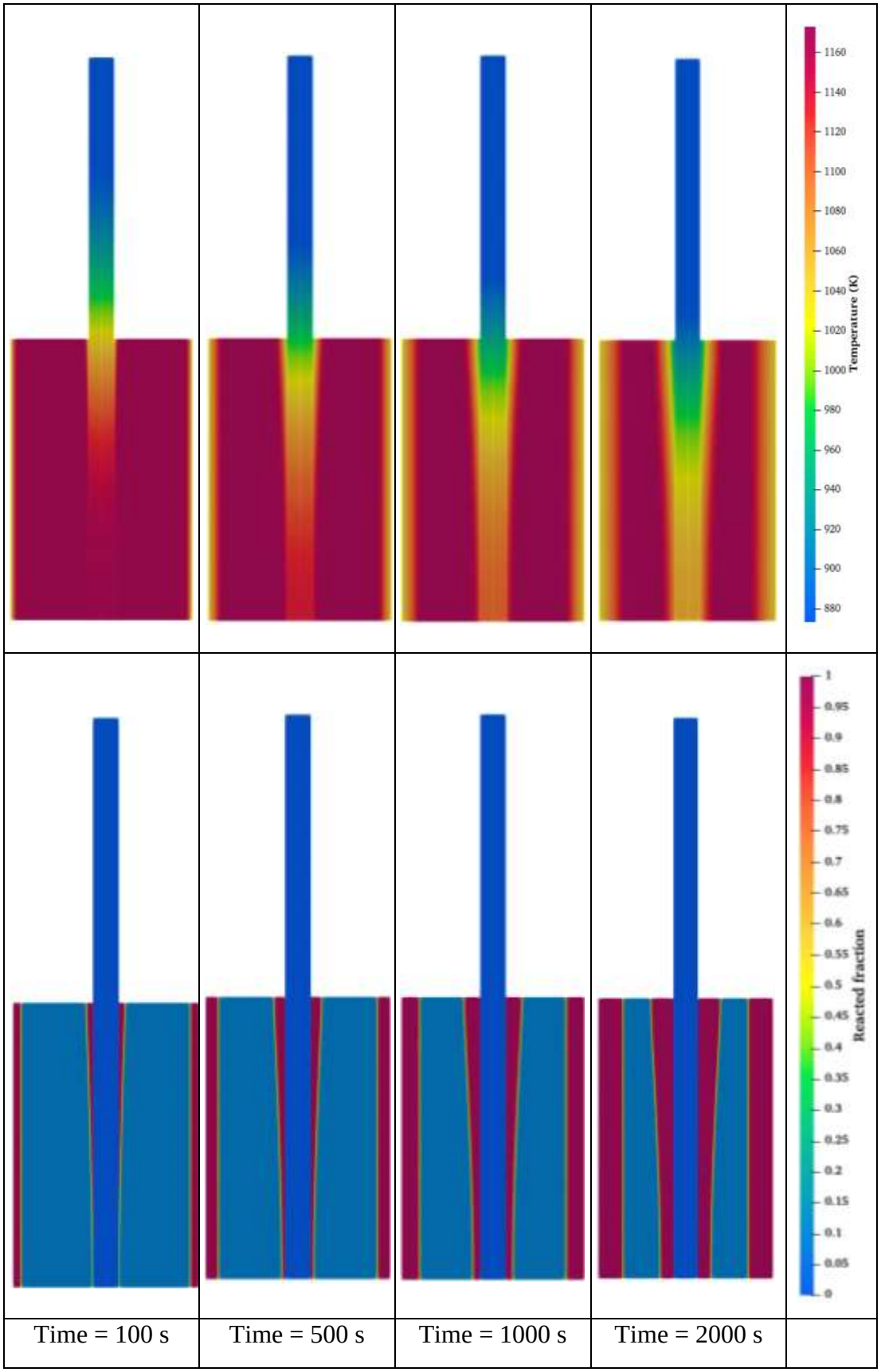

Figure 5.15: Distribution of the reactor's temperature (top rows) and reacted fraction (bottom rows) at various time intervals at a thermal conductivity of 1.33 W/m.K

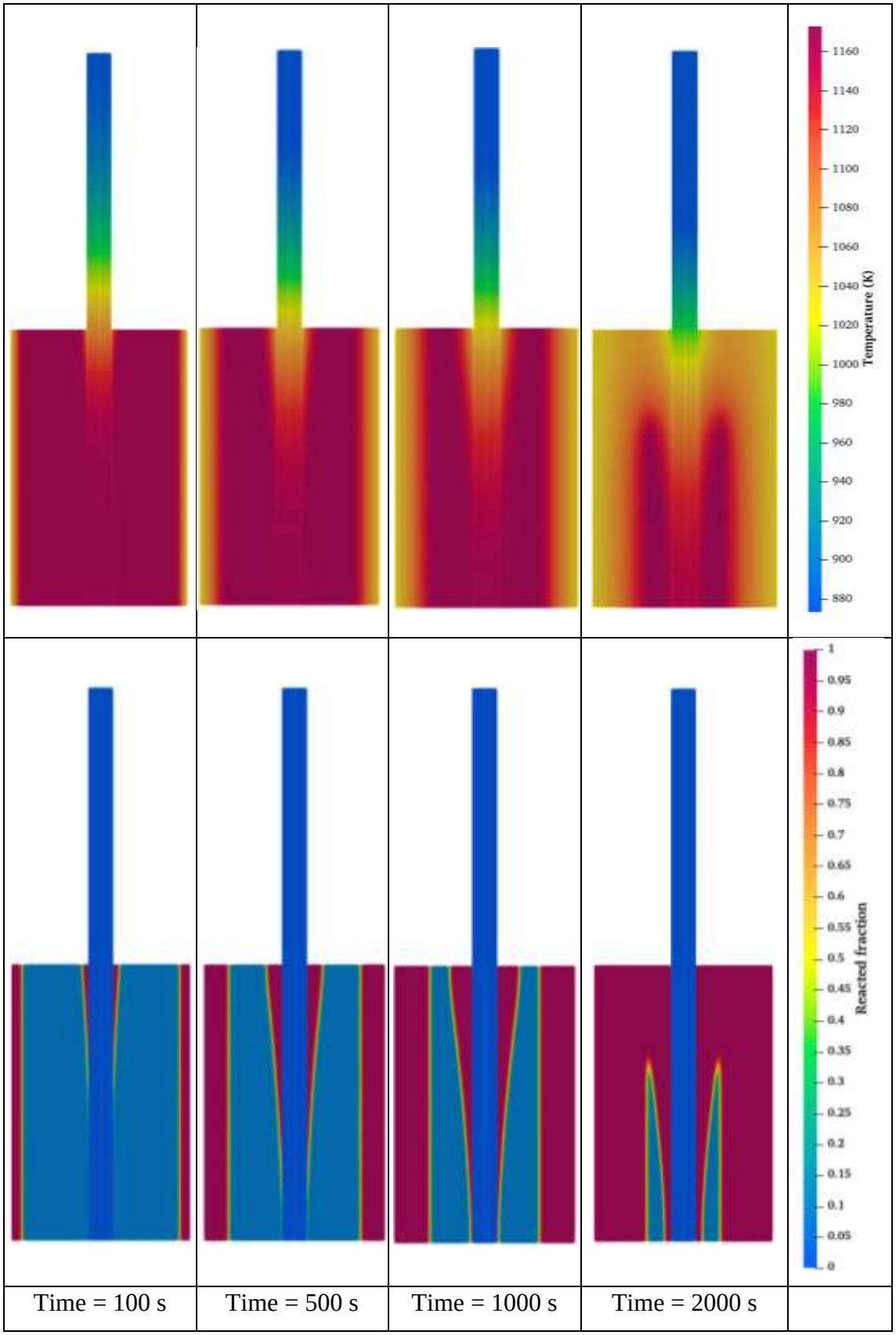

Figure 5.16: Distribution of the reactor's temperature (top rows) and reacted fraction (bottom rows) at various time intervals at a thermal conductivity of 5 W/m.K

Figure 5.17 compares the averaged reacted fraction of the reactor with and without a fin at the two thermal conductivity values studied. With a thermal conductivity of 1.33 /m.K, it is evident that with the graphite fin the reactor bed has greatly enhanced performance. The fin the reacted fraction remains identical among both designs until it reaches 0.4, at which point the carbonation reaction accelerates in the reactor with the fin and the reaction takes ~5910 s to complete, whereas the process extends and completes at ~10580 s in a rector without a fin. Interestingly, increasing the thermal conductivity of the bed to 5 W/m.K when the graphite fin is inserted has a negligible effect on the reactor's performance.

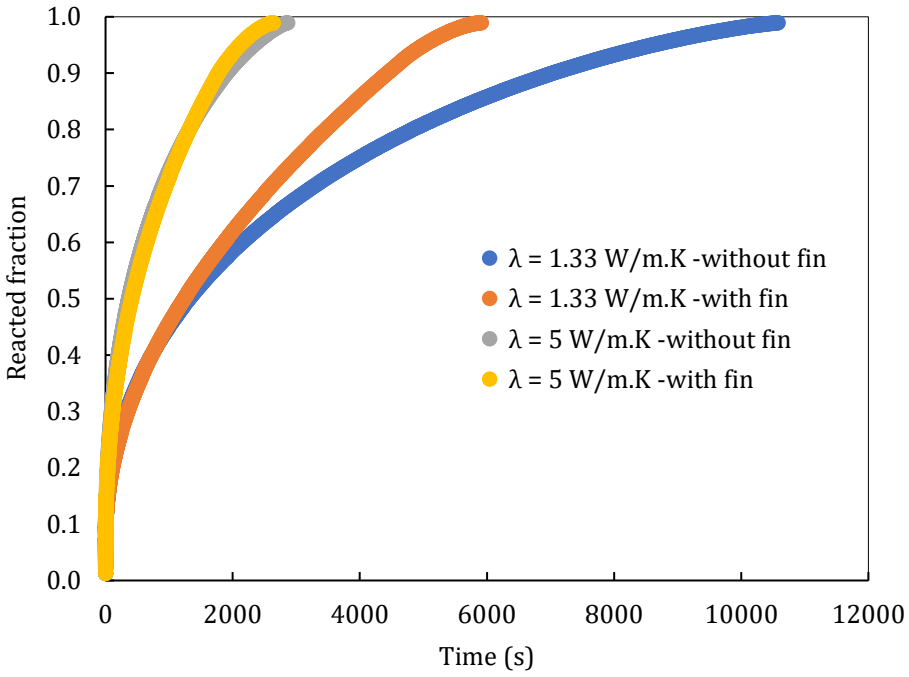

Figure 5.17: Comparison of averaged reacted fraction of reactor with and without the graphite fin at a thermal conductivity of 1.33 and 5 W/m.K

The absence of increased performance under higher thermal conductivity conditions is due to the reduced rate of heat transfer across the extended fins surface. The heat is transferred from the reactor bed in two ways: through the outer wall of the reactor and the extended graphite fin. Among these two methods, the major share of heat energy is removed from the reactor bed through the outer wall of the reactor. As the thermal conductivity of the reactor bed increases, the amount of heat energy transferred through the outer wall increases and the percentage of heat energy transferred through the outer wall further increases (or reduces the percentage of heat transfer through the extended fin). Additionally, due to the higher heat exchange, the reaction is finished significantly

faster in the high thermal conductivity condition. In contrast, the reaction takes a long time to complete low thermal conductivity case and a considerable amount of heat energy is transferred through the fin. This result in improved performance in the 1.33 W/m.K scenario and negligible performance gain in the 5 W/m. K.

The result emphasises the performance enhancement requirements for future $CaCO_3$ reactors. The reactor's performance can be improved by raising the reactor bed's thermal conductivity and increasing the reactor's heat transfer area by introducing an extended fin into the reactor. Both of these strategies, however, add complexity to the reactor's construction and incur additional costs. After weighing these variables, an appropriate approach for the future calcium carbonate reactor can be chosen. Furthermore, once the bed's higher thermal conductivity is achieved, the addition of the fin will not improve the reactor's performance any further. As a result, in large-scale $CaCO_3$ reactors, more optimisation studies of acceptable heat transfer improvement approaches would be necessary.

5.8 Conclusions

A mixture of $CaCO_3$ + 20 wt% Al_2O_3 has previously been shown to be a potential thermal energy storage material due to its operating temperature and ability to reversibly absorb CO_2 for more than 500 cycles. To date, numerical studies on this system have not been undertaken due to the requirement to determine the kinetic model for the CO_2 absorption process. TGA was used to measure the data and a kinetic model was obtained, and a numerical investigation of the cylindrical $CaCO_3$ reactor was conducted. The supply pressure of CO_2, the reactor bed's thermal conductivity, and the reactor wall's boundary temperature were considered for the parametric investigations. The conclusions can be drawn as follows:

- The kinetic study reveals that the carbonation reaction in the $CaCO_3/Al_2O_3$ takes place rapidly. The carbonation reaction follows the Avarami nucleation growth model with an exponent 3 reaction model.
- The time to complete the reaction reduces by ~37% when the applied pressure increases from 1 to 2 bar CO_2. However, as the applied pressure increases from 2 to 3 bar CO_2, only a 16% reduction is visible. The maximum temperature of the reactor bed increases from ~1159 K to ~1238 K when the applied CO_2 pressure rises from 1 to 3 bar.

- The carbonation reaction is ~ 73% faster when the thermal conductivity of the bed increases from 1.33 to 5 W/m.K. The maximum temperature of the reactor is independent of the thermal conductivity of the bed and the wall temperature of the reactor.
- A 34% performance improvement is shown in the reactor when the boundary wall temperature is reduced by 30 K.
- The carbonation reaction enhancement by adding a graphite fin to a reactor with thermal conductivity of 1.33 W/m.K is ~ 44%, while the effect on a reactor with thermal conductivity of 5 W/m.K is negligible.

5.9 Declaration of competing interest

The authors declare that they have no known competing financial interests or personal relationships that could have appeared to influence the work reported in this paper.

5.10 Acknowledgements

CEB, TC, TDH and AM acknowledge the financial support of the Australian Research Council (ARC) for Linkage Project LP150100730. CEB, MP and TDH acknowledge the financial support of the Global Innovation Linkage grant (GIL73589). MP also acknowledges the ARC for Future Fellowship FT160100303. This work was supported by resources provided by the Pawsey Supercomputing Centre with funding from the Australian Government and the Government of Western Australia.

CHAPTER 6: CONCLUSIONS

6.1 Introduction

This thesis presented a research investigation examining the thermal performance of thermochemical energy storage reactors suitable for applications in high temperature concentrated solar systems. An advanced numerical model was successfully developed for simulating the reactor packed bed thermal behaviour using both single-phase and (multi-phase) flow boiling mechanisms for heat exchange in the reactor. Two types of packed bed storage media, namely magnesium hydride (MgH_2) and calcium carbonate ($CaCO_3$), were analysed for performance comparison providing different reaction kinetics. Potential benefits from enhancing thermal conductivity of the packed beds were examined with the introduction of specific doping compounds for the storage media. The predicted outcomes were validated against the experimental data, ascertaining the modelling accuracy and establishing the simulation as a useful design tool for designing and optimising thermochemical energy storage systems. As such, this study represents the most comprehensive analysis to-date on thermochemical energy storage, covering multi-phase heat transfer coupled with reaction kinetics in the reactor storage media.

A clearer understanding on thermal response, parametric behaviour and energy storage capabilities in reactors was derived through the study. This serves to promote wider use of such energy storage systems in concentrated solar collector systems, transposing them to be a practically continuous, reliable and sustainable option for applications in thermal power generation. It is therefore envisaged that, with the tangible benefits realised, the concentrated solar power plants using high-temperature thermochemical energy storage will gain much higher recognition among other storage methods for meeting baseload power demand, whilst offering options for reduced environmental impact from greenhouse gas emissions.

The specific conclusions derived from the study and its outcomes are outlined below.

6.2 Conclusions

In capturing potential gaps in the current state of knowledge, the study conducted a comprehensive literature review of reported research work on thermochemical reactors for applications in concentrated solar power plants. It has been identified that the thermochemical reactor performance is primarily dependent on the reversibility of

reaction kinetics associated with the storage material, its thermophysical properties and, the operating pressure and temperature. With the chemical reactions occurring in the reactor bed, a significant level of heat energy is generated, causing a rapid temperature rise in the storage medium. The high medium temperature feeds back to the thermochemical process to reduce its sustainable rate of reaction, thus adversely affecting the overall reactor storage performance. Hence an efficient heat exchange within the reactor is concluded to be critical for improving energy storage potential of this technology. In line with these observations, previous studies have largely followed single-phase fluid heat exchange along with high packed bed thermal conductivity as a useful heat exchange principles. The packed bed media have been routinely doped in tests with suitable compounds to raise its effective thermal conductivity with some degree of benefit. Other possible flow heat transfer mechanisms, such as multi-phase behaviour in heat exchange fluids have not been appraised in the published literature.

Most of the reported work on thermochemical reactors is limited to conventional experimentation with different types of storage media and evaluating reaction kinetics. These are constrained by measurement uncertainties, manufacturing difficulties and material inconsistencies. Similarly, numerical investigations are lacking and limited in scope due to the inherent modelling complexities arising from reactor configurations. Nonetheless, for parametric optimisation of thermochemical energy storage systems, the literature clearly recognises the crucial role offered by developing numerical investigations as a design tool that would support the advancement of concentrated solar systems technology. In terms of suitable media for thermochemical reactors, the published literature identifies magnesium hydride and calcium carbonate having appropriate characteristics for high-temperature thermal energy storage. In addressing these shortfalls, the current research study successfully developed an advanced and validated numerical study on high-temperature thermal energy storage with the chosen media of magnesium hydride and calcium carbonate. The effects of doping these packed bed media with thermal enhancing compounds were also considered to ascertain any benefits. As a novel contribution to the field from the current study, both single and multiphase flow mechanisms within the reactor heat transfer fluid were modelled and the resulting performances were compared.

In the first stage of the current study, a three-dimensional numerical investigation was developed and carried out on a magnesium hydride (MgH_2) reactor with a helical passage

carrying single-phase heat transfer fluid for heat exchange in the packed bed. A kinetics investigation was performed using Sievert's apparatus to obtain the reaction rate of the hydrogenation process. It was found that the hydrogenation reaction of magnesium hydride compound follows the Avrami nucleation growth model with an exponent 2. The numerical model was validated against the experimental data of a magnesium hydride reactor conducted under known and realistic operating conditions.

In previously reported work, increased bed thermal conductivity has been deployed as a possible performance enhancement strategy only under adiabatic boundary conditions. This boundary condition is difficult to achieve and unrealistic owing to inevitable heat losses from the reactor, especially at elevated reactor temperatures. The current study considered both adiabatic and heat loss boundary conditions in the analysis, hence facilitating more realistic judgement on reactor performance. The investigation examined and compared the reacted fraction during hydrogenation in the reactor beds having thermal conductivities of 0.48 and 13.4 W/m.K, with the imposed adiabatic and heat loss boundary conditions. Significant performance improvements were observed when the thermal conductivity of the magnesium hydride bed was increased under adiabatic boundary conditions. However, enhancing bed thermal conductivity did not produce improved performance with heat loss boundary conditions. Therefore, it is concluded that seeking performance improvement through altering bed thermal conductivity is design rationale with limited applicability. Moreover, it is noted that, the inclusion of any doping material in a reactor bed would incur additional cost and reduce the availability of energy storage density in the storage medium, thus adversely influencing reactor design and development.

The analysis examined the influence of heat transfer fluid flowrate and hydrogen supply pressure on the performance of the magnesium hydride reactor. A 50% reduction in hydrogenation time was evident when the fluid flow rate was increased from 4 ml/min to 10 ml/min. Thus, it is concluded that the increased flow rate of the heat transfer fluid accelerates the hydrogenation process and reduces the time required to complete it. This is attributed to the increased reduction is bed temperature resulting from improved cooling due to faster flow rate. A higher heat transfer fluid flow rate through an energy storage system is not necessarily favourable, because it decreases the heat-carrying capacity of a thermal energy conversion device connected to the thermochemical reactor,

which determines its efficiency. Therefore, such a flow rate needs to be optimised as a linked system.

Similarly, a 37% reduction in hydrogenation time is observed with the hydrogen supply pressure is increased from 7 to 9 bar, leading to the conclusion that increased hydrogen supply pressure accelerates the reaction rate and completes the hydrogenation reaction quickly. However, elevation of higher hydrogen pressure necessitates a more powerful compressor, which increases the compressor's energy consumption. Thus, an optimal applied pressure must be maintained in the reactor, taking into account the energy consumed by the compressor and the performance gain associated with the increased operating pressure.

This investigation considered as a novel approach, multi-phase heat transfer in the reactor bed to lower its operating temperature that is shown to cause degradation in reactor performance. The numerical model developed was successfully amended using Eulerian two-fluid framework to account for flow boiling situation in the heat transfer fluid. The resulting reactor performance using flow boiling was compared with that of single-phase heat transfer. With flow boiling, a higher amount of heat energy was evidently absorbed from the reactor and accelerated the hydrogenation reaction. This approach is highly proposed by the study as an enhancement strategy. However, monitoring and controlling heat flux is critical to ensure the heat collection tube does not reach the dry-out condition during operation. Further heat transfer enhancements in the multiphase flow can be achieved by regulating the subcooled temperature of the heat transfer fluid, to aim for a longer boiling domain in tubes and avoiding dry-out conditions during the hydrogenation.

In the second stage of the investigation, the simulation analysis focused on modelling a limestone-based calcium carbonate ($CaCO_3$) reactor for high-temperature thermal energy storage application. A carbonation kinetics study of the $CaCO_3$ doped with 20% Al_2O_3 was conducted using the TGA apparatus. The kinetic study found that the carbonation reaction in the material follows the Avrami nucleation growth model with exponent 3. Moreover, the kinetic study revealed that the $CaCO_3/Al_2O_3$ compound's carbonation reaction has extremely fast kinetics, which is advantageous for high-temperature thermal energy storage applications.

As before, the effect of carbon dioxide (CO_2) supply pressure, reactor bed thermal conductivity and reactor wall boundary temperature on reactor performance were investigated numerically using the reaction kinetics obtained. The findings indicated that, increasing the applied CO_2 pressure from 1.0 to 2.0 bar decreased the time required to complete the reaction by 37%. However, when the applied pressure was raised from 2.0 to 3.0 bars, the reaction time fell only by 16%, indicating a weaker influence from elevated pressure beyond a point. Similarly, increasing the thermal conductivity of the bed from 1.33 to 5.0 W/m.K enhanced the carbonation reaction by 73%.

Conversely, in the real-world applications, the constant temperature boundary condition assumption is correlated to the effect of temperature rise in the heat collecting fluid on the overall performance of the reactor. Hence it is necessary to examine the wall temperature in preference to the adiabatic conditions. In those lines, when the boundary wall temperature of the reactor rose from 1073 to 1103 K, a 35% reduction in performance was noticed. The reactor bed's maximum temperature was increased from 1159 to 1238 K as the CO_2 pressure was increased from 1.0 to 3.0 bar. However, the maximum temperature was unaffected by the thermal conductivity of the bed or the boundary temperature of the reactor.

The investigation also examined the impact from a configuration modification to the $CaCO_3$ reactor bed, by adding an extended graphite fin to vary the effective bed thermal conductivity. This study indicated that, adding the graphite fin to the reactor bed increased the carbonation reaction by 44% in reactor beds with thermal conductivity of 1.33 W/m.K. However, there was no observable effect with a bed thermal conductivity of 5.0 W/m.K.

This difference in the performance enhancement can be attributed to the amount of heat transfer through the fins. In the high thermal conductivity case, the amount of heat transfer through the extended fin was negligible compared to the heat transfer through the outer boundary wall of the reactor. Contrarily, considerable amount of heat transfer occurred through the expanded fin at a low thermal conductivity case. The overall observation indicates that the performance improvement in the reactor bed due to the addition of extended fins depend on the thermal conductivity of the reactor bed.

6.3 Future Work

The development of high-temperature thermochemical reactors is vital for future development of thermal energy storage systems associated with concentrated solar power plants. In line with the current work, the following areas have the potential for future research. Calcium carbonate doped with Al_2O_3 is recognised to have considerable promise for use as a thermal storage material. Consequently, investigation of large-scale calcium carbonate reactors equipped with an efficient heat exchanger system will be beneficial. Furthermore, it would be much favourable if multiphase heat absorption is combined with high-temperature heat transfer fluid, such as liquid sodium. Additionally, a numerical investigation of multiphase flow optimisation in the high-temperature reactor's heat exchanging system is much desired for the advancement of the thermal energy storage system.

References

[1] Nukiyama S. The maximum and minimum values of the heat Q transmitted from metal to boiling water under atmospheric pressure. International Journal of Heat and Mass Transfer. 1966;9:1419-33.
[2] Ansys® Academic Research Mechanical R, Help System, ANSYS-FLUENT Theory Guide, ANSYS, Inc.
[3] Roser HRaM. CO_2 and Greenhouse Gas Emissions. Our World in Data. 2020.
[4] Roser HRaM. Energy. Published online at OurWorldInDataorg. 2020.
[5] Goswami DY. Principles of Solar Engineering. 3rd ed.;. Taylor and Francis Group. 2015.
[6] Wood T, Blowers, D., and Chisholm, C. Sundown, sunrise: how Australia can finally get solar PV right, Grattan Institute. 2015.
[7] Pelay U, Luo L, Fan Y, Stitou D, Rood M. Thermal energy storage systems for concentrated solar power plants. Renewable and Sustainable Energy Reviews. 2017;79:82-100.
[8] Li B, Li J, Shao H, He L. Mg-Based Hydrogen Absorbing Materials for Thermal Energy Storage—A Review. Applied Sciences. 2018;8:1375.
[9] Wu S, Zhou C, Doroodchi E, Nellore R, Moghtaderi B. A review on high-temperature thermochemical energy storage based on metal oxides redox cycle. Energy Conversion and Management. 2018;168:421-53.
[10] Sheppard DA, Paskevicius M, Humphries TD, Felderhoff M, Capurso G, Bellosta von Colbe J, et al. Metal hydrides for concentrating solar thermal power energy storage. Applied Physics A. 2016;122:395.
[11] Fellet M, Buckley CE, Paskevicius M, Sheppard DA. Research on metal hydrides revived for next-generation solutions to renewable energy storage. MRS Bulletin. 2013;38:1012-3.
[12] Manickam K, Mistry P, Walker G, Grant D, Buckley CE, Humphries TD, et al. Future perspectives of thermal energy storage with metal hydrides. International Journal of Hydrogen Energy. 2019.
[13] Kawamura M, Ono S, Higano S. Experimental studies on the behaviours of hydride heat storage system. Energy Conversion and Management. 1982;22:95-102.
[14] Bogdanović B, Ritter A, Spliethoff B, Straβburger K. A process steam generator based on the high temperature magnesium hydride/magnesium heat storage system. International Journal of Hydrogen Energy. 1995;20:811-22.
[15] Reiser A, Bogdanović B, Schlichte K. The application of Mg-based metal-hydrides as heat energy storage systems. International Journal of Hydrogen Energy. 2000;25:425-30.
[16] Satya Sekhar B, Muthukumar P, Saikia R. Tests on a metal hydride based thermal energy storage system. International Journal of Hydrogen Energy. 2012;37:3818-24.
[17] Askri F, Jemni A, Ben Nasrallah S. Study of two-dimensional and dynamic heat and mass transfer in a metal–hydrogen reactor. International Journal of Hydrogen Energy. 2003;28:537-57.
[18] Marty P, Fourmigue JF, Rango PD, Fruchart D, Charbonnier J. Numerical simulation of heat and mass transfer during the absorption of hydrogen in a magnesium hydride. Energy Conversion and Management. 2006;47:3632-43.
[19] Chaise A, de Rango P, Marty P, Fruchart D. Experimental and numerical study of a magnesium hydride tank. International Journal of Hydrogen Energy. 2010;35:6311-22.
[20] Chung CA, Lin C-S. Prediction of hydrogen desorption performance of Mg2Ni hydride reactors. International Journal of Hydrogen Energy. 2009;34:9409-23.
[21] Chaise A, Marty P, Rango Pd, Fruchart D. A simple criterion for estimating the effect of pressure gradients during hydrogen absorption in a hydride reactor. International Journal of Heat and Mass Transfer. 2009;52:4564-72.
[22] Shen D, Zhao CY. Thermal analysis of exothermic process in a magnesium hydride reactor with porous metals. Chemical Engineering Science. 2013;98:273-81.
[23] Bao Z, Yang F, Wu Z, Cao X, Zhang Z. Simulation studies on heat and mass transfer in high-temperature magnesium hydride reactors. Applied Energy. 2013;112:1181-9.
[24] Bao Z, Yang F, Wu Z, Nyallang Nyamsi S, Zhang Z. Optimal design of metal hydride reactors based on CFD–Taguchi combined method. Energy Conversion and Management. 2013;65:322-30.

[25] Bao Z, Wu Z, Nyamsi SN, Yang F, Zhang Z. Three-dimensional modeling and sensitivity analysis of multi-tubular metal hydride reactors. Applied Thermal Engineering. 2013;52:97-108.
[26] Wu Z, Yang F, Zhang Z, Bao Z. Magnesium based metal hydride reactor incorporating helical coil heat exchanger: Simulation study and optimal design. Applied Energy. 2014;130:712-22.
[27] Ma J, Wang Y, Shi S, Yang F, Bao Z, Zhang Z. Optimization of heat transfer device and analysis of heat & mass transfer on the finned multi-tubular metal hydride tank. International Journal of Hydrogen Energy. 2014;39:13583-95.
[28] Mellouli S, Ben Khedher N, Askri F, Jemni A, Ben Nasrallah S. Numerical analysis of metal hydride tank with phase change material. Applied Thermal Engineering. 2015;90:674-82.
[29] Ben Mâad H, Askri F, Ben Nasrallah S. Numerical investigation of heat and mass transfer during the desorption process of an Mg2Ni–H2 reactor. International Journal of Hydrogen Energy. 2013;38:4597-610.
[30] Ferekh S, Gwak G, Kyoung S, Kang H-g, Chang M-h, Yun S-h, et al. Numerical comparison of heat-fin- and metal-foam-based hydrogen storage beds during hydrogen charging process. International Journal of Hydrogen Energy. 2015;40:14540-50.
[31] Bao Z, Yuan S. Performance investigation of thermal energy storage systems using metal hydrides adopting multi-step operation concept. International Journal of Hydrogen Energy. 2016;41:5361-70.
[32] Lévesque S, Ciureanu M, Roberge R, Motyka T. Hydrogen storage for fuel cell systems with stationary applications— I. Transient measurement technique for packed bed evaluation. International Journal of Hydrogen Energy. 2000;25:1095-105.
[33] Nagel M, Komazaki Y, Suda S. Effective thermal conductivity of a metal hydride bed augmented with a copper wire matrix. Journal of the Less Common Metals. 1986;120:35-43.
[34] Mellouli S, Dhaou H, Askri F, Jemni A, Ben Nasrallah S. Hydrogen storage in metal hydride tanks equipped with metal foam heat exchanger. International Journal of Hydrogen Energy. 2009;34:9393-401.
[35] Chaise A, de Rango P, Marty P, Fruchart D, Miraglia S, Olivès R, et al. Enhancement of hydrogen sorption in magnesium hydride using expanded natural graphite. International Journal of Hydrogen Energy. 2009;34:8589-96.
[36] Souahlia A, Dhaou H, Askri F, Mellouli S, Jemni A, Ben Nasrallah S. Experimental study and characterization of metal hydride containers. International Journal of Hydrogen Energy. 2011;36:4952-7.
[37] Singh A, Maiya MP, Murthy SS. Effects of heat exchanger design on the performance of a solid state hydrogen storage device. International Journal of Hydrogen Energy. 2015;40:9733-46.
[38] Nyamsi SN, Yang F, Zhang Z. An optimization study on the finned tube heat exchanger used in hydride hydrogen storage system – analytical method and numerical simulation. International Journal of Hydrogen Energy. 2012;37:16078-92.
[39] Dhaou H, Souahlia A, Mellouli S, Askri F, Jemni A, Ben Nasrallah S. Experimental study of a metal hydride vessel based on a finned spiral heat exchanger. International Journal of Hydrogen Energy. 2010;35:1674-80.
[40] Li H, Wang Y, He C, Chen X, Zhang Q, Zheng L, et al. Design and performance simulation of the spiral mini-channel reactor during H2 absorption. International Journal of Hydrogen Energy. 2015;40:13490-505.
[41] Visaria M, Mudawar I. Coiled-tube heat exchanger for High-Pressure Metal Hydride hydrogen storage systems – Part 1. Experimental study. International Journal of Heat and Mass Transfer. 2012;55:1782-95.
[42] Dong D, Humphries TD, Sheppard DA, Stansby B, Paskevicius M, Sofianos MV, et al. Thermal optimisation of metal hydride reactors for thermal energy storage applications. Sustainable Energy & Fuels. 2017;1:1820-9.
[43] Linder M, Mertz R, Laurien E. Experimental analysis of fast metal hydride reaction bed dynamics. International Journal of Hydrogen Energy. 2010;35:8755-61.

[44] Oi T, Maki K, Sakaki Y. Heat transfer characteristics of the metal hydride vessel based on the plate-fin type heat exchanger. Journal of Power Sources. 2004;125:52-61.
[45] Askri F, Ben Salah M, Jemni A, Ben Nasrallah S. Optimization of hydrogen storage in metal-hydride tanks. International Journal of Hydrogen Energy. 2009;34:897-905.
[46] Chacartegui R, Alovisio A, Ortiz C, Valverde JM, Verda V, Becerra JA. Thermochemical energy storage of concentrated solar power by integration of the calcium looping process and a CO2 power cycle. Applied Energy. 2016;173:589-605.
[47] Ortiz C, Chacartegui R, Valverde JM, Alovisio A, Becerra JA. Power cycles integration in concentrated solar power plants with energy storage based on calcium looping. Energy Conversion and Management. 2017;149:815-29.
[48] Ylätalo J, Parkkinen J, Ritvanen J, Tynjälä T, Hyppänen T. Modeling of the oxy-combustion calciner in the post-combustion calcium looping process. Fuel. 2013;113:770-9.
[49] Ortiz C, Chacartegui R, Valverde JM, Becerra JA, Perez-Maqueda LA. A new model of the carbonator reactor in the calcium looping technology for post-combustion CO2 capture. Fuel. 2015;160:328-38.
[50] Sanchez-Jimenez PE, Valverde JM, Perez-Maqueda LA. Multicyclic conversion of limestone at Ca-looping conditions: The role of solid-sate diffusion controlled carbonation. Fuel. 2014;127:131-40.
[51] Wu W, Chen S-C, Kuo P-C, Chen S-A. Design and optimization of stand-alone triple combined cycle systems using calcium looping technology. Journal of Cleaner Production. 2017;140:1049-59.
[52] Wang X, Gao J, Jiang L. Feasibility analysis of H2 production by calcium looping process based on coal gasification in a transport reactor. International Journal of Hydrogen Energy. 2016;41:12000-18.
[53] Barker R. The reactivity of calcium oxide towards carbon dioxide and its use for energy storage. Journal of Applied Chemistry and Biotechnology. 1974;24:221-7.
[54] Pardo P, Deydier A, Anxionnaz-Minvielle Z, Rougé S, Cabassud M, Cognet P. A review on high temperature thermochemical heat energy storage. Renewable and Sustainable Energy Reviews. 2014;32:591-610.
[55] Prieto C, Cooper P, Fernández AI, Cabeza LF. Review of technology: Thermochemical energy storage for concentrated solar power plants. Renewable and Sustainable Energy Reviews. 2016;60:909-29.
[56] Edwards SEB, Materić V. Calcium looping in solar power generation plants. Solar Energy. 2012;86:2494-503.
[57] Alovisio A, Chacartegui R, Ortiz C, Valverde JM, Verda V. Optimizing the CSP-Calcium Looping integration for Thermochemical Energy Storage. Energy Conversion and Management. 2017;136:85-98.
[58] Valverde JM, Sanchez-Jimenez PE, Perez-Maqueda LA. Ca-looping for postcombustion CO2 capture: A comparative analysis on the performances of dolomite and limestone. Applied Energy. 2015;138:202-15.
[59] Sánchez-Jiménez PE, Valverde JM, Perejón A, de la Calle A, Medina S, Pérez-Maqueda LA. Influence of Ball Milling on CaO Crystal Growth During Limestone and Dolomite Calcination: Effect on CO2 Capture at Calcium Looping Conditions. Crystal Growth & Design. 2016;16:7025-36.
[60] Valverde JM, Sanchez-Jimenez PE, Perez-Maqueda LA. Role of precalcination and regeneration conditions on postcombustion CO2 capture in the Ca-looping technology. Applied Energy. 2014;136:347-56.
[61] Manovic V, Anthony EJ. Thermal Activation of CaO-Based Sorbent and Self-Reactivation during CO2 Capture Looping Cycles. Environmental Science & Technology. 2008;42:4170-4.
[62] Manovic V, Anthony EJ. Steam Reactivation of Spent CaO-Based Sorbent for Multiple CO2 Capture Cycles. Environmental Science & Technology. 2007;41:1420-5.
[63] Sun J, Liu W, Li M, Yang X, Wang W, Hu Y, et al. Mechanical Modification of Naturally Occurring Limestone for High-Temperature CO2 Capture. Energy & Fuels. 2016;30:6597-605.
[64] Sun P, Grace JR, Lim CJ, Anthony EJ. Investigation of Attempts to Improve Cyclic CO2 Capture by Sorbent Hydration and Modification. Industrial & Engineering Chemistry Research. 2008;47:2024-32.

[65] Møller KT, Ibrahim A, Buckley CE, Paskevicius M. Inexpensive thermochemical energy storage utilising additive enhanced limestone. Journal of Materials Chemistry A. 2020;8:9646-53.
[66] Li Q, Jiang L-j, Chou K-c, Lin Q, Zhan F, Xu K-d, et al. Effect of hydrogen pressure on hydriding kinetics in the Mg2−xAgxNi–H (x=0.05, 0.1) system. Journal of Alloys and Compounds. 2005;399:101-5.
[67] Liu J, Zhang X, Li Q, Chou K-C, Xu K-D. Investigation on kinetics mechanism of hydrogen absorption in the La2Mg17-based composites. International Journal of Hydrogen Energy. 2009;34:1951-7.
[68] Li Q, Chou K-C, Lin Q, Jiang L-J, Zhan F. Hydrogen absorption and desorption kinetics of Ag–Mg–Ni alloys. International Journal of Hydrogen Energy. 2004;29:843-9.
[69] Abbott D. Keeping the Energy Debate Clean: How Do We Supply the World's Energy Needs? Proceedings of the IEEE. 2010;98:42-66.
[70] Zalba B, Marín JM, Cabeza LF, Mehling H. Review on thermal energy storage with phase change: materials, heat transfer analysis and applications. Applied Thermal Engineering. 2003;23:251-83.
[71] Aydin D, Casey SP, Riffat S. The latest advancements on thermochemical heat storage systems. Renewable and Sustainable Energy Reviews. 2015;41:356-67.
[72] Hirscher M, Yartys VA, Baricco M, Bellosta von Colbe J, Blanchard D, Bowman RC, et al. Materials for hydrogen-based energy storage – past, recent progress and future outlook. Journal of Alloys and Compounds. 2020;827:153548.
[73] Harries DN, Paskevicius M, Sheppard DA, Price TEC, Buckley CE. Concentrating Solar Thermal Heat Storage Using Metal Hydrides. Proceedings of the IEEE. 2012;100:539-49.
[74] Jia Y, Sun C, Shen S, Zou J, Mao SS, Yao X. Combination of nanosizing and interfacial effect: Future perspective for designing Mg-based nanomaterials for hydrogen storage. Renewable and Sustainable Energy Reviews. 2015;44:289-303.
[75] Wang H, Lin HJ, Cai WT, Ouyang LZ, Zhu M. Tuning kinetics and thermodynamics of hydrogen storage in light metal element based systems – A review of recent progress. Journal of Alloys and Compounds. 2016;658:280-300.
[76] Yartys VA, Lototskyy MV, Akiba E, Albert R, Antonov VE, Ares JR, et al. Magnesium based materials for hydrogen based energy storage: Past, present and future. International Journal of Hydrogen Energy. 2019.
[77] Sheppard DA, Paskevicius M, Buckley CE. Thermodynamics of Hydrogen Desorption from NaMgH3and Its Application As a Solar Heat Storage Medium. Chemistry of Materials. 2011;23:4298-300.
[78] Poupin L, Humphries TD, Paskevicius M, Buckley CE. A thermal energy storage prototype using sodium magnesium hydride. Sustainable Energy & Fuels. 2019;3:985-95.
[79] Sheppard DA, Corgnale C, Hardy B, Motyka T, Zidan R, Paskevicius M, et al. Hydriding Characteristics of $NaMgH_2F$ with Preliminary Technical and Cost Evaluation of Magnesium-Based Metal Hydride Materials for Concentrating Solar Power Thermal Storage. RSC Adv. 2014;4:26552-62.
[80] Ward PA, Corgnale C, Teprovich JA, Motyka T, Hardy B, Peters B, et al. High performance metal hydride based thermal energy storage systems for concentrating solar power applications. Journal of Alloys and Compounds. 2015;645:S374-S8.
[81] Paskevicius M, Sheppard DA, Williamson K, Buckley CE. Metal hydride thermal heat storage prototype for concentrating solar thermal power. Energy. 2015;88:469-77.
[82] Mohammadshahi SS, Gray EM, Webb CJ. A review of mathematical modelling of metal-hydride systems for hydrogen storage applications. International Journal of Hydrogen Energy. 2016;41:3470-84.
[83] Muthukumar P, Madhavakrishna U, Dewan A. Parametric studies on a metal hydride based hydrogen storage device. International Journal of Hydrogen Energy. 2007;32:4988-97.
[84] Bao Z. Performance investigation and optimization of metal hydride reactors for high temperature thermochemical heat storage. International Journal of Hydrogen Energy. 2015;40:5664-76.

[85] Feng P, Zhu L, Zhang Y, Yang F, Wu Z, Zhang Z. Optimum output temperature setting and an improved bed structure of metal hydride hydrogen storage reactor for thermal energy storage. International Journal of Hydrogen Energy. 2019;44:19313-25.
[86] Lototskyy M, Satya Sekhar B, Muthukumar P, Linkov V, Pollet BG. Niche applications of metal hydrides and related thermal management issues. Journal of Alloys and Compounds. 2015;645:S117-S22.
[87] Afzal M, Mane R, Sharma P. Heat transfer techniques in metal hydride hydrogen storage: A review. International Journal of Hydrogen Energy. 2017;42:30661-82.
[88] Laurencelle F, Goyette J. Simulation of heat transfer in a metal hydride reactor with aluminium foam. International Journal of Hydrogen Energy. 2007;32:2957-64.
[89] Raju M, Kumar S. System simulation modeling and heat transfer in sodium alanate based hydrogen storage systems. International Journal of Hydrogen Energy. 2011;36:1578-91.
[90] Klein H-P, Groll M. Heat transfer characteristics of expanded graphite matrices in metal hydride beds. International Journal of Hydrogen Energy. 2004;29:1503-11.
[91] Pohlmann C, Röntzsch L, Kalinichenka S, Hutsch T, Kieback B. Magnesium alloy-graphite composites with tailored heat conduction properties for hydrogen storage applications. International Journal of Hydrogen Energy. 2010;35:12829-36.
[92] Botzung M, Chaudourne S, Gillia O, Perret C, Latroche M, Percheron-Guegan A, et al. Simulation and experimental validation of a hydrogen storage tank with metal hydrides. International Journal of Hydrogen Energy. 2008;33:98-104.
[93] Andreasen G, Melnichuk M, Ramos S, Corso HL, Visintin A, Triaca WE, et al. Hydrogen desorption from a hydride container under different heat exchange conditions. International Journal of Hydrogen Energy. 2013;38:13352-9.
[94] Chung CA, Yang S-W, Yang C-Y, Hsu C-W, Chiu P-Y. Experimental study on the hydrogen charge and discharge rates of metal hydride tanks using heat pipes to enhance heat transfer. Applied Energy. 2013;103:581-7.
[95] Mellouli S, Askri F, Dhaou H, Jemni A, Ben Nasrallah S. Numerical simulation of heat and mass transfer in metal hydride hydrogen storage tanks for fuel cell vehicles. International Journal of Hydrogen Energy. 2010;35:1693-705.
[96] Raju M, Kumar S. Optimization of heat exchanger designs in metal hydride based hydrogen storage systems. International Journal of Hydrogen Energy. 2012;37:2767-78.
[97] Lewis SD, Chippar P. Numerical investigation of hydrogen absorption in a metal hydride reactor with embedded embossed plate heat exchanger. Energy. 2020;194:116942.
[98] Chandra S, Sharma P, Muthukumar P, Tatiparti SSV. Modeling and numerical simulation of a 5 kg LaNi5-based hydrogen storage reactor with internal conical fins. International Journal of Hydrogen Energy. 2020;45:8794-809.
[99] Kumar A, Raju NN, Muthukumar P, Selvan PV. Experimental studies on industrial scale metal hydride based hydrogen storage system with embedded cooling tubes. International Journal of Hydrogen Energy. 2019;44:13549-60.
[100] Satya Sekhar B, Lototskyy M, Kolesnikov A, Moropeng ML, Tarasov BP, Pollet BG. Performance analysis of cylindrical metal hydride beds with various heat exchange options. Journal of Alloys and Compounds. 2015;645:S89-S95.
[101] Wu Z, Yang F, Zhu L, Feng P, Zhang Z, Wang Y. Improvement in hydrogen desorption performances of magnesium based metal hydride reactor by incorporating helical coil heat exchanger. International Journal of Hydrogen Energy. 2016;41:16108-21.
[102] Feng P, Liu Y, Ayub I, Wu Z, Yang F, Zhang Z. Optimal design methodology of metal hydride reactors for thermochemical heat storage. Energy Conversion and Management. 2018;174:239-47.
[103] Shim J-H, Park M, Lee YH, Kim S, Im YH, Suh J-Y, et al. Effective thermal conductivity of MgH2 compacts containing expanded natural graphite under a hydrogen atmosphere. International Journal of Hydrogen Energy. 2014;39:349-55.

[104] Ben Mâad H, Miled A, Askri F, Ben Nasrallah S. Numerical simulation of absorption-desorption cyclic processes for metal-hydrogen reactor with heat recovery using phase-change material. Applied Thermal Engineering. 2016;96:267-76.
[105] Churchill SW, Chu HHS. Correlating equations for laminar and turbulent free convection from a vertical plate. International Journal of Heat and Mass Transfer. 1975;18:1323-9.
[106] Lemmon EW, McLinden MO, Friend DG, National Institute of S, Technology. Thermophysical properties of fluid systems. 1998.
[107] Tian Y, Zhao CY. A review of solar collectors and thermal energy storage in solar thermal applications. Applied Energy. 2013;104:538-53.
[108] Balakrishnan S, Sofianos MV, Humphries TD, Paskevicius M, Buckley CE. Thermochemical energy storage performance of zinc destabilized calcium hydride at high-temperatures. Physical Chemistry Chemical Physics. 2020;22:25780-8.
[109] Griffond ACM, Sofianos MV, Sheppard DA, Humphries TD, Sargent A-L, Dornheim M, et al. High-temperature thermochemical energy storage using metal hydrides: Destabilisation of calcium hydride with silicon. Journal of Alloys and Compounds. 2021;858:158229.
[110] Humphries TD, Møller KT, Rickard WDA, Sofianos MV, Liu S, Buckley CE, et al. Dolomite: a low cost thermochemical energy storage material. Journal of Materials Chemistry A. 2019;7:1206-15.
[111] Poupin L, Humphries TD, Paskevicius M, Buckley CE. An experimental high temperature thermal battery coupled to a low temperature metal hydride for solar thermal energy storage. Sustainable Energy & Fuels. 2020;4:285-92.
[112] Sakintuna B, Lamaridarkrim F, Hirscher M. Metal hydride materials for solid hydrogen storage: A review☆. International Journal of Hydrogen Energy. 2007;32:1121-40.
[113] Ward PA, Corgnale C, Teprovich JA, Motyka T, Hardy B, Sheppard D, et al. Technical challenges and future direction for high-efficiency metal hydride thermal energy storage systems. Applied Physics A. 2016;122:462.
[114] Bellosta von Colbe J, Ares J-R, Barale J, Baricco M, Buckley C, Capurso G, et al. Application of hydrides in hydrogen storage and compression: Achievements, outlook and perspectives. International Journal of Hydrogen Energy. 2019;44:7780-808.
[115] Humphries TD, Moller KT, Rickard WDA, Sofianos MV, Liu S, Buckley CE, et al. Dolomite: A Low Cost Thermochemical Energy Storage Material. Journal of Materials Chemistry A. 2018:Submitted.
[116] Milanese C, Jensen TR, Hauback BC, Pistidda C, Dornheim M, Yang H, et al. Complex hydrides for energy storage. International Journal of Hydrogen Energy. 2019;44:7860-74.
[117] Humphries TD, Sheppard DA, Li G, Rowles MR, Paskevicius M, Matsuo M, et al. Complex hydrides as thermal energy storage materials: characterisation and thermal decomposition of Na2Mg2NiH6. Journal of Materials Chemistry A. 2018;6:9099-108.
[118] Møller KT, Sheppard D, Ravnsbæk DB, Buckley CE, Akiba E, Li H-W, et al. Complex Metal Hydrides for Hydrogen, Thermal and Electrochemical Energy Storage. Energies. 2017;10.
[119] Sheppard DA, Humphries TD, Buckley CE. Sodium-based hydrides for thermal energy applications. Applied Physics A. 2016;122:406.
[120] Cot-Gores J, Castell A, Cabeza LF. Thermochemical energy storage and conversion: A-state-of-the-art review of the experimental research under practical conditions. Renewable and Sustainable Energy Reviews. 2012;16:5207-24.
[121] Mao Q. Recent developments in geometrical configurations of thermal energy storage for concentrating solar power plant. Renewable and Sustainable Energy Reviews. 2016;59:320-7.
[122] Askri F, Bensalah M, Jemni A, Bennasrallah S. Optimization of hydrogen storage in metal-hydride tanks. International Journal of Hydrogen Energy. 2009;34:897-905.
[123] Kaplan Y. Effect of design parameters on enhancement of hydrogen charging in metal hydride reactors. International Journal of Hydrogen Energy. 2009;34:2288-94.
[124] Garrier S, Chaise A, de Rango P, Marty P, Delhomme B, Fruchart D, et al. MgH2 intermediate scale tank tests under various experimental conditions. International Journal of Hydrogen Energy. 2011;36:9719-26.

[125] Bhouri M, Goyette J, Hardy BJ, Anton DL. Numerical modeling and performance evaluation of multi-tubular sodium alanate hydride finned reactor. International Journal of Hydrogen Energy. 2012;37:1551-67.
[126] Mathew A, Nadim N, Chandratilleke TT, Humphries TD, Paskevicius M, Buckley CE. Performance analysis of a high-temperature magnesium hydride reactor tank with a helical coil heat exchanger for thermal storage. International Journal of Hydrogen Energy. 2021;46:1038-55.
[127] Garrier S, Delhomme B, de Rango P, Marty P, Fruchart D, Miraglia S. A new MgH2 tank concept using a phase-change material to store the heat of reaction. International Journal of Hydrogen Energy. 2013;38:9766-71.
[128] Madaria Y, Anil Kumar E, Srinivasa Murthy S. Effective thermal conductivity of reactive packed beds of hydriding materials. Applied Thermal Engineering. 2016;98:976-90.
[129] Wang Z-M, Tao S, Li J-J, Deng J-Q, Zhou H, Yao Q. The Improvement of Dehydriding the Kinetics of NaMgH3 Hydride via Doping with Carbon Nanomaterials. Metals. 2017;7:9.
[130] Forster HK, Zuber N. Dynamics of vapor bubbles and boiling heat transfer. AIChE Journal. 1955;1:531-5.
[131] Chandratilleke TT, Nadim N. Enhanced Thermo-Fluid Dynamic Modelling Methodologies for Convective Boiling. In: Khan MMK, Chowdhury AA, Hassan NMS, editors. Application of Thermo-fluid Processes in Energy Systems: Key Issues and Recent Developments for a Sustainable Future. Singapore: Springer Singapore; 2018. p. 173-202.
[132] Abishek S, King AJC, Narayanaswamy R. Computational analysis of two-phase flow and heat transfer in parallel and counter flow double-pipe evaporators. International Journal of Heat and Mass Transfer. 2017;104:615-26.
[133] Jemni A, Nasrallah SB. Study of two-dimensional heat and mass transfer during absorption in a metal-hydrogen reactor. International Journal of Hydrogen Energy. 1995;20:43-52.
[134] M. Lemmert LMC. Influence of Flow Velocity on Surface Boiling Heat Transfer Coefficient in Heat Transfer in Boiling. E Hahne, U Grigull (Eds), Academic Press and Hemisphere, New York, NY, USA. 1977.
[135] Kurul N, Podowski MZ. Multidimensional effects in forced convection subcooled boiling. Proceedings of the 9th International Heat Transfer Conference, Jerusalem, Israel. 1990;1:21-6.
[136] Taguchi T, Saito A, Yanai H. Development of efficient Lewis acid catalysts for intramolecular cycloaddition reactions of ester-tethered substrates. Chem Rec. 2007;7:167-79.
[137] Ranz WE, Marshall WR. Evaporation from drops, Part 1 and Part 2. Chem Eng Prog. 1952;48 (4):173-80.
[138] Ishii M, Zuber N. Drag coefficient and relative velocity in bubbly, droplet or particulate flows. AIChE Journal. 1979;25:843-55.
[139] Moraga FJ, Bonetto FJ, Lahey RT. Lateral forces on spheres in turbulent uniform shear flow. International Journal of Multiphase Flow. 1999;25:1321-72.
[140] Troshko AA, Hassan YA. A two-equation turbulence model of turbulent bubbly flows. International Journal of Multiphase Flow. 2001;27:1965-2000.
[141] Cole R. A photographic study of pool boiling in the region of the critical heat flux. AIChE Journal. 1960;6:533-8.
[142] Bartolemei GG, Chanturiya VM. Experimental study of true void fraction when boiling subcooled water in vertical tubes. Teploenergeika. 1967;14 (2):123 - 8.
[143] Zhang R, Cong T, Tian W, Qiu S, Su G. Effects of turbulence models on forced convection subcooled boiling in vertical pipe. Annals of Nuclear Energy. 2015;80:293-302.
[144] EW L, MO M, DG F. National Institute of Standards and Technology. Thermophysical properties of fluid systems. 1998.
[145] Gil A, Medrano M, Martorell I, Lázaro A, Dolado P, Zalba B, et al. State of the art on high temperature thermal energy storage for power generation. Part 1—Concepts, materials and modellization. Renewable and Sustainable Energy Reviews. 2010;14:31-55.

[146] Wagner SJ, Rubin ES. Economic implications of thermal energy storage for concentrated solar thermal power. Renewable Energy. 2014;61:81-95.
[147] N'Tsoukpoe KE, Liu H, Le Pierrès N, Luo L. A review on long-term sorption solar energy storage. Renewable and Sustainable Energy Reviews. 2009;13:2385-96.
[148] Urbanczyk R, Peinecke K, Peil S, Felderhoff M. Development of a heat storage demonstration unit on the basis of Mg2FeH6 as heat storage material and molten salt as heat transfer media. International Journal of Hydrogen Energy. 2017;42:13818-26.
[149] Carrillo AJ, González-Aguilar J, Romero M, Coronado JM. Solar Energy on Demand: A Review on High Temperature Thermochemical Heat Storage Systems and Materials. Chemical Reviews. 2019;119:4777-816.
[150] Benitez-Guerrero M, Sarrion B, Perejon A, Sanchez-Jimenez PE, Perez-Maqueda LA, Manuel Valverde J. Large-scale high-temperature solar energy storage using natural minerals. Solar Energy Materials and Solar Cells. 2017;168:14-21.
[151] Butler JW, Grace JR. 16 - High-pressure systems and processes for calcium looping. In: Fennell P, Anthony B, editors. Calcium and Chemical Looping Technology for Power Generation and Carbon Dioxide (CO2) Capture: Woodhead Publishing; 2015. p. 377-408.
[152] Outukumpu, HSC Chemistry, Houston, version 6.
[153] Stanmore BR, Gilot P. Review—calcination and carbonation of limestone during thermal cycling for CO2 sequestration. Fuel Processing Technology. 2005;86:1707-43.
[154] Sun P, Grace JR, Lim CJ, Anthony EJ. The effect of CaO sintering on cyclic CO2 capture in energy systems. AIChE Journal. 2007;53:2432-42.
[155] Grasa GS, Abanades JC, Alonso M, González B. Reactivity of highly cycled particles of CaO in a carbonation/calcination loop. Chemical Engineering Journal. 2008;137:561-7.
[156] Grasa G, Murillo R, Alonso M, Abanades JC. Application of the random pore model to the carbonation cyclic reaction. AIChE Journal. 2009;55:1246-55.
[157] Valverde JM, Sanchez-Jimenez PE, Perez-Maqueda LA. Limestone Calcination Nearby Equilibrium: Kinetics, CaO Crystal Structure, Sintering and Reactivity. The Journal of Physical Chemistry C. 2015;119:1623-41.
[158] Benitez-Guerrero M, Valverde JM, Sanchez-Jimenez PE, Perejon A, Perez-Maqueda LA. Multicycle activity of natural CaCO3 minerals for thermochemical energy storage in Concentrated Solar Power plants. Solar Energy. 2017;153:188-99.
[159] Zhu Q, Zeng S, Yu Y. A Model to Stabilize CO2 Uptake Capacity during Carbonation–Calcination Cycles and its Case of CaO–MgO. Environmental Science & Technology. 2017;51:552-9.
[160] Filitz R, Kierzkowska AM, Broda M, Müller CR. Highly Efficient CO2 Sorbents: Development of Synthetic, Calcium-Rich Dolomites. Environmental Science & Technology. 2012;46:559-65.
[161] Li L, King DL, Nie Z, Howard C. Magnesia-Stabilized Calcium Oxide Absorbents with Improved Durability for High Temperature CO2 Capture. Industrial & Engineering Chemistry Research. 2009;48:10604-13.
[162] Park J, Yi KB. Effects of preparation method on cyclic stability and CO2 absorption capacity of synthetic CaO–MgO absorbent for sorption-enhanced hydrogen production. International Journal of Hydrogen Energy. 2012;37:95-102.
[163] Da Y, Xuan Y, Teng L, Zhang K, Liu X, Ding Y. Calcium-based composites for direct solar-thermal conversion and thermochemical energy storage. Chemical Engineering Journal. 2020;382:122815.
[164] Yang L, Huang Z, Huang G. Fe- and Mn-Doped Ca-Based Materials for Thermochemical Energy Storage Systems. Energy & Fuels. 2020;34:11479-88.
[165] Valverde JM, Perejon A, Perez-Maqueda LA. Enhancement of Fast CO2 Capture by a Nano-SiO2/CaO Composite at Ca-Looping Conditions. Environmental Science & Technology. 2012;46:6401-8.
[166] Manovic V, Anthony EJ. Integration of Calcium and Chemical Looping Combustion using Composite CaO/CuO-Based Materials. Environmental Science & Technology. 2011;45:10750-6.

[167] Wang Y, Zhu Y, Wu S. A new nano CaO-based CO2 adsorbent prepared using an adsorption phase technique. Chemical Engineering Journal. 2013;218:39-45.
[168] Zhang L, Lu Y, Rostam-Abadi M. Sintering of calcium oxide (CaO) during CO2 chemisorption: a reactive molecular dynamics study. Physical Chemistry Chemical Physics. 2012;14:16633-43.
[169] Koirala R, Gunugunuri KR, Pratsinis SE, Smirniotis PG. Effect of Zirconia Doping on the Structure and Stability of CaO-Based Sorbents for CO2 Capture during Extended Operating Cycles. The Journal of Physical Chemistry C. 2011;115:24804-12.
[170] Tregambi C, Salatino P, Solimene R, Montagnaro F. An experimental characterization of Calcium Looping integrated with concentrated solar power. Chemical Engineering Journal. 2018;331:794-802.
[171] Wu SF, Li QH, Kim JN, Yi KB. Properties of a Nano CaO/Al2O3 CO2 Sorbent. Industrial & Engineering Chemistry Research. 2008;47:180-4.
[172] Tesio U, Guelpa E, Verda V. Integration of thermochemical energy storage in concentrated solar power. Part 1: Energy and economic analysis/optimization. Energy Conversion and Management: X. 2020;6:100039.
[173] Tregambi C, Montagnaro F, Salatino P, Solimene R. Directly irradiated fluidized bed reactors for thermochemical processing and energy storage: Application to calcium looping. AIP Conference Proceedings. 2017;1850:090007.
[174] Tescari S, Neises M, de Oliveira L, Roeb M, Sattler C, Neveu P. Thermal model for the optimization of a solar rotary kiln to be used as high temperature thermochemical reactor. Solar Energy. 2013;95:279-89.
[175] Shimizu T, Hirama T, Hosoda H, Kitano K, Inagaki M, Tejima K. A Twin Fluid-Bed Reactor for Removal of CO2 from Combustion Processes. Chemical Engineering Research and Design. 1999;77:62-8.
[176] Bhatia SK, Perlmutter DD. Effect of the product layer on the kinetics of the CO2-lime reaction. AIChE Journal. 1983;29:79-86.
[177] Mess D, Sarofim AF, Longwell JP. Product Layer Diffusion during the Reaction of Calcium Oxide with Carbon Dioxide. Energy & Fuels. 1999;13:999-1005.
[178] Silaban A, Harrison DP. HIGH TEMPERATURE CAPTURE OF CARBON DIOXIDE: CHARACTERISTICS OF THE REVERSIBLE REACTION BETWEEN CaO(s) and CO2(g). Chemical Engineering Communications. 1995;137:177-90.
[179] Sun P, Grace JR, Lim CJ, Anthony EJ. Determination of intrinsic rate constants of the CaO–CO2 reaction. Chemical Engineering Science. 2008;63:47-56.
[180] Scaltsoyiannes A, Lemonidou A. CaCO3 decomposition for calcium-looping applications: Kinetic modeling in a fixed-bed reactor. Chemical Engineering Science: X. 2020;8:100071.
[181] Wang H, Li Z, Li Y, Cai N. Reduced-order model for CaO carbonation kinetics measured using micro-fluidized bed thermogravimetric analysis. Chemical Engineering Science. 2021;229:116039.
[182] Ortiz C, Valverde JM, Chacartegui R, Perez-Maqueda LA. Carbonation of Limestone Derived CaO for Thermochemical Energy Storage: From Kinetics to Process Integration in Concentrating Solar Plants. ACS Sustainable Chemistry & Engineering. 2018;6:6404-17.
[183] Khawam A, Flanagan DR. Solid-State Kinetic Models: Basics and Mathematical Fundamentals. The Journal of Physical Chemistry B. 2006;110:17315-28.
[184] Vyazovkin S, Burnham AK, Criado JM, Pérez-Maqueda LA, Popescu C, Sbirrazzuoli N. ICTAC Kinetics Committee recommendations for performing kinetic computations on thermal analysis data. Thermochimica Acta. 2011;520:1-19.
[185] Fedunik-Hofman L, Bayon A, Donne SW. Kinetics of Solid-Gas Reactions and Their Application to Carbonate Looping Systems. Energies. 2019;12:2981.
[186] Fedunik-Hofman L, Bayon A, Donne SW. Comparative Kinetic Analysis of CaCO3/CaO Reaction System for Energy Storage and Carbon Capture. Applied Sciences. 2019;9.
[187] Mathew A, Nadim N, Chandratilleke TT, Humphries TD, Buckley CE. Investigation of boiling heat transfer for improved performance of metal hydride thermal energy storage. International Journal of Hydrogen Energy. 2021;46:28200-13.

[188] Touloukian YS. Thermal Expansion: Nonmetallic Solids, Thermophysical Properties of Matter. 1977.
[189] Catalog. https://www.toyotanso.com/Products/catalogenfullpdf20.